Title

Studies of stochastic effects in biological signaling pathways

Permalink

Author

Wang, Kai

Publication Date

2006

UNIVERSITY OF CALIFORNIA, SAN DIEGO

Studies of Stochastic Effects in Biological Signaling Pathways

A dissertation submitted in partial satisfaction of the
requirements for the degree Doctor of Philosophy
in
Physics (Biophysics)

by

Kai Wang

Committee in charge:

Professor Herbert Levine, Chair
Professor Wolfgang H. Dillmann
Professor Terrence Hwa
Professor Andrew McCulloch
Professor Jose Onuchic

2006

The dissertation of Kai Wang is approved, and it is acceptable in quality and form for publication on microfilm:

Chair

University of California, San Diego

2006

TABLE OF CONTENTS

LIST OF FIGURES

LIST OF TABLES

ACKNOWLEDGEMENTS

First of all I would like to gratefully thank my advisor, Professor Herbert Levine, for leading me to the interesting theoretical biology field and guiding me throughout the progress of my doctoral research work. His genuine interest in science has always been very inspiring, and his profound knowledge has made our discussions on research projects always very fruitful. The most important thing I have learned from him, is the optimistic and rational way to confront and solve difficulties appearing in work, which will benefit my whole life no matter what I will be working on.

I would like to thank Dr. Wouter-Jan Rappel. He has participated in all of my research work and contributed on every aspect of it, including the initial modeling, the simulation and the paper writing. He is always so generous to discuss with me whenever I need help, and I feel very lucky to collaborate with him.

I would also like to thank other collaborators. Dr. Yuhai Tu at IBM research center gave me very useful discussions on our initial modeling of RyR during his visit to CTBP in the summer of 2004. Dr. Rex Kerr and Dr. Tom Bartol at Salk Institute have provided great support on our MCell simulations in the chemoreception project. Rex worked very hard to modify the MCell source code and generate the boundary condition that satisfies our simulation needs, and it was done during his busiest time. I hereby appreciate his work very much.

I appreciate all the efforts done by the leaders and staff members of the center for theoretical biological physics. They have provided great facilities, especially the computation power, to support our research work. Much of my work involves heavily with simulations which cannot be done without it.

Finally I would like to give my deepest thanks to my parents. They were not born at a right time in China, but they have selflessly supported my education for so many years.

The text of chapter III, in part, is a reprint of the material as it appears in Kai Wang, Wouter-Jan Rappel, and Herbert Levine, *Cooperativity can reduce stochasticity in intracellular calcium dynamics*, Phys. Biol. **1**, 27, © Institute of Physics and IOP Publishing Limited, where the dissertation author was the first author. The co-authors in this publication directed, supervised, and co-worked on the research which forms the basis of this chapter.

The text of chapter IV, in part, is a reprint of the material as it appears in Kai Wang, Yuhai Tu, Wouter-Jan Rappel, and Herbert Levine, *Excitation-Contraction Coupling Gain and Cooperativity of the Cardiac Ryanodine Receptor: A Modeling Approach*, Biophys. J. **89**, 3017, © 2005 Biophysical Society, where the dissertation author was the first author. The co-authors in this publication directed, supervised, and co-worked on the research which forms the basis of this chapter.

The text of chapter V, in part, is a reprint of the material as it appears in Kai Wang, Wouter-Jan Rappel, Rex Kerr and Herbert Levine, *Measuring Intercellular Signals with Arbitrary Accuracy*, Submitted to Proc. Natl. Acad. Sci., where the dissertation author was the first author. The co-authors in this publication directed, supervised, and co-worked on the research which forms the basis of this chapter.

VITA

1979	Born, Wuhu, China
2001	Bachelor of Science in Physics Peking University, Beijing, China
2001–2002	Teaching Assistant, Department of Physics University of California, San Diego
2002–2006	Research Assistant, Department of Physics & Center for Theoretical Biological Physics University of California, San Diego
2006	Doctor of Philosophy University of California, San Diego

PUBLICATIONS

Kai Wang, Wouter-Jan Rappel, and Herbert Levine, *Cooperativity Can Reduce Stochasticity in Intracellular Calcium Dynamics*, Phys. Biol. **1**, 27 (2004).

Kai Wang, Yuhai Tu, Wouter-Jan Rappel, and Herbert Levine, *Excitation-Contraction Coupling Gain and Cooperativity of the Cardiac Ryanodine Receptor: A Modeling Approach*, Biophys. J. **89**,3017 (2005).

Kai Wang, Wouter-Jan Rappel, Rex Kerr, and Herbert Levine, *Measuring Intercellular Signals with Arbitrary Accuracy*, submitted to Proc. Natl. Acad. Sci.

FIELDS OF STUDY

Major Field: Physics
  Studies in Intracellular Calcium Dynamics.
  Professor Herbert Levine

  Studies in Cellular Signaling Pathways.
  Professor Herbert Levine

  Studies in Statistical Physics.
  Professor Terrence Hwa

ABSTRACT OF THE DISSERTATION

Studies of Stochastic Effects in Biological Signaling Pathways

by

Kai Wang
Doctor of Philosophy in Physics (Biophysics)
University of California, San Diego, 2006
Professor Herbert Levine, Chair

In this thesis three case studies of stochastic effects in biological signaling systems are presented. The opening of Ca release channels, clustered at discrete sites on the endoplasmic reticulum, can lead to large scale intracellular calcium waves. Experiments in *Xenopus* oocytes have shown the inter-wave intervals for these waves have a standard deviation much smaller than the mean and that the background $[\mathrm{Ca}^{2+}]$ exhibits a slow rise during the interwave interval. In Chapter III we modeled this process and confirmed slow rise of Ca increases the cooperativity between the openings of the clusters. Moreover, a slow kinetics of Ca pump proteins is important for the accumulation of background Ca.

Cardiac calcium release channels are reported to have sub-conducting states when FK-506 binding protein (FKBP) level is low. This has important implications for heart failure, where it has been hypothesized that hyperphosphorylation of calcium channel by β-adrenergic stimulation results in a loss of FKBP binding, which can lead to a persistent leak and a reduced SR calcium content. In Chapter IV we modeled the gating of the channel via an allosteric interaction between its subunits and coupled this dynamics with the excitation-contraction (E-C) cycle of cardiac myocytes. We find the level of cooperativity can have a dramatic effect on the cardiac E-C coupling gain and that this gain exhibits a clear maximum. These findings are compared to currently available data from different species and allows for an evaluation of the heart failure scenario.

Cells often measure their local environment via the interaction of diffusible chemical signals with membrane receptors. At the level of a single receptor, this process is inherently stochastic, but cells can contain many such receptors to reduce the variability in the detected signal by suitable averaging. In Chapter V, we use explicit Monte Carlo simulations and analytical calculations to characterize the noise level as a function of the number of receptors. We show that the residual noise approaches zero and that the correlation time diverges for large receptor numbers. This result has important implications for such processes as eukaryotic chemotaxis.

I

Introduction

Physicists have been fascinated by the versatility of biological world for a long time. Accompanying with the revolution of molecular biology marked by the discovery of DNA structure, theoretical biology has prospered for decades. Due to limited access to experimental data, early theoretical research focused on universal phenomena such as enzyme dynamics, or circadian rhythms, etc. Such research was directly related to some fields of physics like nonlinear dynamics, and was of great interest by physicists. But the models were usually phenomenological and can hardly be linked to the real biological components in a specific system. Moreover, a whole picture including different spatial and temporal properties of the system was lacking because experiments couldn't provide enough details.

Nowadays experimental biology has made tremendous progress and almost every biological process can be studied through experiments. Some systems, such as *Escherichia coli (E. coli)* chemotaxis, have been studied so thoroughly that almost every functional protein and gene is known. The enormous experimental data has provided theorists a great platform to do modeling work on all scales from atom level to ecological level with highly reliable system parameters. On the other hand, although a lot of facts have been accumulated, there is still a long way to truly understand how those components work together to form an organism. Theorists can help this understanding process by making models based on their theoretical training. A successful model can identify the critical players of the process and provoke new experiment designs. Moreover, today's biological modeling is heavily involved with computer simulation, mostly using differential equations or Monte Carlo methods. Thanks to the incredibly increasing computation speed, it is possible to run simulations of large spatial and temporal scales which take no more than a few days. Simulation costs much less than experiment, and one can freely change parameters, with some of those being impossible to be varied in experiments. This provides an advantage to explore a much wider range of dynamics of the system.

Among all levels of modeling, signaling transduction pathways involve with how enzymes and second messenger molecules are connected together to fulfill a specific cellular function such as cell division, cell motility, etc., and how the cell reacts to specific membrane stimuli such as hormone stimulation or membrane depolarization. At this cellular level, the enzyme-ligand interaction is usually modeled as chemical rate equations abstracted from more detailed protein dynamics research. Mathematically, even there are only a few participants in the signaling pathway, they can form complicated nonlinear reaction network and have rich dynamic behavior such as oscillations, switch-like behaviors, and even chaos, although the latter one is the region that cells try to avoid.

Since the spatial effects have no place in the rate equation models, the cell is modeled as a well-stirred reactor, and the modeling tool is a set of ordinary differential equations. In many cases this methodology works fine for an initial model, and it's easy to analyze and fast to simulate. But there are more situations where spatial difference of reaction components cannot be ignored. Molecules inside a cell is not uniformly distributed. A cell has its structure and different ligands and proteins are compartmentalized into different regions such as nucleus, endoplasmic reticulum, mitochondria, etc. In this case a common-pool model can be changed to a model with several pools and the communication between different pools can be modeled as well.

As another possibility, some cellular events initiate at a local region and can propagate through the whole cell. For example, intracellular calcium release channels usually form clusters and distribute discretely in space. They have a positive feedback circuit called calcium-induced-calcium-release (CICR). That means, they can be activated by calcium and release more calcium from internal Ca^{2+} stores. Once a local cluster is activated, the released calcium has the potential to open neighboring clusters and eventually form a propagating calcium wave. This wave sometimes work as an important intracellular signal. For example, the sperm initiated Ca^{2+} wave in oocyte fertilization process propagates through the whole cytoplasm and triggers a series of important biological events. [1, 2]. But in other systems like ventricular cells, a Ca^{2+} wave is considered as harmful and is blocked under physiological condition [3]. So the geometric distribution and diffusive property of biological components can be a decisive factor for the function, even the underlying rate equations show no difference.

Moreover, spatial properties are intrinsic for some cellular functions. One example is cell division. The cell decides the spatial location to divide itself into two equally half by forming a FtsZ ring [4, 5]. Then all the cellular organelles are equally partitioned into the two halves before the division begins. This whole event is highly organized in space, while it is still based on the chemical reactions between regulatory proteins, coupled with spatial diffusion process. Another example is eukaryotic chemotaxis. An eukaryotic cell can tell the gradient of chemical signal concentration and swim in that direction. The receptors which capture the signal molecules distribute uniformly on cell membrane. They accept signals indistinguishably and transmit the them into the cell. The whole signaling pathway must have the ability to compare membrane receptor activity in all directions and decide the way to go. Here again the large scale spatial effect is intrinsically required, and it is implemented by the coupling between reaction and diffusion.

The importance of spatiotemporal dynamics of cellular signaling presents us a puzzle. On one hand, the cell is usually small (1-10μm in length) and typical molecule concentration ranges from nM to mM. With a simple calculation we know that 1μM is equivalent to roughly 0.6 molecule per μm^3. That means for many reactions with μM or lower molecule concentration, there are usually no more than 1000 molecules in the whole cell. For example, in cardiac excitation-contraction coupling, in the local chamber where Ca^{2+} is released, there is only about one free Ca^{2+} ion during peak activity, and zero for most of the time. Such a small number of molecules causes large intrinsic fluctuations in the system that is comparable to the mean concentration, and thus can damage the efficiency of cellular signaling. On the other hand, cellular signaling pathway turns out to have many excellent features, such as high accuracy, adaptability, specificity, and stability. For cell division, the determined location for the formation of FtsZ ring is highly accurate, with the error less than 3% of cell length [6]. Eukaryotic cells can detect a gradient as small as 1% of background concentration across the cell, and such a high accuracy is maintained across four orders of background concentration, showing great adaptability. The T-cell recognition of antigen-presenting-cells (APCs) is an extremely specific process. T-cell receptors can identify a single antigen peptide among thousands of domestic peptides and amplify the signal to trigger a whole-cell event [7]. All of these facts imply cells must have found their unique ways to deal with stochastic effects during the long time of evolution.

Some of these mechanisms have been well known. The most simple way is probably to increase the number of participating molecules directly, and trading the reaction time with high accuracy. But it has a cost and is not feasible for some small cells. Specific reaction networks can also control the noise. For example, for a simplest two-component model, a negative feedback can effectively suppress noise level, while a positive feedback circuit strengthens the signal and forms a switch-like all-or-none behavior [8]. Proteins can also form dimers or other composites to limit their accessibility with ligands and make the reaction more controllable. These are bricks to form more complicated nonlinear reaction networks. The spatial organization also plays a role in controlling the noise. In calcium dynamics, calcium sparks caused by single cluster of Ca^{2+} release channels are stochastic events. Other factors such as Ca^{2+} binding proteins (Ca^{2+} buffers) and spacing between clusters determine whether the individual events should communicate with each other or not. For example, in Xenopus oocytes, opening of >7 neighboring clusters seems to be a threshold for initiating a global Ca^{2+} wave [9]. In ventricular cells, Ca^{2+} release is strictly controlled by membrane depolarization. The rate of individual spontaneous sparks is controlled under a low level and regenerative calcium wave is unwanted. So the system parameters ensure the released Ca^{2+} from one unit cannot trigger another, unless under pathological conditions where Ca^{2+} release is prolonged and amplified [3]. These mechanisms show that the way to control the noise is very versatile and depends on the specific system that is of interest. Such research involves heavily with modeling stochastic reaction-diffusion systems, Monte-Carlo simulations and detailed experimental observations. It brings interesting and challenging topics to contemporary physicists, while is closely related to the real biology.

I.A Dissertation Outline

In this thesis the stochastic effects of calcium dynamics in two different systems: *Xenopus* oocytes and cardiac myocytes are discussed. Then we switch to chemotaxis process and a general theory for the noise level during biochemical signal detection is presented.

Calcium is a universal intracellular second messenger. Although its function is very versatile in different cell types, the mechanisms of its dynamics are all based on the calcium-induced-calcium-release of intracellular calcium channels. In Chapter II I will first introduce the common components of calcium signaling pathway. Then two examples of calcium dynamics in oocytes and myocytes respectively are discussed.

In Chapter III we studied the spatiotemporal calcium dynamics in *Xeno-*

pus oocytes. Our research shows spontaneous global Ca^{2+} waves can be initiated through the gradual elevation of background Ca^{2+} contributed by individual opening of Ca^{2+} release sites, and the variation of inter-wave interval is much smaller than that of a Poisson process with the same mean. Such an integrate-and-fire mechanism requires the slow kinetics of calcium pump proteins.

In Chapter IV we modeled the stochastic gating of RyR, a calcium release channel in myocytes, by assuming cooperativity between subunits of RyR can be controlled by bound FKBP, a small RyR regulatory protein. The RyR model is integrated into the whole excitation-contraction process of myocyte and is shown that the loss of cooperativity can lead to heart failure disease. The modeling results also explained the apparant discrepancy of the function of FKBP observed in experiments across different species.

In Chapter V we reviewed the classic chemoreception theory by Burg and Purcell in 1977 [10]. The theory deals with the initial step of a general extracellular signal detection process and claims there is a universal limit of accuracy for the detection process that cannot be improved by increasing membrane receptor number. We showed through both theory and Monte Carlo simulation that the limit only exists when the measuring time of down signaling pathway is much larger than the correlation time scale of this detection process, and the correlation time increases linearly when increasing the number of receptors. Thus increasing receptor number converts a time-averaged measurement into an instantaneous measurement by reducing the correlation time, and the error of measurements approaches zero. This work clarifies the noise structure of the detection process and helps to build more accurate chemotaxis models.

Bibliography

[1] Dumollard, R., Carroll, J., Dupont, G. & Sardet, C. (2002) Calcium wave pacemakers in eggs. *J. Cell Sci.* **115,** 3557-3564.

[2] Webb, S. E. & Miller, A. L. (2003) Calcium signalling during embryonic development. *Nat. Rev. Mol. Cell Biol.* **4,** 539-551.

[3] Lakatta, E. G. & Guarnieri, T. (1993) Spontaneous myocardial calcium oscillations: are they linked to ventricular fibrillation? *J. Cardiovasc. Electrophysiol.* **4,** 473-489.

[4] Bi, E. & Lutkenhaus, J. (1993) Cell division inhibitors SulA and MinCD prevent formation of the FtsZ ring. *J. Bacteriol.* **175,** 1118-1125.

[5] Bi, E. & Lutkenhaus, J. (1991) FtsZ ring structure associated with division in Escherichia coli. *Nature* **354,** 161-164.

[6] Yu, X.-C. & Margolin, W. (1999) FtsZ ring clusters in min and partition mutants: role of both the Min system and the nucleoid in regulating FtsZ ring localization. *Mol. Microbiol.* **32,** 315-326.

[7] Irvine, D. J., Purbhoo, M. A., Krogsgaard, M. & Davis, M. M. (2002) Direct observation of ligand recognition by T cells. *Nature* **419,** 845-849.

[8] Stelling, J., Sauer, U., Szallasi, Z., Doyle, F. J. & Doyle, J. (2004) Robustness of cellular functions. *Cell* **118,** 675-685.

[9] Marchant, J., Callamaras N. & Parker, I. (1999) Initiation of IP_3 -mediated Ca^{2+} waves in *Xenopus* oocytes *EMBO* **18,** 5285-5299.

[10] Berg, H. C. & Purcell, E. M. (1977) Physics of chemoreception. *Biophys. J.* **20,** 193-219.

II

A Brief Review of Intracellular Calcium Dynamics

Ca^{2+} is an omnipresent intracellular second messenger that regulates many different cellular functions. Its cytosolic concentration is determined by a balance of processes that bring Ca^{2+} into cytoplasm and processes that remove Ca^{2+} from the cytoplasm [10]. The basal level of cytosolic Ca^{2+} is kept low since a persistent high calcium transient leads to unsoluble Ca^{2+} salts, which is very harmful. But upon external stimuli, membrane receptors can be triggered to activate oscillatory calcium concentration in cytoplasm.

For example, in non-muscle cells such as oocytes and hepatocytes, inositol 1,4,5-trisphosphate (IP_3) is produced through the activation of phospholipase C (PLC) by signals such as fertilization or hormone stimulation. As a response, calcium is released from endoplasmic reticulum (ER) through IP_3 receptors (IP_3Rs). In cardiac myocytes, calcium entry during depolarization of plasma membrane triggers large calcium release from sarcoplasmic reticulum (SR) through ryanodine receptors (RyRs), which activates muscle contraction.

In this chapter we will first review the most common components of intracellular calcium signaling cycle. Then calcium dynamics in two specific systems: *Xenopus* oocytes and cardiac myocytes is discussed.

II.A Major Components of Calcium Signaling

Although each cell type utilize calcium in a unique way, the core part of calcium signaling pathways share a lot in common. As we have mentioned in last section, It always involves calcium transport between cytoplasm and internal stores such as SR/ER. The resting cytosolic Ca^{2+} is about 0.1μM, and Ca^{2+} inside SR/ER is roughly 1mM. Such a steep concentration gradient is maintained by SR/ER calcium ATPase (SERCA), which actively pump cytosolic Ca^{2+} into SR/ER. During a large releasing event, a group of IP_3R /RyR opens for less than 100ms and the cytosolic Ca^{2+} increases to 0.5-1μM, followed by a slow but persistent reuptake by SERCA. For excitable cells such as muscle cells or neurons, there are important calcium channels on the plasma membrane, such as Na^{+}-Ca^{2+} exchanger (NCX). There are also huge amount of calcium buffer proteins, either diffusible or non-diffusible. They modify the amplitude and diffusivity of Ca^{2+} in both cytoplasm and SR/ER.

II.A.1 IP_3R

IP_3R is one of the two major calcium release channels mediated with many calcium signaling events from the fertilization of oocytes [8, 9] to the control of gene expression, cell proliferation and cell death [10], to long-term depression of neural system [11, 12]. IP_3R is a tetrameric protein with 300kDa subunits. It has a central pore, and 4 large wings which provide functional sites for many regulators [13, 14]. The gating of IP_3R is controlled by IP_3 , which is a second messenger produced primarily by phospholipase C (PLC) metabolism of phosphoinositol-4,5-bisphosphate (PIP_2) activated by hormone-receptor coupled G-proteins [15, 16]. The channel is also regulated by Ca^{2+} through both an activation site and an inhibition site. The Ca^{2+} -dependent activation is fast (1 sec) and has high affinity (0.2 μM), but the inhibition process is more than ten times slower and has low affinity for Ca^{2+} (10-100 μM). So the steady state Ca^{2+} response curve is of bell shape, with highest open probability at 1-10μM Ca^{2+} . Furthermore, in response to a sudden Ca^{2+} elevation, IP_3R gating is of an adaptive manner, first activated, and subsequently inactivated. When this CICR is coupled with the calcium diffusion, buffering and reuptaking in cytoplasm, temporal oscillations and spatial waves of Ca^{2+} can appear under appropriate controlled IP_3 concentration. This interesting gating behavior of IP_3R has attracted modeling work since decades ago. Despite early phenomenological models based on generic excitable systems, such as Fitzhugh-Nagumo model [17], the first influential model is DeYoung-Keizer model [11]. It assumes there are 3 identical subunits for each IP_3R . Each unit can be regulated by IP_3 activation, Ca^{2+} activation or Ca^{2+} inhibition independently. The channel is only opened when each subunit has one IP_3 and one activating Ca^{2+} bound, and no inactivating Ca^{2+} bound. Although the 3-subunits assumption is wrong and the regulation by IP_3 and Ca^{2+} is proved to be not independent, this model captures the essentials of IP_3R dynamics and forms the basis of other models. Li and Rinzel [12] simplified De Young-Keizer model and get a 2 component model, which is much easier to be analyzed.

II.A.2 RyR

RyR is the other major type of calcium release channels. It exists in many tissues, but it is mostly known as playing the central role in the excitation-contraction coupling in striated muscle. RyR is also a huge tetramer protein with a central pore which shares significant homology with IP_3R . The conductance of the pore is about 100pS for divalent cation but is not very selective. Under physiological condition, the current through a single RyR is suggested to be 0.5-1pA. Like IP_3R , RyR can be activated by low Ca^{2+} concentrations (1-10μM) and inhibited by high Ca^{2+} concentrations (1-10mM), but it is doubted that physiological Ca^{2+} can ever reach that high level for inhibition.

There are three isoforms of RyR. The expression of different isoforms is tissue specific. The predominant RyR isoform in skeletal muscle is RyR1 [1, 2].

Each RyR1 is physically associated with a cluster of 4 plasma membrane dihydropyridine receptors (DHPRs or L-type calcium channels) through a 10-nm gap between plasma membrane and SR membrane [3, 4]. It is thought that membrane depolarization can induce internal calcium release through the direct protein-protein interaction and it ensures the fast twitch of skeletal muscles [5, 6].

RyR2 is the most redundant isoform in cardiac muscle [1]. There are about 10 DHPRs and 50-100 RyRs in one calcium release unit [7]. Contrary to the skeletal muscle case, there is no physical contact between DHPR and RyR2, and they are loosely coupled through Ca^{2+} entry from DHPR and calcium-induced-calcium-release from RyR2. The coupling is considerably slower than DHPR-RyR1 signaling, but it may provide more opportunities for pharmacological regulation [7].

RyR3 is relatively rare in mammalian muscles, and its specific physiological role is still unclear [1]. In tissues other than striated muscles (e. g. neurons [12]), all isoforms of RyR can be expressed, as well as IP_3R s. The coexistence of these calcium release channels may work together and satisfy the complicated signaling function required by the cell.

RyR can be regulated by many molecules and proteins including Mg^{2+}, FK506 binding proteins (FKBP), protein kinase A (PKA), calmodulin, sorcin, and many others.

Mg^{2+} inhibits RyR in several ways. First, free cytosolic ATP is an RyR activator [1], but Mg^{2+} binds to ATP and reduces the amount of free ATP available to RyR. Second, Mg^{2+} is a competitive antagonist of RyR [1, 20, 21]. It can bind to Ca^{2+} activation sites on RyR, and thus prevents Ca^{2+} from opening the channel. Third, the high RyR inhibition site does not discriminate between different divalent cations, so even physiological Ca^{2+} can never reach the inhibition threshold, RyR can be inhibited by binding of Mg^{2+}, which is typically 1mM [1, 20, 21]. In addition, Mg^{2+} is reported to slow down the rate of activation of RyRs in response to sustained elevations of Ca^{2+} [22]. This could be critical to the control of excitation-contraction coupling since the trigger Ca^{2+} lasts only less than 1ms.

FKBP is a small protein that can bind to each of the RyR monomer. It has been observed that FKBP binding lowers open probability and prevents unwanted Ca^{2+} leak from SR without DHPR signal. Moreover, several groups have shown that lack of FKBP binding results in subconductance states of RyR [23, 24]. Subconductance states are open events with less than normal unit current amplitude. Some of the experiments show clearly 3 discrete subconductance, which indicates there are 4 stages of RyR opening, and FKBP stabilizes the channel by make the opening in a more cooperative way, i.e., with higher Ca^{2+} activation threshold and Hill coefficient. The level of bound FKBP is suggested to be critical in heart muscle excitation-contraction coupling [25, 26].

PKA is activated through β-adrenergic signaling pathway, and it can phosphorylate RyR. Some groups have reported that PKA phosphorylation results in the dissociation of FKBP from RyR, and thus destabilizes RyR [27]. However, other groups report FKBP is not dissociated by phosphorylation, or RyR kinetics is not altered [28, 29]. It is possible that different experimental conditions are responsible.

Sorcin is also a small RyR-binding protein. It inhibits RyR gating independent of Ca^{2+} regulation, and this inhibition is turned off by PKA phosphorylation of sorcin [30]. Overexpression of sorcin has been found to dramatically rescue the abnormal excitation-contraction coupling in diabetic heart [31], which may indicate sorcin helps to stabilize the RyR gating and prevents unwanted leaking of Ca^{2+} .

II.A.3 DHPR

As mentioned in last section, DHPR is a plasma membrane Ca^{2+} channel widely spreading in striated muscles and is responsible for triggering intracellular Ca^{2+} release when cell membrane is depolarized. It has a fast voltage-dependent activation and a slow voltage-dependent inactivation circuit, and a Ca^{2+} -dependent inactivation circuit [32, 33]. Upon depolarization, DHPR is opened immediately and allows extracellular Ca^{2+} to enter the cell. Since DHPRs are usually located very close to RyRs, the small Ca^{2+} entry can trigger large amount of Ca^{2+} release from SR. DHPR is then closed by the elevated intracellular Ca^{2+} and membrane potential. The opening of a DHPR is usually less than 1ms.

The details of the activation and inactivation sites on DHPR are still not clear, and several models have been proposed to describe its gating [34, 35, 36]. They are not necessarily optimal, but they all recover the kinetics observed in experiments very well.

II.A.4 SERCA

SERCA is a Ca-ATPase on ER/SR membrane. It actively pumps cytosolic Ca^{2+} released by $\mathrm{IP_3R}$/RyR back into ER/SR and keeps cytosolic Ca^{2+} at low level [37]. At the beginning of a transport cycle, one Ca^{2+} ion is binded to a Ca^{2+} binding site very rapidly. Then the second Ca^{2+} binding site is exposed, which explains the observed cooperative transport with Hill coefficient about 1-2. SERCA is only phosphorylated after two Ca^{2+} binding sites are occupied. Note that under appropriate conditions the phosphorylated SERCA can also bind ADP and synthesize ATP, so the reaction is reversible. At this stage SERCA still has high affinity for Ca^{2+} . Then it isomerizes rapidly and sequentially into several other intermediate forms which translocates the Ca^{2+} binding sites to the luminal side and lowers Ca^{2+} affinity by 3 orders. After Ca^{2+} ions are occluded SERCA is hydrolyzed in a reaction stimulated by Mg^{2+}. In total each cycle transports 2 Ca^{2+} ions into luminal side by the hydrolysis of 1 ATP. The steep gradient of Ca^{2+} across ER/SR membrane is maintained by this energy-costing process.

In theory the reuptake rate is usually modeled as:

$$J_{uptake} = \frac{V_{max}[Ca^{2+}]^n}{[Ca^{2+}]^n + K_{1/2}^n} \tag{II.1}$$

with Hill coefficient n=2 in most cases. The max uptake rate V_{max} is 0.5-1μM/s. Another model of SERCA is proposed recently by Bers group [38]:

$$J_{uptake} = \frac{V_{mf}([Ca^{2+}]_i/K_{mf})^n - V_{mr}([Ca^{2+}]_{SR}/K_{mr})^n}{1 + ([Ca^{2+}]_i/K_{mf})^n + ([Ca^{2+}]_{SR}/K_{mb})^n} \tag{II.2}$$

This model considers the fact that reuptake process is reversible and the rate is the difference of Ca^{2+} transport from cytoplasm to ER/SR and the vice versa. It has the potential to cover wider range of physiological parameters, such as partially depletion of ER/SR, or persistent high level of cytosolic Ca^{2+} .

There are three major isoforms of SERCA [39]. SERCA1 is expressed exclusively in fast-twitch skeletal muscle. SERCA2 has 2 sub-isoforms: SERCA2a and SERCA2b. SERCA2a expresses in cardiac and slow-switch skeletal muscle. Its quantitative properties are identical as SERCA1. SERCA2b exists in smooth muscle and non-muscle cells such as oocytes. It has lower rates for both calcium transport and ATP hydrolysis, which suggests a slower catalytic cycle. SERCA3 expresses in non-muscle cells. It has a lower Ca^{2+} affinity comparing to the other two.

II.A.5 Sodium Calcium Exchanger

To keep the Ca^{2+} balance inside a cell, there are other plasma membrane Ca^{2+} channels which extrude those Ca^{2+} entered through DHPR. The most important one is Na-Ca exchanger (NCX). This membrane protein imports Na^{+} ions by exporting Ca^{2+} ions, with the exchange stoichiometry as 3:1 (Na:Ca) [40]. Note that the exchange is also reversible and it depends on the membrane voltage and ion concentrations. The NCX current is likely to be responsible for the transient inward current during diastolic phase[7]. This current increases membrane potential and may trigger the opening of inward Na^{+} current and intracellular calcium releasing, producing the so-called delayed after-depolarization, which is usually a precaution of cardiac arrhythmia.

II.A.6 Buffer Proteins

Buffers are intracellular Ca^{2+} -binding proteins. They exist in large abundance in both cytoplasm and ER/SR. For example, calsequestrin is the major Ca^{2+} buffer in SR [41], and calmodulin and troponin C are Ca^{2+} buffers in cytoplasm [7]. These buffers bind most of the Ca^{2+} in a cell (up to 99%)[42]. Buffers have much lower diffusivity than free Ca^{2+} , and some of them are even immobile, so they greatly affect the intracellular Ca^{2+} dynamics by limiting the Ca^{2+} diffusion. For simulation, buffers with fast binding and unbinding rates like calsequestrin and calmodulin are modeled as in equilibrium with free Ca, while slow buffers are simulated according to their kinetics [41, 43].

II.B Case Studies of Calcium Dynamics

II.B.1 Spatial Organization and Spontaneous Calcium Waves

The opening of a single calcium release channel is the smallest calcium signaling event, called a ”blip”. However, calcium release channels are not uniformly distributed on ER/SR membrane. Instead 10-100 channels tend to form a cluster. Channels within one cluster are strongly coupled through CICR. That means, calcium ions released from a ”blip” can diffuse and increase the open probability of nearby channels. Such an elemental releasing event is the building block for local and global Ca^{2+} signaling. They are called ”puffs” for IP_3R mediated signaling, or ”sparks” for RyR mediated signaling. Puffs were first observed in immature *Xenopus* oocytes by I. Parker's group [44]. The calcium release is regulated by IP_3 level, which is controlled by flash photolysis of caged IP_3 . Ca^{2+} fluorescent indicator protein is added to the cell and the fluorescence is measured through confocal linescan microscopy technique. By this method they were able to measure the spatiotemporal spread of a highly localized Ca^{2+} release event. (See Figure II.1.)

Although the cluster size and the number of opening channels in a puff is very difficult to be directly measured, they are estimated by several models based on the confocal image results. Swillens *et al* [13] concluded a puff is generated by at least openings of 5 IP_3Rs, and a cluster has about 20-30 IP_3Rs, packed closely together in order to allow inter-channel cooperativity. More recently, Shuai *et al* [46] build a model directly simulating the fluorescence signal mass measured in experiments. They estimated there are 25 channel openings during a puff, the size of a cluster ranges from 300 to 800nm, and physiological current through a single IP_3R is about 0.4pA.

Ca^{2+} released from a puff can diffuse to neighboring sites and increase the rate of puffs at those sites. This weaker version of CICR has the potential to form organized calcium events, such as calcium waves, at a larger spatial scale. I. Parker's group have studied the initiation of spontaneous Ca^{2+} waves in unfertilized *Xenopus* oocytes with controlled IP_3 level [47] (see Figure II.1). They found the amount of Ca^{2+} required to trigger a wave was about 10-fold greater than the average size of a puff. However, frequent puffs contribute to a slow increase in basal free Ca, which increases puff rates slowly, and initiates a wave eventually.

The ability for a puff to trigger neighboring puffs is determined by the $[IP_3]$, the Ca^{2+} diffusivity, and the space between puff sites. The diffusion constant of free calcium is about $200\mu m^2/s$, but it's greatly reduced to about 25 $\mu m^2/s$ by Ca^{2+} buffers. The density of puff sites is about 1 per 20-30μm [48]. Jung and Shuai [18, 7] studied the global stochastic Ca^{2+} dynamics based on Li-Rinzel [12] model and revealed that global propagating wave can only happen in a selective range of $[IP_3]$, calcium diffusion constant (D), and spacing between puff sites (d). There are only independent puffs when $[IP_3]$ or D is too low, or d is too large. On the opposite side, there are too many competitive local calcium waves, and global Ca^{2+} average turns out to be constant. Global Ca^{2+} waves only appear for intermediate parameters.

The wave speed is studied by J. Keizer *et al* [51] through a simple fire-diffuse-fire model. Suppose the mean time a site is open is τ, which is directly controlled by [IP$_3$], then apparently the relevant dimensionless constant is $D\tau/d^2$. It is shown that when this constant is much larger than one, the wave propagation is continuous and the speed is proportional to $\sqrt{D\tau}$. However, when it is much less than one (which is the case in calcium signaling), the propagation is saltatory and the speed is proportional to D. The wave speed in *Xenopus* oocytes is $>50\mu$m/s.

The period of spontaneous Ca^{2+} waves is regulated by [IP$_3$] [52]. With very high [IP$_3$], wave period is as short as 7s, which is the recovery time after a cluster is inactivated. For low IP$_3$ level, the period can extend to more than 120 seconds. The measured standard deviation is much less than the mean interwave interval, indicating spontaneous waves are not Poisson processes. A natural assumption is that the gradual elevation of basal Ca^{2+} by puffs increases the probability of wave nucleation at a later time, rather than right after last wave. In chapter III we will study this assumption, and the possible underlying mechanism responsible for the gradual elevation of Ca^{2+} .

II.B.2 Cardiac Excitation-Contraction Coupling

Calcium dynamics plays a central role in cardiac excitation-contraction coupling. During the systolic phase of a heart beat cycle, the plasma membrane is depolarized by a trigger current and further by the activation of Na$^+$ channel. The DHPR is then opened and a small amount of Ca^{2+} ions enter the myoplasm. RyRs are then activated by CICR and a much larger amount of Ca^{2+} is released from SR. Ca^{2+} level in myoplasm is increased to around 1μM. These abundant Ca^{2+} ions activate the myofilaments and cause the contraction of the myocyte. Ca^{2+} release is terminated by the membrane repolarization. The cytosolic Ca^{2+} is pumped back into SR by SERCA or extruded from the cell by sodium-calcium exchanger (NCX) on the membrane. The ratio of the amount of Ca^{2+} released from the SR to the Ca^{2+} entry through DHPR is defined as the gain of excitation-contraction coupling. It is usually larger than 10 under physiological conditions, and depends on the level of membrane depolarization in a graded way. Figure IV.2

shows that under voltage clamp condition, the triggered release from SR is much larger than the Ca^{2+} entry through DHPR, and the gain is a decreasing function of membrane potential.

Early models assume the CICR happens directly in the cytoplasm. There are only two chambers: the cytoplasm and the SR. RyRs are triggered by the mean Ca^{2+} elevation caused by DHPR activation, and release Ca^{2+} from SR. However, such common pool model cannot explain the graded control of Ca^{2+} release by membrane potential. The positive feedback of RyR determines the response is all-or-none. That is, no Ca^{2+} can be released from SR when membrane potential is low, and regenerative Ca^{2+} waves will appear when membrane potential is high, just as we discussed in the IP_3R case. M. D. Stern proposed the local control model to solve this puzzle [53]. Instead of triggering CICR in a common pool, this model assumes there are many local chambers and CICR happens in each chamber independently. The local chambers all connect to the cytoplasm and contribute the local Ca^{2+} release to the global Ca^{2+} . In this way, although the Ca^{2+} release in each local chamber is still all-or-none, their sum can be a smoothly graded function of membrane potential. The key point here is the CICR in one chamber must not affect Ca^{2+} release of other chambers, so Ca^{2+} wave is a phenomenon that is avoided in myocytes under physiological condition.

The geometric distribution of RyR in myocytes has greatly supported the local control theory. Each calcium release unit (CRUs) contains 100-200 RyRs clustering on the end of a junctional SR which is opposed to plasma membrane with only 10-20 nm dyadic clefts between them. There are thousands of such CRUs in one myocyte and they form a very regular lattice, with 2 μm distance between them along the longitudinal direction and 0.4-0.8μm along the transverse direction [54]. When cell membrane is depolarized, the local $[Ca^{2+}]$ in the dyadic space can reach 10-100 μM [55], and the gating of a RyR cluster is essentially of all-or-none style. The release event of such a CRU is called a ”spark” (just like a ”puff” in oocytes). The profiles of all the triggered sparks are similar, but the probability to trigger a spark is a continuous function of membrane potential, thus the total calcium release during systole varies in a graded style with the membrane potential.

There are also spontaneous sparks during diastolic phase. They are harmless under physiological condition because the rate is very small. When the activation threshold of RyR is reduced (for example, by dissociation of FKBP), the channel becomes leaky and the rate of spontaneous sparks increases greatly. On the other hand, this causes a partially depletion of SR Ca^{2+} content in a long term, which results in a reduced RyR Ca^{2+} current. It seems that there is a balance between these two contrary effects: increased RyR open probability and reduced RyR current. In Chapter IV we will see there is an optimal point for excitation-contraction coupling based on the assumption that RyR gating is cooperative, and it suggests that loss of this cooperativity may cause heart failure disease.

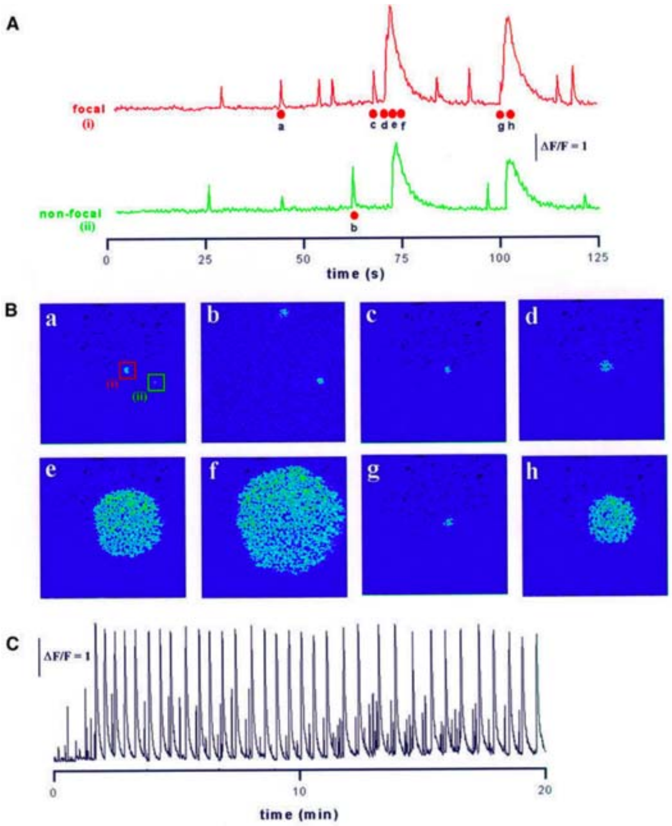

Figure II.1: Induction of puffs and periodic Ca^{2+} waves by sustained photorelease of IP_3 (Marchant and Parker 2001 [52]). (A) Measurements of IP_3 -dependent fluorescence monitored from 8×8 μm regions centered on two puff sites (i and ii) within the imaging field. The UV photolysis light was turned on at the start of the record, and remained on thereafter. Photoreleased IP_3 initially evoked asynchronous puffs at these sites (and at many other sites not shown), and a puff at site (i) triggered a Ca^{2+} wave that propagated throughout the imaging field. Puff activity ceased during the falling phase of the wave, but subsequently recovered until a second wave was again triggered by a puff at site (i). (B) Single image frames illustrating the spatial patterns of cytosolic Ca^{2+} observed at times corresponding to the points marked in (A). The sites from which the traces in (A) were obtained are marked on frame B (a). Panels depict Ca^{2+} -dependent fluorescence on a pseudo-color scale, after subtraction of resting fluorescence before stimulation. (C) Fluorescence trace from site (i) shown on a slower time scale illustrating periodic Ca^{2+} waves during sustained photolysis for 20 min.

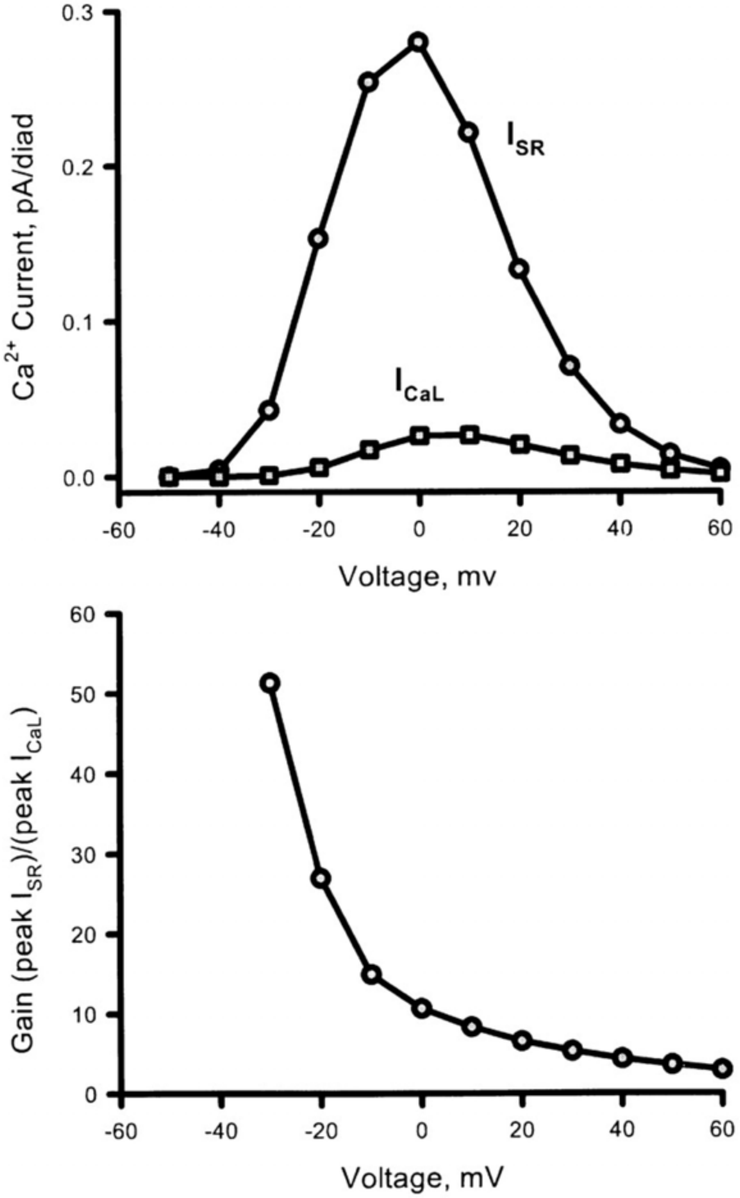

Figure II.2: Simulation results of cardiac graded control by Stern et at [56]. Top: Calcium current through DHPR (I_{CaL}) and RyR (I_{SR}) as functions of membrane potential. Bottom: Excitation-contraction coupling gain is a smooth decreasing function of membrane potential.

Bibliography

[1] Fill, M. & Copello, J. A. (2002) Ryanodine receptor calcium release channels. *Physiol. Rev.* **82,** 893-922.

[2] Coronado, R., Morrissette, J., Sukhareva, M. & Vaughan, D. M. (1994) Structure and function of ryanodine receptors. *Am. J. Physiol. Cell Physiol.* **266,** C1485-C1504.

[3] Block, B. A., Imagawa T., Campbell, K. P. & Franzini-Armstrong, C. (1988) Structural evidence for direct interaction between the molecular components of the transverse tubule/sarcoplasmic reticulum junction in skeletal muscle. *J. Cell Biol.* **107,** 2587-2600.

[4] Franzini-Armstrong, C. (1970) Studies of triad I structure of the junction in frog twitch fibers. *J. Cell Biol.* **47,** 488-499.

[5] Ikemoto, N., Antoniu B., & Kim, D. H. (1984) Rapid calcium release from the isolated sarcoplasmic reticulum is triggered via the attached transverse tubular system. *J. Biol. Chem* **259,** 13151-13158.

[6] Lam G. D. (1992) DHP receptors and excitation-contraction coupling. *J. Muscle Res. Cell Motil.* **13,** 394-405.

[7] Bers D. (2001) Excitation-contraction coupling and cardiac contractile force. Kluwer, Boston.

[8] Dumollard, R., Carroll, J., Dupont, G., & Sardet, C. (2002) Calcium wave pacemakers in eggs. *J. Cell Sci.* **115,** 3557-3564.

[9] Webb, S. E., & Miller, A. L. (2003) Calcium signalling during embryonic development. *Nat. Rev. Mol. Cell Biol.* **4,** 539-551.

[10] Marks, A. R. (1997) Intracellular calcium-release channels: regulators of cell life and death. *Am. J. Physiol.* **272,** H597-H605.

[11] Inoue, T., Kato K. & Mikoshiba, K. (1999) Type I inositol 1,4,5-trisphosphate receptor is required for induction of long-term depression in cerebellar Purkinje neurons. *J. Neurosci.* **18,** 5366-5373.

[12] Nishiyama, M., Hong K., Mikoshiba, K., Poo, M.-M. & Kato, K. (2000) Calcium stores regulate the polarity and input specificity of synaptic modification. *Nature* **408,** 584-588.

[13] Jiang, Q.-X., Thrower, E. C., Chester, D. W., Ehrlich, B. E. & Sigworth, F. J. (2002) Three-dimensional structure of the type 1 inositol 1,4,5-trisphosphate receptor at 24Åresolution. *EMBO* **21,** 3575-3581.

[14] Bosanac, I., Alattia, J.-R., Mal, T. K., Chan, J., Talarico, S., Tong, F. K., Tong, K. I., Yoshikawa, F., Furuchi, T., Iwai, M., Michikawa, T., Mikoshiba, K. & Ikura, M. (2002) Sturcture of the inositol 1,4,5-trisphosphate receptor binding core in complex with its ligand. *Nature* **420,** 696-700.

[15] Berridge, M. J., Lipp, P. & Bootman, M. D. (2000) The versatility and universality of calcium signalling. *Nat. Rev. Mol. Cell Biol.* **1,** 11-21.

[16] Berridge, M. J., Bootman, M. D. & Roderick, H. L. (2003) Calcium signalling: dynamics, homeostasis and remodelling. *Nat. Rev. Mol. Cell Biol.* **4,** 517-529.

[17] Keener, J. P. & Sneyd, J. (1998) Mathematical physiology. Springer, New York.

[18] De Young, G. W. & Keizer, A. (1992) A single pool IP_3-receptor based model for agonist stimulated Ca^{2+} oscillations. *Proc. Natl. Acad. Sci.* **89,** 9895-9899.

[19] Li, X.-Y. & Rinzel, J. (1994) Equations for InsP3 receptor-mediated [Ca^{2+}] oscillations derived from a detailed kinetic model a Hodgkin-Huxley like formalism. *J. Theor. Biol.* **166,** 461-473.

[20] Laver, D. R., Baynes T. M. & Dulhunty, A. F. (1997) Magnesium inhibition of ryanodine-receptor calcium channels: evidence for two independent mechanisms. *J. Membrane Biol.* **156,** 213-229.

[21] Meissner, G. (1994) Ryanodine receptor/Ca^{2+} release channels and their regulation by endogenous effectors. *Annu. Rev. Physiol.* **56,** 485-508.

[22] Zahradnikova, A., Dura M., Gyorke, I, Escobar, A. L. Zahradnik, I. & Gyorke, S. (2003) Regulation of dynamic behavior of cardiac ryanodine receptor by Mg^{2+} under simulated physiological conditions. *Am. J. Physiol. Cell Physiol.* **285,** C1059-C1070.

[23] Brillantes A. B., Ondrias, K., Scott, A., Kobrinsky, E., Ondriasova, E., Moschella, M. C., Jayaraman, T., Landers, M., Ehrlich, E. E. & Marks, A. R. (1994) Stabilization of calcium release channel (ryanodine receptor) function by FK506-binding protein. *Cell* **77,** 513-523.

[24] Ahern, G. P., Junankar, P. R. & Dulhunty, A. F. (1997) Subconductance states in single-channel activity of skeletal muscle ryanodine receptors after removal of FKBP12. *Biophys. J.* **72,** 146-162.

[25] Marx, S. O., Reiken, S., Hisamatsu, Y., Jayaraman, T., Burkhoff, D., Rosemblit, N. & Marks, A. R. (2000) PKA phosphorylation dissociates FKBP12.6 from the calcium release channel (ryanodine receptor): defective regulation in failing hearts. *Cell* **101,** 365-376.

[26] Ono, K., Yano, M., Ohkusa, T., Kohno, M., Hisaoka, T., Tanigawa, T., Kobayashi, S., Kohno, M. & Matsuzaki, M. (2000) Altered interaction of FKBP12.6 with ryanodine receptor as a cause of abnormal Ca(2+) release in heart failure. *Cardiovasc. Res.* **48,** 323-331.

[27] Marx, S. O., Reiken, S., Hisamatsu, Y., Jayaraman, T., Burkhoff, D., Rosemblit, N. & Marks, A. R. (2000) PKA phosphorylation dissociates FKBP12.6 from the calcium release channel (ryanodine receptor): defective regulation in failing hearts. *Cell* **101,** 365-376.

[28] Jiang, M. T., Lokuta, A. J., Farrell, E. F., Wolff, M. R., Haworth, R. A. & Valdivia, H. H. (2002) Abnormal Ca2+ release, but normal ryanodine receptors in canine and human heart failure. *Circ. Res.* **91,** 1015-1022.

[29] Xiao, B., Sutherland, C., Walsh, M. P. & Chen, S. R. W. (2004) Protein kinase A phosphorylation at serine-2808 of the cardiac Ca2+-release channel (Ryanodine receptor) does not dissociate 12.6-kDa FK506-binding protein (FKBP12.6). *Circ. Res.* **94,** 487-495.

[30] Lokuta, A. J., Meyers, M. B., Sander, P. R., Fishman, G. I. & Valdivia, H. H. (1997) Modulation of cardiac ryanodine receptors by sorcin. *J. Biol. Chem.* **272,** 25333-25338.

[31] Suarez, J., Belke, D. D., Gloss, B., Dieterle, T., McDonough, P. M., Kim, Y.-K., Brunton, L. L. & Dillmann, W. H. (2004) . *Am. J. Physiol. Heart Circ. Physiol.* **286,** H68-H75.

[32] Kass, R. S. & Sanguinetti, M. C. (1984) Inactivation of calcium channel current in the calf cardiac Purkinje fiber: evidence for voltage- and calcium mediated mechanisms. *J. Gen. Physiol.* **84,** 705-726.

[33] Lee, K. S., Marban, E. & Tsien, R. W. (1985) Inactivation of calcium channels in mammalian heart cells: joint dependence of membrane potential and intracellular calcium. *J. Physiol.* **364,** 395-411.

[34] Jafri, M. S., Rice J. J. & Winslow, R. L. (1998) Cardiac Ca^{2+} dynamics: the roles of ryanodine receptor adaptation and sarcoplasmic reticulum load. *Biophys. J.* **74,** 1149-1168.

[35] Stern, M. D., Song, L.-S., Cheng, H. & Sham, J. S. K. (1999) Local control models of cardiac excitation-contraction coupling: a possible role for allosteric interactions between ryanodine recepors. *J. Gen. Physiol.* **113,** 469-489.

[36] Bondarenko, V. E., Szigeti G. P., Bett, G. C. L., Kim, S.-J. & Rasmusson, R. L. (2004) Computer model of action potential of mouse ventricular myocytes. *Am. J. Physiol. Heart. Circ. Physiol.* **287,** H1378-H1403.

[37] Inesi, G., Kurzmack, M. & Lewis, D. (1988) Kinetic and equilibrium characterization of an energy-transducing enzyme and its partial reactions. *Methods Enzymol.* **157,** 154-190

[38] Shannon, T. R., Wang, F., Puglisi, J., Weber, C. & Bers, D. M. (2004) A mathematical treatment of integrated Ca dynamics within the ventricular myocyte. *Biophys. J.* **87,** 3351-3371

[39] Lytton, J., Westlin, M., Burk, S. E., Shull, G. E. & MacLennan, D. H. (1992) Functional comparisons between isoforms of the sarcoplasmic or endoplasmic reticulum family of calcium pumps. *J. Biol. Chem.* **267,** 14483-14489

[40] Reeves, J. P. & Hale, C. C. (1984) The stoichiometry of the cardiac sodium-calcium exchange system. *J. Biol. Chem.* **259,** 7733-7739.

[41] Luo, C.-H. & Rudy, Y. (2004) A dynamic model of the cardiac ventricular action potential. I. Simulations of ionic currents and concentration changes. *Circ. Res.* **74,** 1071-1096.

[42] Falcke, M. (2003) Buffers and oscillations in intracellular Ca2+ dynamics. *Biophys. J.* **84,** 28-41

[43] Iyer, V., Mazhari, R. & Winslow, R. L. (2004) A computational model of the human left-ventricular epicardial myocyte. *Biophys. J.* **87,** 1507-1525.

[44] Yao, Y., Choi J. & Parker, I. (1995) Quantal puffs of intracellular Ca^{2+} evoked by inositol trisphosphate in *Xenopus* oocytes. *J. Physiol.* **482,** 533-553.

[45] Swillens, S., Dupont G., Combettes, L. & Champeil, P. (1999) From calcium blips to calcium puffs: theoretical analysis of the requirements for interchannel communication. *Proc. Natl. Acad. Sci.* **96,** 13750-13755.

[46] Shuai, J., Rose H. J. & Parker, I. (1997) The number and spatial distribution of IP_3 receptors underlying calcium puffs in *Xenopus* oocytes. *Biophys. J.* **91,** 4033-4044.

[47] Marchant, J., Callamaras N. & Parker, I. (1999) Initiation of IP_3 -mediated Ca^{2+} waves in *Xenopus* oocytes *EMBO* **18,** 5285-5299.

[48] Albritton, N. L., Meyer T. & Streyer, L. (1992) Range of messenger action of calcium ion and inositol 1,4,5-trisphosphate. *Science* **258,** 1812-1815.

[49] Shuai, J. W. & Jung, P. (2002) Optimal ion channel clustering for intracellular calcium signaling. *Proc. Natl. Acad. Sci.* **100,** 506-510.

[50] Shuai, J. W. & Jung, P. (2003) Selection of intracellular calcium patterns in a model with clustered Ca^{2+} release channels. *Phys. Rev. E* **67,** 031905.

[51] Keizer, J., Smith G. D., Ponce-Dawson, S. & Pearson, J. E. (1998) Saltatory propagation of Ca^{2+} waves by Ca^{2+} sparks. *Biophys. J.* **75,** 595-600.

[52] Marchant, J. S. & Parker, I. (2001) Role of elementary Ca^{2+} puffs in generating repetitive Ca^{2+} oscillations. *EMBO J.* **20,** 65-76

[53] Stern, M. D. (1992) Theory of excitation-contraction coupling in cardiac muscle. *Biophys. J.* **63,** 497-517

[54] Izu, L. T., Wier, W. G. & Balke, C. W. (2001) Evolution of cardiac calcium waves from stochastic calcium sparks. *Biophys. J.* **80,** 103-120

[55] Soeller, C. & Cannell, M. B. (1997) Numerical simulation of local calcium movements during L-type calcium channel gating in the cardiac diad. *Biophys. J.* **73,** 97-111

[56] Stern, M. D., Song, L. S., Cheng, H., Sham, J. S., Yang, H. T., Boheler, K. R. & Rios,E. (1999) Local control models of cardiac excitation-contraction coupling. A possible role for allosteric interactions between ryanodine receptors. *J. Gen. Physiol.* **113,** 469-489.

III

Stochastic Calcium Waves in *Xenopus* Oocytes

III.A Introduction

In many cell types, Ca^{2+} is released from the ER through the opening of the inositol (1,4,5)-triphosphate (IP_3) receptors (IP_3Rs). These receptors are clustered at sites [2, 3] which are positioned randomly on the ER membrane with a distance of $\sim 5-8$ μm [4]. The binding of IP_3 and Ca^{2+} results in the opening of a channel which is inactivated for very high concentrations of Ca^{2+}. Through the use of novel experimental techniques that permit the visualization of subcellular events, it has become clear that Ca^{2+} dynamics can be a highly localized process. Release events, during which the IP_3Rs open and release Ca^{2+} from the ER into the cytosol, can be limited to single clusters ("puffs" or "sparks") or even single channels ("blips") [2, 5]. Furthermore, it has become clear that these release events exhibit a large degree of stochasticity [6, 2]. The increase in Ca^{2+} concentration due to a puff from one cluster can initiate the opening of neighboring clusters. The subsequent further increase in local Ca^{2+} concentration can then lead to a global Ca^{2+} wave.

A recent experimental study by Marchant *et al.* [4] examined spontaneous global Ca^{2+} waves in unfertilized Xenopus oocytes for different IP_3 concentrations. In particular, they found global waves with mean inter-wave intervals ranging from 8 s, for the highest IP_3 concentration, to 120 s for the lowest IP_3 concentration. The standard deviations for these inter-wave intervals were found to be significantly smaller than their mean and ranged from < 2 s to ~ 25 s. Furthermore, for the global events with large inter-wave intervals, the average cytosolic Ca^{2+} concentration was observed to increase slowly between two waves. In contrast, the puff rate only increased during the first part of a wave cycle and then reached a sustained level.

The relatively small standard deviation observed in the experiments indicates that the puffs, which are the building blocks of the global events, are not uncoupled. After all, if the puffs were independent of the history of the system, the global events could be described by a Poisson process. Then, the distribution of mean inter-wave intervals would be exponential and the measured standard deviation should equal the measured mean inter-wave interval. Conversely, a mechanism which makes global events progressively more likely to occur as the system generates puffs would be able to explain the observed data.

In this chapter, we investigate the possibility that the slow increase of the average Ca^{2+} concentration is related to the small standard deviations in the inter-wave intervals and study possible sources for this slow increase. Our basic hypothesis is that this slow rise will increase the probability that cluster openings lead to global waves. Thus, the probability of the nucleation process for a global wave will be an increasing function of time and the standard deviation will be reduced.

We address this hypothesis via the simulation of a simple computational model for Ca^{2+} dynamics. Several groups have presented detailed models of intracellular Ca^{2+} dynamics, taking into account spatial localization of the IP_3 receptor clusters [7, 8, 9]. These models have been helpful in furthering our understanding of Ca^{2+} dynamics. However, their complexity makes it difficult to investigate the essential processes involved in certain experimental observations. For this reason, we have chosen to study a very simple model, with as goal to capture the physical mechanism that can lead to mean inter-wave intervals with small standard deviations, as caused by a slow rise in cytosolic Ca^{2+} between two successive waves. As we will see, our approach leads to the conclusion that a model consisting of a diffusive coupling between the receptor clusters, combined with *instantaneously* activated pumps on the ER is not able to explain the experimental data. Specifically, it is unable to produce both a slow cytosolic Ca^{2+} rise and a sufficient reduction in cytosolic Ca^{2+} after a global event. Thus, our model needs to incorporate an additional mechanism and we show that incorporating a pump which slowly activates is one possible way to account for the experimental findings.

III.B The Ca^{2+} model

The basic elements of Ca^{2+} dynamics include diffusion through the cytosol, release from the ER through IP_3Rs and the uptake into ER through SERCA pumps. Thus, we start with the reaction-diffusion equation

$$\frac{\partial[Ca^{2+}]}{\partial t} = J_{release} - J_{uptake} + D\nabla^2[Ca^{2+}] \qquad \text{(III.1)}$$

where D is the Ca^{2+} diffusion constant. We have chosen a two-dimensional $150\times150\ \mu m$ square computational domain with zero-flux boundary conditions; this is large enough to study large scale calcium dynamics. The first term of this equation models the release of Ca^{2+} from the IP_3Rs. Instead of using a detailed channel model as in previous studies [10, 11, 12, 13], we use a simple point-source description which reads

$$J_{release} = \nu_r \sum_{i,j} \delta\left(\overrightarrow{x} - \overrightarrow{x}_i\right) \delta\left(t - t_i^j\right) \qquad \text{(III.2)}$$

where $\overrightarrow{x}_i$ is the position of a cluster site, and t_i^j gives the time of the jth puff at site $\overrightarrow{x}_i$. (see also ref. [14]). The cluster sites are located on a square grid with a grid spacing of d =6 μm. During each puff a constant amount of Ca^{2+}

is released instantaneously. Estimated from experiments[2], the amount is chosen here as $\nu_r = 70\ \mu M/\mu m^2$.

Stochasticity is built in the model via the description of the "firing" times t_i^j. To this end, we associate with each cluster site a stochastic controlling variable θ and generate a puff at that site when the value of this variable exceeds a threshold, θ_{th}. The fact that the firing is controlled by Ca^{2+} (the well-known CICR mechanism [5]), is incorporated by making this threshold a function of the Ca^{2+} concentration. In general we expect this dependence to be sigmoidal, corresponding to a high, baseline threshold at low concentration dropping to a low threshold at high concentration. Here we take the simplest caricature,

$$\begin{aligned} \theta_{th} &= \theta_{th,0} \quad \text{for} \quad \mathrm{Ca}^{2+} < \mathrm{Ca}^{2+}_{\mathrm{th}} \\ \theta_{th} &= -\infty \quad \text{for} \quad \mathrm{Ca}^{2+} \geq \mathrm{Ca}^{2+}_{\mathrm{th}} \end{aligned} \tag{III.3}$$

In other words, for Ca^{2+} levels exceeding $\mathrm{Ca}^{2+}_{\mathrm{th}}$ the threshold becomes infinitely low and the cluster will fire with probability 1, which will be called a triggered puff. For Ca^{2+} levels below $\mathrm{Ca}^{2+}_{\mathrm{th}}$ the cluster will only release Ca^{2+} when θ exceeds $\theta_{th,0}$, which will be called a spontaneous puff. To incorporate a refractory period we specify that after a threshold crossing θ is reset to 0 where it remains for a fixed period of time. The equation for θ reads:

$$d\theta = -\Gamma\theta dt + \sigma dW \tag{III.4}$$

where W is a standard Wiener process and where the positive Γ ensures a stochastic process centered around 0. In the following, we have fixed $\theta_{th,0} = 1.05$, $\Gamma = 1\ s^{-1}$, and $\sigma = 0.2\ s^{-1/2}$. The refractory period is set to $7s$, following the minimum period seen in Parker's data[4]. We will vary the Ca^{2+} threshold to mimic the effect of varying IP_3 in the experiments.

The second term in our equation describes the uptake of the cytosolic Ca^{2+} into the ER via the SERCA pumps. We assume that the pumps are uniformly distributed on the ER membrane and that the uptake can be described by

$$J_{uptake} = r_u[\mathrm{Ca}^{2+}] \tag{III.5}$$

As we will discuss below, the exact form of the pumping rate r_u might play a determining role in the distribution of inter-wave intervals. We will assume here that r_u obeys a first order reaction

$$\tau_u \frac{\partial r_u}{\partial t} = \nu_u[\mathrm{Ca}^{2+}] - \left([\mathrm{Ca}^{2+}]^2 + \mathrm{K}_\mathrm{u}^2\right) \mathrm{r}_\mathrm{u} \qquad \text{(III.6)}$$

The parameter τ_u controls the time scale of the pump kinetics and we will consider two cases. The first one, customarily used in modeling studies and which we will call ultra-fast SERCA kinetics, is the limit of large τ_u. In this case, r_u reaches equilibrium very quickly and J_{uptake} can be described by $J_{uptake} = \nu_u[Ca^{2+}]^2/([Ca^{2+}]^2 + K_u^2)$. This Hill function form of J_{uptake} has been seen experimentally and we have chosen the values of the parameters to be consistent with measured data [16, 15, 17] and theoretical models [18, 7]: $\nu_u = 0.5\ \mu M/s$, and $K_u = 0.31\ \mu M$. The second case investigated here corresponds to taking a finite value of τ_u. In this case, we can no longer use the steady state solution for r_u, which now has to be solved explicitly through Eq. III.6. We will call this case slow SERCA kinetics and we have chosen $\tau_u = 1.25s$.

The last term in our equation describes the diffusion of free Ca^{2+}. In reality, most of the cytosolic calcium is bound by calcium buffer proteins. Generally, the buffers are present in large concentrations and have fast binding kinetics relative to the time scale of global calcium waves. Therefore, we assume that the buffers are always in equilibrium with free Ca^{2+}. This assumption can be shown to result in a simple renormalization of the diffusion constant which we take $D = 25\ \mu m^2/s$, a value that falls within the experimentally observed range [19].

III.C Results

Ultra-fast SERCA kinetics We start by showing in Fig. III.1 several typical snapshots of the Ca^{2+} concentration field as simulated by the model with ultra-fast SERCA kinetics. These snapshots are qualitatively similar to those using slow SERCA kinetics (data not shown). The Ca^{2+} concentration is shown on a gray scale with white corresponding to high and black corresponding to low Ca^{2+} concentrations. Initially there is no activity in the entire region, as we start our simulation with all θ's set to zero and with a uniform zero Ca^{2+} concentration (Fig. III.1*a*). Gradually, some stochastic puffs appear, as shown by the small white circles in Fig. III.1*b*. These puffs can then trigger neighboring cluster sites to open (right side in Fig. III.1*c*), which releases more Ca^{2+}. This, in turn, will trigger more neighboring sites to open (Fig. III.1*d*) and a global calcium wave is initiated (Fig. III.1*e,f*). This wave was found to propagate with a wave speed of approximately 15 $\mu m/s$, which falls into the measured velocity region. [20, 21]. After the wave has swept through the entire computational domain (Fig. III.1*g*), almost all the puff sites have been triggered and thereby entered the refractory period (Fig. III.1*h*). During this refractory period, no puffs are generated while Ca^{2+} is continuously pumped back into ER by the SERCA pumps. After the refractory period, a new cycle can begin.

Fig. III.2 shows a full simulation run for ultra-fast SERCA kinetics. The calcium concentration shown in Fig. III.2A is an average over the whole computational domain. Unlike the experiments, it is obviously very irregular. In Fig. III.3 we show the mean of the inter-wave intervals, along with its standard deviation, as a function of $[Ca^{2+}]_{th}$. Each simulation was run for a long enough time so that at least 100 global waves were counted. As in the experiments, the mean increases from 10 s, close to the refractory period, to 100 s as the Ca^{2+} threshold, which is inversely related to the IP_3 concentration, is increased. As seen, the standard deviation is roughly equal to the mean of the inter-wave interval plus the refractory period, which is much larger than the one observed in the experiments. This indicates that the global waves are uncoupled and can be described by a Poisson process (supplemented by a refractory period). This is further illustrated by Fig. III.4 where we plot the distribution of inter-wave intervals for the simulation shown in Fig. III.2. As demonstrated by the solid line, which is obtained through a two parameter fit $A\exp(-(T-7)/(T_0-7)$, the distribution is well described by an exponential, a hallmark of the Poisson process.

As mentioned above, our basic hypothesis is that the slow rise in background Ca^{2+} is important in limiting the variance. Our model so far is consistent with this claim which is shown in Fig. III.2B, where we plot the background Ca^{2+} concentration as a function of wave phase between two global waves. The background concentration was measured by averaging the concentration over the whole simulated region and over 250 different inter-wave intervals. Contrary to the experiments, the simulations show no discernible rise in the background Ca^{2+} concentration. It is therefore not surprising that the global waves are completely Poissonian. Finally, for completeness we show in Fig. III.2C the corresponding puff rate, defined as the average number of puffs per second. The puff rate following a global wave increases during the first 1/5 wave cycle and then reaches a steady state level until another global wave occurs.

Let us now address why the ultra-fast kinetics fails to describe the experimental findings. For ultra-fast kinetics, the Ca^{2+} released in a puff will be pumped backed into the ER very quickly. This is illustrated in Fig. III.5A where we have plotted as a dashed line the Ca^{2+} concentration as a function of time at the release site for the case of ultra-fast kinetics. The Ca^{2+} concentration reaches an almost constant level very quickly after the release. Thus, unless the pump rate is very low, the Ca^{2+} is prevented from diffusing far from the release site (see Fig. III.5B) and the global background Ca^{2+} will not exhibit a slow increase over time. Consequently, the puff sites will always fire independently and the probability for a global event remains constant over time.

One obvious way to prevent the Ca^{2+} from being pumped back into the ER is to reduce the pump rate via the reduction of ν_u. However, reducing this rate also reduces the ability of the pumps to reduce the Ca^{2+} concentration after a global event. We found, through extensive numerical experiments, that reducing the value of ν_u results in Ca^{2+} concentration that are above or very close to the

Ca^{2+} threshold after a global event. Thus, this reduction was always accompanied by a significant decrease in the inter-wave interval. One could not get long inter-wave intervals together with weak pumping. Thus, a new mechanism is needed.

Slow SERCA kinetics A possible mechanism that will permit large inter-wave intervals coupled with background Ca^{2+} concentrations that accumulate slowly between global events is the inclusion of slow SERCA kinetics. The slow kinetics ensures that after a release event, the pump activity is initially not very high and the released Ca^{2+} can diffuse away from the cluster site. This leads to a slow build-up of background Ca^{2+}, which reduces the threshold for firing and which leads to global waves with a large mean and a small standard deviation. On the other hand, by choosing the time scale of the kinetics to be smaller than the refractory period, the pumps are still able to efficiently bring the Ca^{2+} concentration to small levels after a global event.

To verify this qualitative picture, we have performed a series of numerical simulations. Fig. III.6A shows a sample simulation of slow SERCA kinetics with roughly the same mean inter-wave interval as in Fig. III.2. But in this simulation, global waves are much more regular compared to the case of ultra fast kinetics, and each global wave is indeed preceded by a slow background increase. Furthermore, in Fig. III.7 we show the mean of the inter-wave intervals and its standard deviation as a function of $[Ca^{2+}]_{th}$. As in the case of ultra-fast kinetics, the mean inter-wave intervals ranges from 10 s to 90 s but now the standard deviation is much smaller and comparable to the experimental one. In Fig. III.8 we show the distribution of inter-wave intervals based on 172 global events. The inter-wave interval is clearly not exponentially distributed and thus the global wave generation can no longer be described by a Poisson process.

Our hypothesis claims that the probability for the occurrence of a global event depends on the background Ca^{2+} concentration. In Fig. III.6B we plot the background Ca^{2+} concentration, again measured by averaging $[Ca^{2+}]$ over the whole simulated region and over 172 global events. As in the experiment, the background Ca^{2+} concentration rises slowly by about 0.01μ M between two global events. This cumulative increase of Ca^{2+} should lead to an increased wave nucleation probability. It is important to note, though, that, as in the experiments the simulated puff rate (shown in Fig. III.6C) does not change significantly during the latter parts of the wave cycle. This is because most of the puffs are spontaneous and independent of each other. However, during a nucleation process, all the involved puffs are correlated via the Ca^{2+} concentration. Therefore, the distribution of the "triggered puffs" should be a proper measure of the effect of the background Ca^{2+} level. In Fig. III.9 we show the distribution of triggered events for both cases. The distribution shown here is confined by the distribution of global waves because we cannot measure the appearance times of triggered puffs which are longer than the intervals of global waves. The distribution for ultra-fast SERCA kinetics shows that nucleation processes are likely to occur during both the early and late stages of an interwave interval. On the contrary, Fig. III.9B demonstrates that the nucleation probability for slow SERCA kinetics is an increasing function of time and is vanishingly small immediately following a global event.

To further elucidate the contribution of slow SERCA kinetics to the background Ca^{2+} increase, we have plotted in Fig. III.5A as a solid line the Ca^{2+} concentration as a function of time at the release site for the case of slow kinetics. Contrary to the case of ultra-fast kinetics (dashed line), the Ca^{2+} concentration at the release site decays slowly. In Fig. III.5B we plot the Ca^{2+} concentration as a function of time at the cluster site that neighbors a site from which Ca^{2+} is released at $t = 0$ s. As expected, slow SERCA kinetics (solid line) results in a much higher Ca^{2+} concentration in the cytoplasm during a puff than does ultra-fast kinetics (dashed line).

III.D Discussion

Our results are two-fold. First, we show that a new mechanism is needed to account for the slow rise in global Ca^{2+} during the inter-wave period. We propose that a simple possibility is afforded by relaxing the usual assumption of instantaneous SERCA pump activation. The detailed kinetics of the pumps have been measured for both SERCA1 [22, 23] and for SERCA3 [24]. An estimate based on kinetic parameters of SERCA1 shows that the typical time scale for the pump to reach a new equilibrium working state upon a rapid change in the cytosolic Ca^{2+} concentration is about 0.1 s, which is much smaller than we postulated in our model. However, the major isoform of SERCA in Xenopus oocytes is SERCA2b, which is proving to be very different from the other isoforms due to its higher sensitivity to calcium and slower turnover rate [16, 25]. Moreover, a very recent study on the kinetics of SERCA2b shows that some of the reaction steps of SERCA2b are much slower than their counterparts in SERCA1 and SERCA3 [26]. Although more work is needed, the current experimental data strongly supports the possibility of slow pump kinetics.

The second result concerns the necessity and sufficiency of the slow Ca^{2+} rise in limiting the variance of the inter-wave interval. The sufficiency is clear, but the question if whether this is the only possible mechanism is more complicated. After all, this necessity has been shown in a model which is rather simple and in particular ignores the detailed biochemistry involved in the channel dynamics. We have verified that relaxing some of the simplifying assumptions in our model (such as the all-or-none nature of the puff) do not alter any of our conclusions, but it is hard to check all possible modifications. In the work of Falcke [8] who studied global oscillations using the deYoung-Keizer kinetics [11], there is some limitation in the variance as compared to the mean due to what appears to be an effective increase in the refractory period as IP_3 is lowered. His simulations do not show the slow background rise and therefore the interval distribution presumably remains exponential after the refractory period. It should therefore be straightforward in principle to distinguish the single-puff biochemical effects as seen in his work from the inter-puff coordination effects seen in our model.

There are of course issues that need to be addressed in future work with our model. Foremost among these is the role of the third dimension, i.e. the fact that Ca^{2+} can diffuse away from the ER membrane. This could change somewhat the nature of the global waves and needs to be carefully studied. Additionally, one can consider the effects of slow buffers as that can have a large effect on coupling between puff sites (see [9]). Finally, one can imagine applying our framework to cells other than the Xenopus oocyte, including hepatocytes in which IP_3 dynamics may play a more critical role in the oscillations [27].

Our model suggests several new directions for experiments. First, it is clear that the most important diagnostic of the global wave nucleation mechanism is the interval distribution function. Different models lead to very different distributions, which offers a way to examine their validity in experiments. Next, we predict that altering SERCA kinetics either pharmacologically or genetically would lead to changes in global oscillation behavior - faster pumps mean more randomness in the oscillations and less Ca^{2+} accumulation. Finally, measuring the spatial correlations among puff sites (our notion of the "triggered" as opposed to "spontaneous" puff) should reveal how global waves are organized from their fundamental constituents.

III.E Acknowledgements

The text of chapter III, in part, is a reprint of the material as it appears in Kai Wang, Wouter-Jan Rappel, and H. Levine, *Cooperativity can reduce stochasticity in intracellular calcium dynamics*, Phys. Biol. **1**, 27, © Institute of Physics and IOP Publishing Limited, where the dissertation author was the first author. The co-authors in this publication directed, supervised, and co-worked on

the research which forms the basis of this chapter.

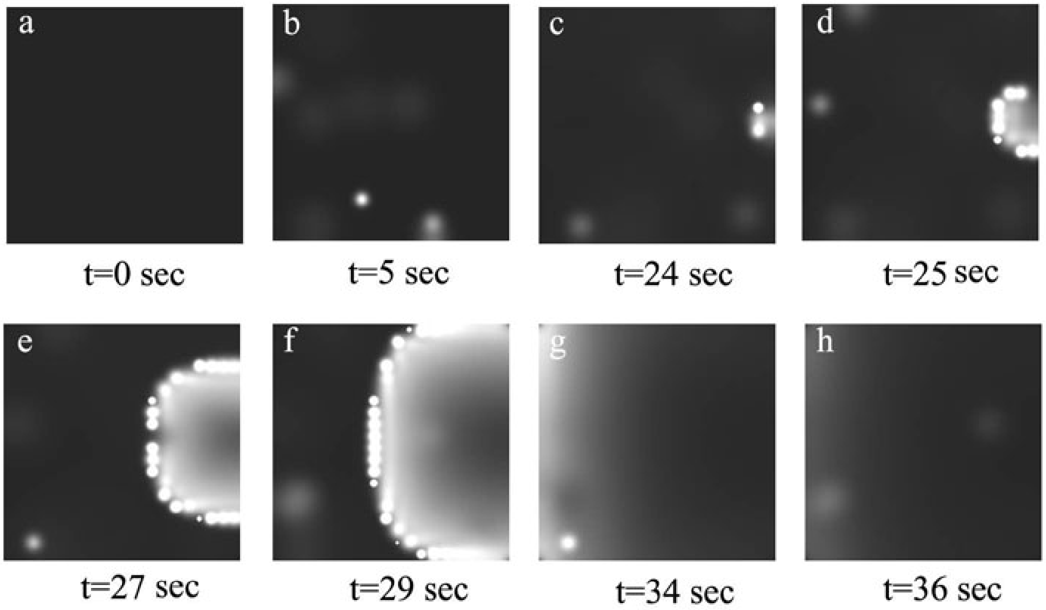

Figure III.1: Snapshots of calcium puffs and a global calcium wave simulated by the model with ultra-fast SERCA kinetics within a 150×150 μm region. After many stochastic puffs, a global wave is initiated from the right side of the region and spreads over the whole region in about 10 seconds.

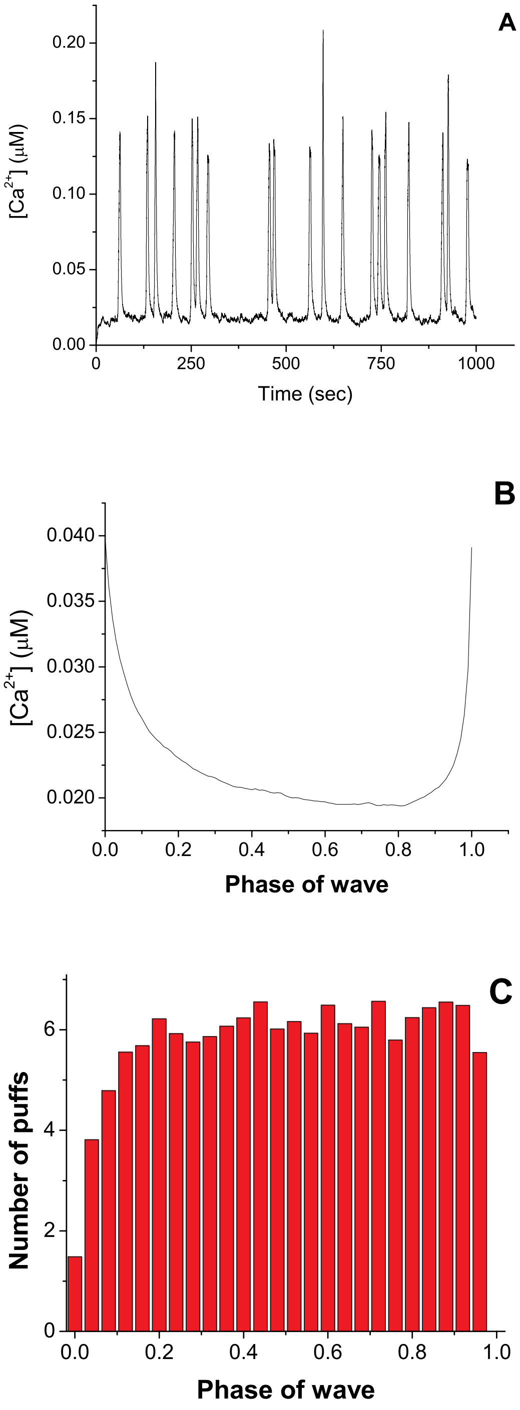

Figure III.2: Cytosolic calcium concentration exhibits irregular global oscillations for the case of ultra-fast SERCA kinetics with $[\mathrm{Ca}^{2+}]_{th} = 0.1\mu M$. A: a trace of $[\mathrm{Ca}^{2+}]$ for the first 1000 s. B: cytosolic calcium level averaged over 250 interwave intervals as a function of a rescaled wave phase beginning immediately after a global wave. C: corresponding averaged puff frequency as a function of wave phase.

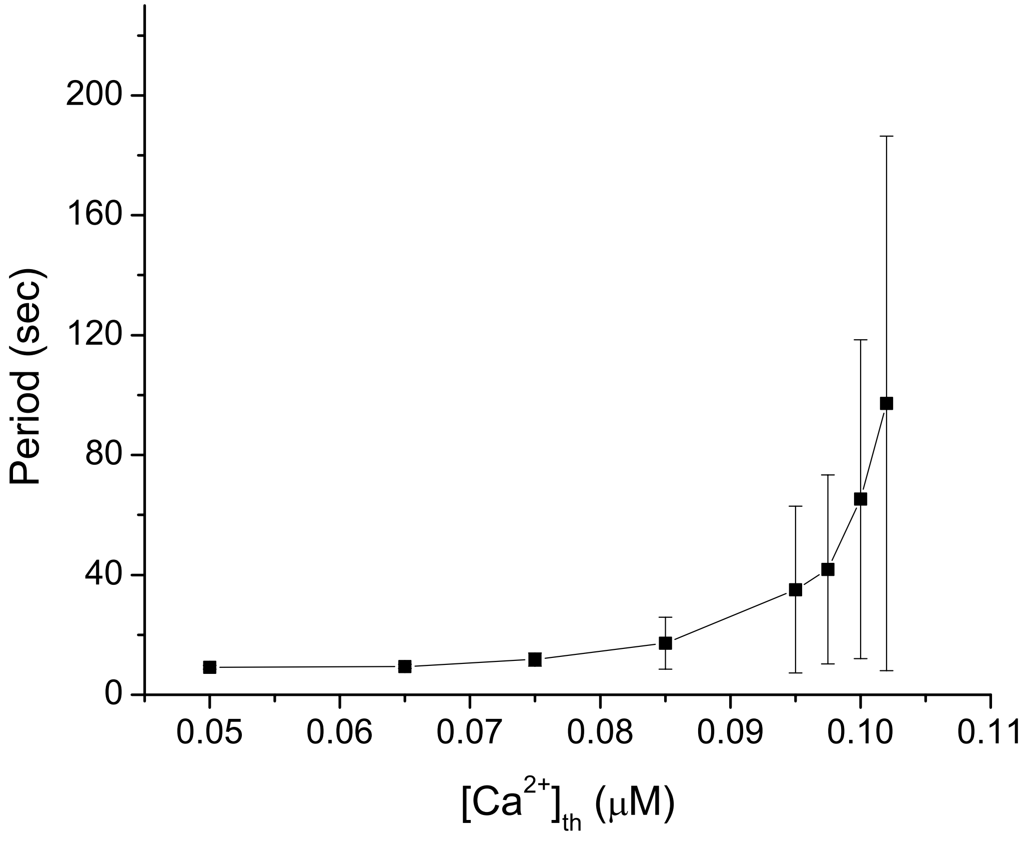

Figure III.3: The mean and standard deviation of inter-wave intervals as a function of $[\mathrm{Ca}^{2+}]_{th}$ for the model with ultra-fast SERCA kinetics.

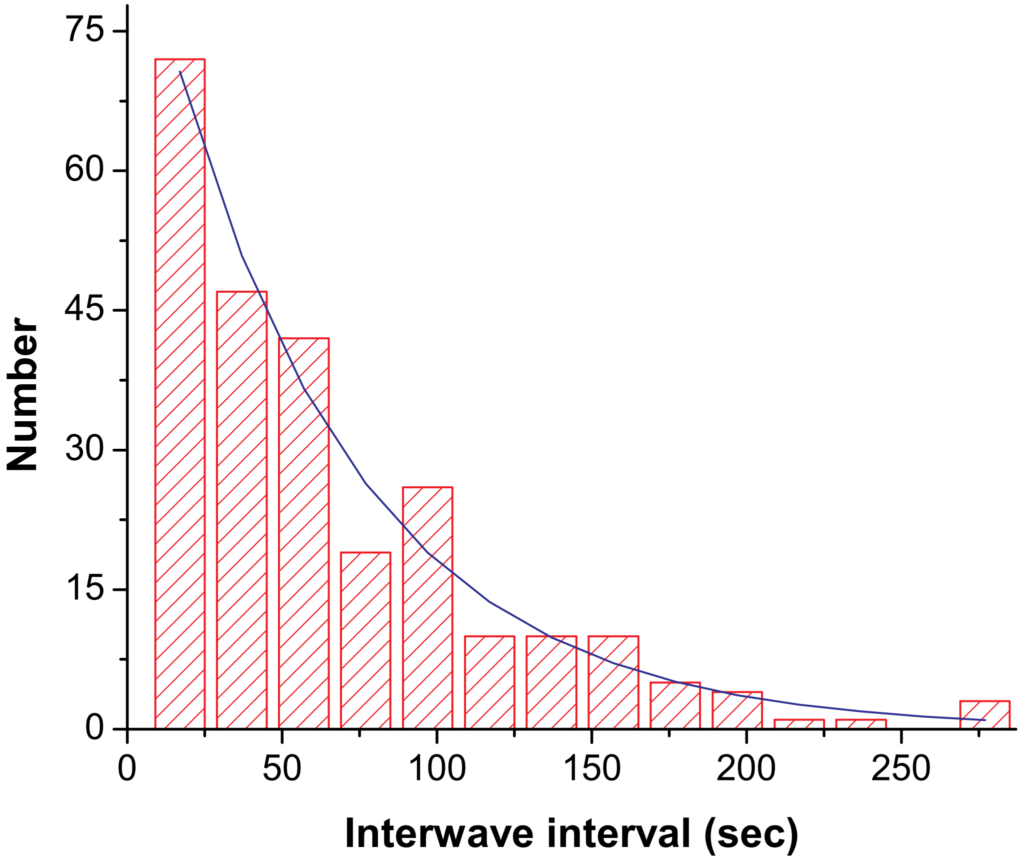

Figure III.4: The distribution of inter-wave intervals for the ultra-fast SERCA kinetics case and $[\mathrm{Ca}^{2+}]_{th} = 0.1\mu M$. The mean inter-wave interval for this distribution is $65.3s$ while the standard deviation is 53.2s. It fits well to an exponential distribution $A\exp(-(T-7)/(T_0-7))$. The value of the fitting parameters are $A =$ and $T_0 = 67.9s$.

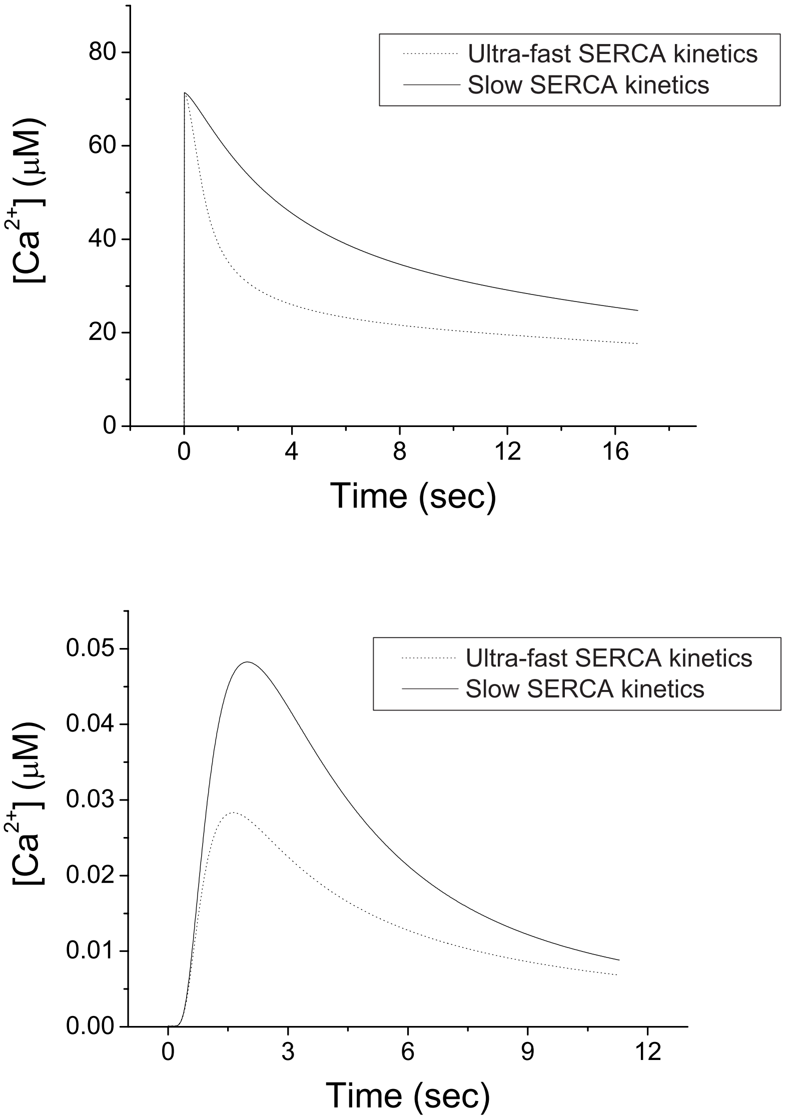

Figure III.5: A: The [Ca^{2+}] released by a puff decreases with time as SERCA works. When SERCA kinetics is slow, less [Ca^{2+}] are pumped back into ER. B: The change of cytosolic calcium level at a puff site after a puff happens at a neighboring site. The peak [Ca^{2+}] is larger when SERCA kinetics is slow.

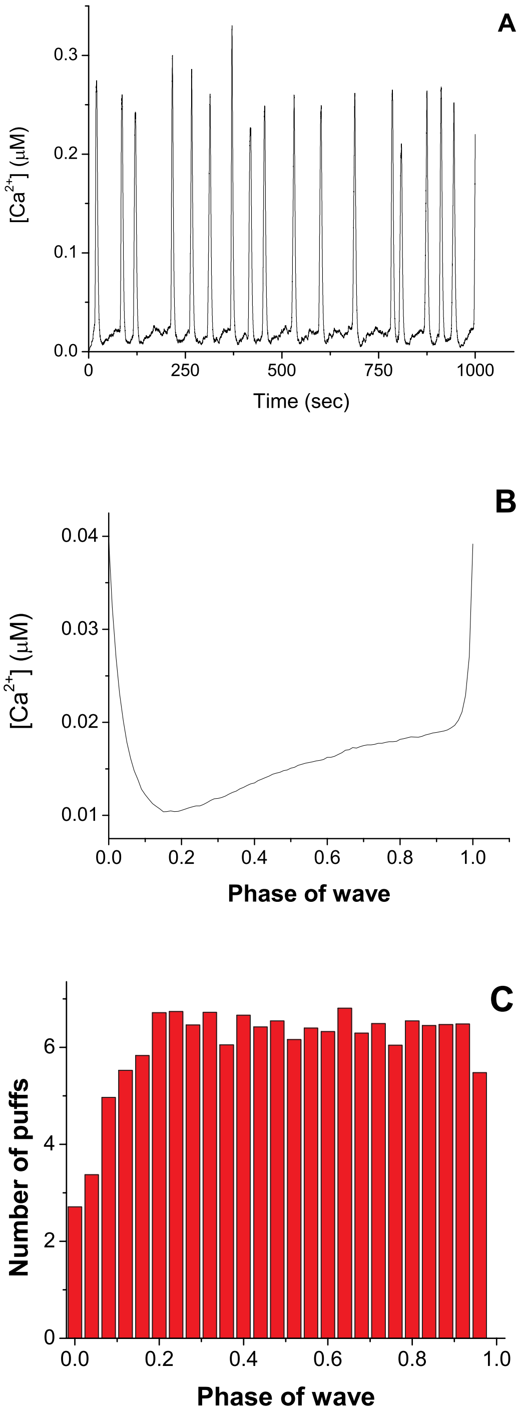

Figure III.6: Cytosolic calcium concentration exhibits periodical global oscillation in the case of slow SERCA kinetics with $[\mathrm{Ca}^{2+}]_{th} = 0.12\mu M$. A: a trace of $[\mathrm{Ca}^{2+}]$ for the first 1000 s. B: cytosolic calcium level averaged over 172 interwave intervals as a function of a rescaled wave phase beginning immediately following a global wave. C: corresponding averaged puff frequency as a function of wave phase.

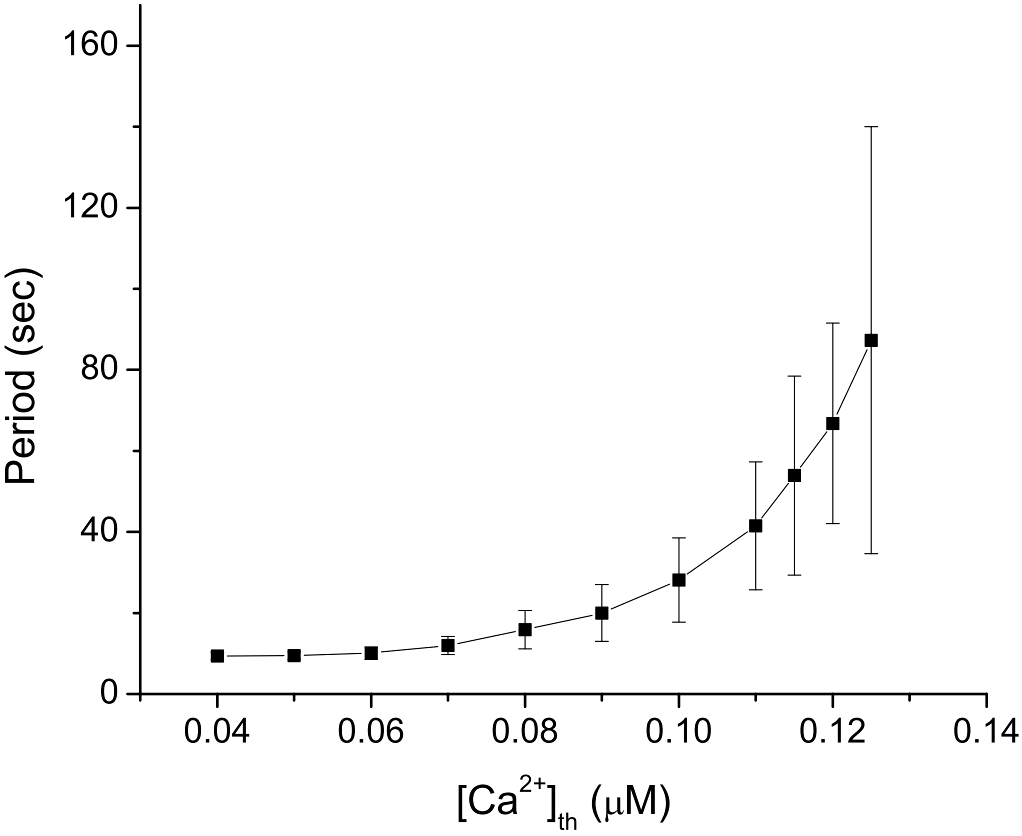

Figure III.7: The mean and standard deviation of inter-wave intervals as a function of $[\mathrm{Ca}^{2+}]_{th}$ for the model with slow SERCA kinetics.

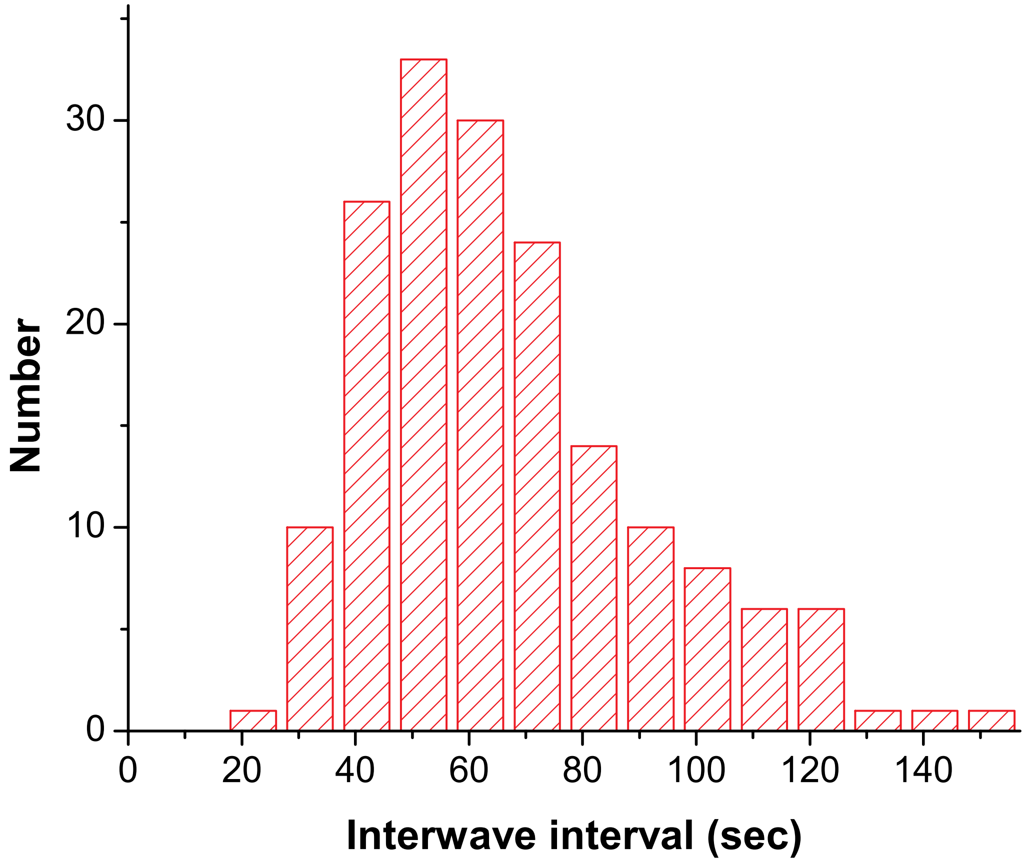

Figure III.8: The distribution of inter-wave intervals for the slow SERCA kinetics case and $[\mathrm{Ca}^{2+}]_{th} = 0.12\mu M$. The mean inter-wave interval for this distribution is 66.8s while the standard deviation is 24.7s.

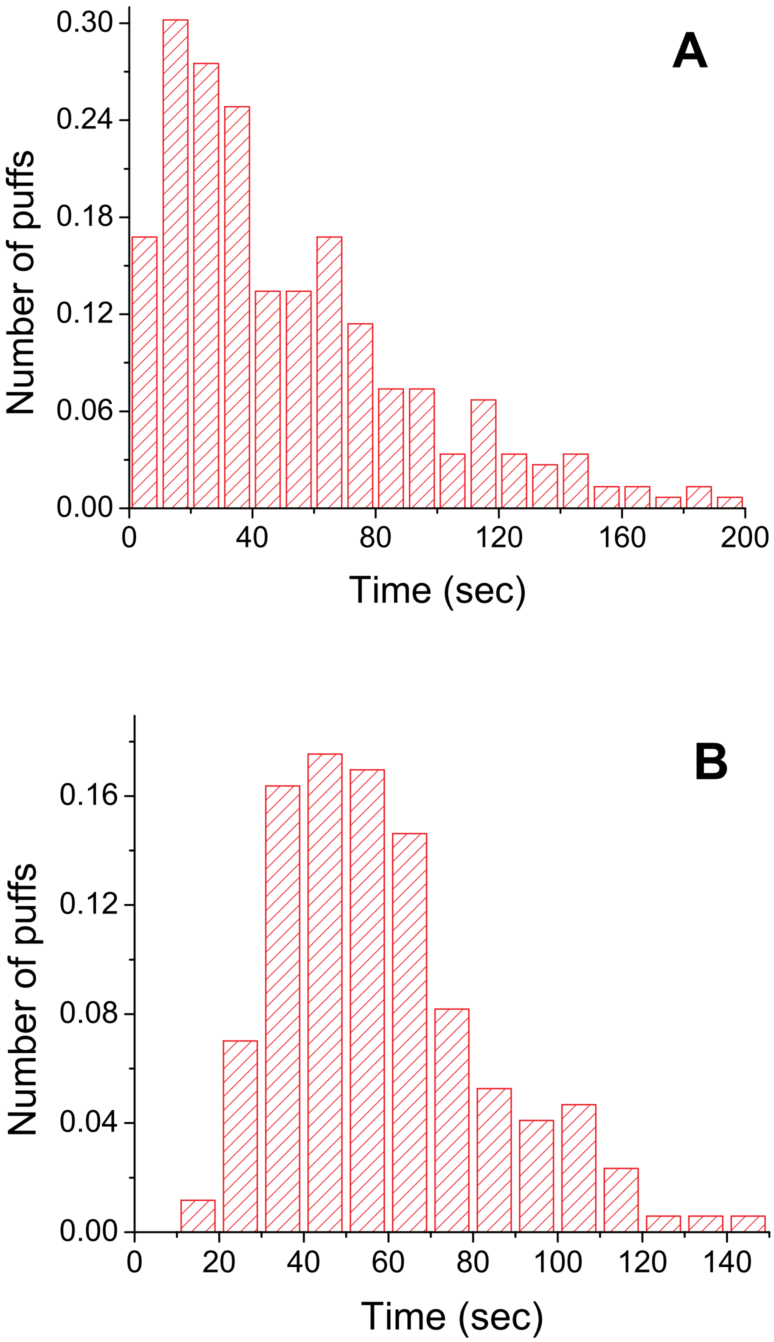

Figure III.9: The distribution of triggered puffs for ultra-fast SERCA kinetics with $[\mathrm{Ca}^{2+}]_{th} = 0.1\ \mu M$ (A) and slow SERCA kinetics with $[\mathrm{Ca}^{2+}]_{th} = 0.12\ \mu M$ (B). In A, the distribution was obtained by examining 149 global waves, containing 251 puffs, while in B, the distribution was found by simulating 172 global waves with 172 puffs.

Bibliography

[1] Berridge, M. J., Bootman, M. D. & Roderick, H. L. (2003) Calcium signalling: dynamics, homeostasis and remodelling. *Nat. Rev. Mol. Cell Biol.* **4,** 517-529.

[2] Sun, X. P., Callamaras, N., Marchant, J. S. & Parker, I. (1998) A continuum of InsP3-mediated elementary Ca2+ signalling events in Xenopus oocytes. *J. Physiol.* **509,** 67-80

[3] Mak, D., McBride, V., Raghuram, Y., Joseph, S. & Foskett, J. (2000) Single-channel properties in endoplasmic reticulum membrane of recombinant type 3 inositol trisphosphate receptor. *J. Gen. Physiol.* **115,** 241-255

[4] Marchant, J. S. & Parker, I. (2001) Role of elementary Ca(2+) puffs in generating repetitive Ca(2+) oscillations. *EMBO J.* **20,** 65-76

[5] Bootman, M. D., Lipp., P. & Berridge, M. J. (2001) The organisation and functions of local Ca(2+) signals. *J. Cell Sci.* **114,** 2213-2222

[6] Bootman, M. D., Berridge, M. J. & Lipp P. (1997) Cooking with calcium: the recipes for composing global signals from elementary events. *Cell* **91,** 367-73.

[7] Shuai, J. W. & Jung, P. (2003) Optimal ion channel clustering for intracellular calcium signaling. *Proc. Natl. Acad. Sci.* USA **100,** 506-510

[8] Falcke, M. (2003) On the role of stochastic channel behavior in intracellular Ca2+ dynamics. *Biophys. J.* **84,** 42-56

[9] Falcke, M. (2003) Buffers and oscillations in intracellular Ca2+ dynamics. *Biophys. J.* **84,** 28-41

[10] Schuster, S. Marhl, M. & Höfer, T. (2002) Modelling of simple and complex calcium oscillations: from single-cell responses to intercellular signalling. *Eur. J. Biochem.* **269,** 1333-1355

[11] DeYoung, G. W. & Keizer, J. (1992) A single-pool inositol 1,4,5-trisphosphate-receptor-based model for agonist-stimulated oscillations in Ca2+ concentration. *Proc. Natl. Acad. Sci.* USA **89,** 9895-9899

[12] Li, Y. & Rinzel, J. (1994) Equations for InsP3 receptor-mediated [Ca2+]i oscillations derived from a detailed kinetic model: a Hodgkin-Huxley like formalism. *J. Theor. Biol.* **166,** 461-473

[13] Swillens, S., Dupont, G., Combettes, L. & Champeil, P. (1999) From calcium blips to calcium puffs: theoretical analysis of the requirements for interchannel communication. *Proc. Natl. Acad. Sci.* USA **96,** 13750-13755

[14] Coombes, S. & Timofeeva, Y. (2003) Sparks and waves in a stochastic fire-diffuse-fire model of Ca2+ release. *Phys. Rev. E* **68,** 021915

[15] Camello, P., Gardner, J., Petersen, O. H. & Tepikin, A. V. (1996) Calcium dependence of calcium extrusion and calcium uptake in mouse pancreatic acinar cells. *J. Physiol.* **490.3,** 585-593

[16] Lytton, J., Westlin, M., Burk, S. E., Shull, G. E. & MacLennan, D. H. (1992) Functional comparisons between isoforms of the sarcoplasmic or endoplasmic reticulum family of calcium pumps. *J. Biol. Chem.* **267,** 14483-14489

[17] Ji, Y., Loukianov, E., & Periasamy, M. (1999) Analysis of sarcoplasmic reticulum Ca2+ transport and Ca2+ ATPase enzymatic properties using mouse cardiac tissue homogenates. *Anal. Biochem.* **269**(2), 236-244

[18] Shuai, J. W. & Jung, P. (2002) Stochastic properties of Ca(2+) release of inositol 1,4,5-trisphosphate receptor clusters. *Biophys. J.* **83,** 87-97

[19] Albritton, N. L., Meyer, T. & Streyer, L. (1992) Heterotrophic plate counts of surface water samples by using impedance methods. *Science* **258,** 1812-1815

[20] Marchant, J., Callamaras, N. & Parker, I. (1999) Initiation of IP(3)-mediated Ca(2+) waves in Xenopus oocytes. *EMBO J.* **18,** 5285-5299

[21] John L. M., Lechleiter J. D. & Camacho P. (1998) Differential modulation of SERCA2 isoforms by calreticulin. *J. Cell Biol.* **142,** 963-973

[22] Inesi, G., Kurzmack, M. & Lewis, D. (1988) Kinetic and equilibrium characterization of an energy-transducing enzyme and its partial reactions. *Methods Enzymol.* **157,** 154-190

[23] Sumbilla, C., Lewis, D., Hammerschmidt, T. & Inesi, G. (2002) The slippage of the Ca2+ pump and its control by anions and curcumin in skeletal and cardiac sarcoplasmic reticulum. *J. Biol. Chem.* **277,** 13900-13906

[24] Dode, L., Vilsen, B., Baelen, K.V., Wuytack, F., Clausen, D. & Andersen, J.P. (2002) Dissection of the functional differences between sarco(endo)plasmic reticulum Ca2+-ATPase (SERCA) 1 and 3 isoforms by steady-state and transient kinetic analyses. *J. Biol. Chem.* **227**(47), 45579-45591

[25] Verboomen, H., Wuytack, F., Van Den Bosch, L., Mertens, L. & Casteels, R. (1994) The functional importance of the extreme C-terminal tail in the gene 2 organellar Ca(2+)-transport ATPase (SERCA2a/b). *Biochem. J.***302,** 979-984

[26] Dode, L., Andersen, J.P., Leslie, N., Dhitavat, J., Vilsen, B. & Hovnanian, A. (2003) Dissection of the functional differences between sarco(endo)plasmic reticulum Ca2+-ATPase (SERCA) 1 and 2 isoforms and characterization of Darier disease (SERCA2) mutants by steady-state and transient kinetic analyses. *J. Biol. Chem.* Ahead of Print

[27] Woods, N.M., Cuthbertson, K.S.R. & Cobbold, P.H. (1986) Repetitive transient rises in cytoplasmic free calcium in hormone-stimulated hepatocytes. *Nature* **319**, 600-602

IV

Excitation-contraction Coupling Gain and Cooperative Gating of Cardiac RyR

Congestive heart failure (HF) is a condition affecting more than two million people in the USA, characterized by reduced contractility of the heart muscle [1, 2, 3]. Many of these patients will die directly from this contractile dysfunction, associated with a reduction of calcium transients elicited in response to electrical stimulation; others will die from ventricular arrhythmias many of which themselves appear related to this calcium handling malfunction [4]. The calcium transient reduction in turn appears to be primarily due to a decrease in the amount of releasable Ca^{2+} in the SR [5]. Many factors can contribute to this reduction, including lowered SERCA pump activity, smaller influx through the L-type channel, anomalous activity of the Na-Ca exchanger and, of concern here, increased SR leak through the RyR array. The relative importance of these components continues to be debated [3, 6, 7].

In this study, we focus on the role of RyR subunit cooperativity as it affects RyR gating and hence diastolic SR leak. Initial evidence for this cooperativity came from lipid bilayer experiments in which the concentration of FK506-binding protein (FKBP) was controlled [8, 9]. The RyR, a homotetramer comprised of four monomers that can each bind one FKBP, was found to exhibit subconductance states in the absence of FKBP. These subconductance states are characterized by fractional openings of the receptor and the current through these fractional openings were, interestingly, either 1/4, 1/2 or 3/4 of the current of a fully opened channel. The clear implication of this *in vitro* data was that FKBP binding induced a coupling between the otherwise independent opening and closing dynamics of the individual subunits.

Data from isolated myocyte studies also shows the importance of FKBP in RyR functioning. However, these experiments provide seemingly contradictory results: sequestering of FKBP in rats [10] and mice [11] was found to increase E-C coupling gain while in rabbits it resulted in a decreased E-C coupling gain [12]. In addition, overexpression of FKBP in rabbits was reported to increase the Ca^{2+} transient and contractility [13, 14], while overexpression in rats decreased the spontaneous spark frequency while increasing the Ca^{2+} transient [15].

To model the role of FKBP in RyR gating, we introduce an allosteric interaction between the RyR subunits whose strength is modulated by FKBP binding. This interaction changes the transition rates in a Markov process approach to RyR gating. We find that the E-C coupling gain exhibits a clear maximum for a certain optimal level of cooperativity (i.e. an optimal value of FKBP binding). In addition, we find that an increase in cooperativity leads to a decrease in the spontaneous spark frequency. These results are then critically compared to existing experimental data. Furthermore, our model can be compared to detailed information regarding the effects of adrenergic stimulation, based on the fact that stimulation leads to activation of cAMP-dependent protein kinase A (PKA) which then lowers FKBP binding via RyR phosphorylation [16, 17].

It is through the action of PKA that HF is hypothesized to lead to increased SR leak. Specifically, a chronic hyperadrenergic state during HF leads to elevated levels of PKA and consequently the RyR becomes hyperphosphorylated

[18, 19]. This leads to a persistent dissociation of FKBP and presumably a reduced SR content [19, 20, 21]. Our results lend support to this proposed mechanism, as we show that a reduction of cooperativity as would be caused by FKBP disassociation would indeed give rise to a large RyR leak and a concomitantly reduced SR content. While one obviously needs to use a more comprehensive model to account for all the changes in calcium handling one would expect under HF conditions, the results to date do show that this idea is quantitatively sensible.

We note in passing a final set of experiments which links FKBP directly to cardiac arrhythmias: FKBP deficient mice were found to consistently exhibit exercise-induced ventricular arrhythmias and sudden cardiac death [22], most likely caused by delayed after depolarization resulting from Ca^{2+} mishandling. Moreover, it was shown that restoring the binding of FKBP through pharmaceutical intervention was able to protect these mice from ventricular arrhythmias [23] Although it remains extremely challenging to relate subcellular-scale physiology with organism scale response, we view this latest work as an indication that properly modeling the effects of FKBP is a critical issue that is timely to address.

IV.A Materials and Methods

IV.A.1 Intracellular Calcium Dynamics

The calcium dynamics in the myocyte is locally controlled through the tight coupling between the L-type calcium channels and the RyR cluster. In our model, the calcium concentration in the dyadic space, $[Ca^{2+}]_{ds}$, is described as:

$$\frac{d[Ca^{2+}]_{ds}}{dt} = J_{RyR} + J_{dhpr} + J_{buf} - \frac{[Ca^{2+}]_{ds} - [Ca^{2+}]_{cyto}}{\tau_{efflux}} \tag{IV.1}$$

Here, J_{buf} describes the binding of calcium to buffers that are present in the dyadic space [24]:

$$J_{Buf} = -\sum_j k_{j,on}[Ca^{2+}]_{ds}([B_j] - [CaB_j]) - k_{j,off}[CaB_j] \tag{IV.2}$$

The sum is over 3 calcium buffers B (calmodulin, SR membrane buffers and sarcolemmal membrane buffers) of constant concentration. For a full description including parameter settings we refer to the Supplemental Materials. Furthermore, J_{RyR} is the flux through the RyRs, J_{dhpr} is the L-type channel flux and the last term represents the flow of Ca^{2+} ions from the dyadic space to the cytoplasm.

The equation for the Ca^{2+} concentration in the junctional SR (jSR), $[Ca^{2+}]_{jSR}$, includes the release of Ca^{2+} through the RyR receptors and the refilling from the network SR (nSR), where the Ca^{2+} concentration, $[Ca^{2+}]_{nSR}$, is taken as constant:

$$\frac{d[Ca^{2+}]_{jSR}}{dt} = \beta_{jSR}\left(-\frac{V_{ds}}{V_{jSR}}J_{RyR} + \frac{[Ca^{2+}]_{nSR} - [Ca^{2+}]_{jSR}}{\tau_{refill}}\right) \tag{IV.3}$$

where the parameter values are listed in Table IV.1. In this equation, we have assumed rapid equilibrium between calcium and calsequestrin in the junctional SR, leading to [25]:

$$\beta_{jSR} = \left(1 + \frac{[B_{CSQN}]K_{CSQN}}{(K_{CSQN} + [Ca^{2+}]_{ds})^2}\right)^{-1} \tag{IV.4}$$

In most of the simulation results reported here we assumed that $[Ca^{2+}]_{cyto}$ was constant and equal to its resting cytosolic calcium concentration $[Ca^{2+}]_i$. Furthermore, the the nSR calcium concentration $[Ca^{2+}]_{nSR}$ was also taken constant. These assumptions lead to a more computationally tractable model that avoids the simulation of the cytosolic calcium machinery including SERCA pumps and the sodium-calcium exchanger. Furthermore, since $[Ca^{2+}]_{nSR}$ is assumed to be constant, it is sufficient to simulate a single calcium release unit (see E). However, we have also performed simulations using a “full model” in which these assumptions are relaxed. Details of this model can be found in the Supplemental Materials sections. The results of these simulations (shown in Fig. IV.4) demonstrate that the full model produces qualitatively identical results to the simple model.

Table IV.1: Cell Geometry Parameters

Parameter	Description	Value	Reference
A_{cap}	Cell capacitance	153.4pF	[26]
V_{cyto}	Cytoplasm volume	25.84pL	[26]
V_{jSR}	Junctional SR volume	0.16pL	[26]
V_{nSR}	Network SR volume	2.1pL	[26]
V_{ds}	Dyadic space volume	1.2×10^{-3}pL	[26]
$[Ca^{2+}]_o$	Extracellular calcium concentration	2.0mM	[26]
$[Ca^{2+}]_i$	Cytosolic calcium concentration	0.1μM	[24]
$[Ca^{2+}]_{nSR}$	Network SR calcium concentration	1.0mM	[24]
τ_{efflux}	Dyadic space efflux time	7.0×10^{-7}s	[24]
τ_{refill}	Junctional SR refilling time	0.003s	[25]

IV.A.2 The L-type calcium channel

To model the L-type channel, we adopt the formulation from [26], along with its parameters. The channel is described via a Markov model consisting of 11 voltage and calcium-dependent states along with 2 voltage dependent inactivation states. The calcium current through a single channel can be written as:

$$I_{dhpr} = P_{Ca}\frac{4VF^2}{RT}\frac{[Ca^{2+}]_{ds}e^{2VF/RT} - 0.341[Ca^{2+}]_o}{e^{2VF/RT} - 1} \tag{IV.5}$$

leading to a total flux through the L-type channel

$$J_{dhpr} = -\frac{N_{open,dhpr}I_{dhpr}}{2FV_{ds}} \tag{IV.6}$$

where V is the membrane potential, P_{Ca} is the channel permeability, $[Ca^{2+}]_o$ is the extracellular calcium concentration and where $N_{open,dhpr}$ is the number of open L-type calcium channels, which is set to be 10 per calcium release unit in our simulation. For further details we refer to [25, 26].

IV.A.3 The RyR

As already noted, the RyR is a homotetramer comprised of four monomers that can each bind one FKBP. Lipid bilayer experiments have shown that RyR can exhibit 1/4, 1/2 and 3/4 of the total channel conductance when FKBP is absent (8). In our model we thus assume that each subunit can be activated upon binding of one Ca^{2+} ion and is responsible for 1/4 of the maximum current via a conformational change. To model the gating kinetics of the subunits, we will employ a simple scheme in which each subunit can be in one of three states: closed (C), open (O) or inactivated (I) (see Fig. IV.1). Similar gating schemes, but without subunit coupling, were investigated in [27]. To incorporate the FKBP binding effect, we assume that it can introduce an allosteric energy between neighboring subunits and that subunits are energetically penalized for being in a different state than their neighbors. This allosteric energy is introduced via a symmetric energy matrix with vanishing diagonal terms:

$$\mathbf{\Delta E} = \mathbf{s} \times \begin{pmatrix} 0 & \Delta E_{co} & \Delta E_{ci} \\ \Delta E_{co} & 0 & \Delta E_{oi} \\ \Delta E_{ci} & \Delta E_{oi} & 0 \end{pmatrix} \tag{IV.7}$$

The continuous variable s is the key parameter in our model and controls the coupling strength between subunits. It corresponds indirectly to the amount of associated FKBP with low values of s corresponding to nearly all FKBP being dissociated and high values of s corresponding to full FKBP association.

To include this interaction into the RyR gating dynamics, we need to specify how this interaction energy enters into the rate constants. Here, we simply follow [27] and let half of the energy contribute to the forward rate constant and half to the backward rate constant. In other words, the rate constants K_{ij} for the transition from state i to state j have the form:

$$K_{ij} = k_{ij} \exp\left(\sum \frac{s\,(\Delta E_{is_m} - \Delta E_{js_m})}{2kT} \right) \tag{IV.8}$$

where the sum is over neighboring subunits and s_m is the state of the neighboring subunits. The values of matrix elements ΔE_{ij} and the transition rates k_{ij} in the absence of any allosteric interaction used in our simulations are given in Table IV.2.

Based on experimental results, we take the number of RyRs in our basic calcium release unit to be 100 [28]. Fast equilibrium of calcium diffusion within the dyadic space is assumed so that all the RyRs in the same calcium release unit sense $[\mathrm{Ca}^{2+}]_{ds}$ with no difference. The total flux through the RyRs in a calcium release unit is then proportional to the concentration gradient and the number of open subunits $N_{open,RyR}$:

$$J_{RyR} = g_{RyR} N_{open,RyR}([Ca^{2+}]_{jSR} - [Ca^{2+}]_{ds}) \tag{IV.9}$$

where g_{RyR} is the conductance of single RyR subunit. See Table IV.2 for parameter settings.

IV.A.4 The E-C coupling gain

The E-C coupling gain function is defined as:

$$Gain = \frac{J_{RyR,max} - J_{RyR,rest}}{J_{dhpr,max}} \tag{IV.10}$$

where $J_{RyR,max}$ and $J_{dhpr,max}$ are the maximal fluxes through the RyR cluster and the L-type calcium channels during E-C coupling, and $J_{RyR,rest}$ is the calcium release through the RyR receptors in the absence of J_{dhpr}.

IV.A.5 Simulation protocol

The gating of L-type calcium channels and RyRs are simulated as Markov processes. Thus, at each time step, a random number is generated to help a channel to decide how its state should change based on the rate equations. The time step Δt is set to be 10^{-5}s, which is much shorter than all the processes except the calcium efflux from dyadic space to the cytoplasm. During Δt, Eq. IV.11 is integrated analytically under the approximation that J_{dhpr}, J_{RyR} and J_{Buf} don't

Table IV.2: RyR parameters

Parameter	Description	Value
N_{RyR}	Number of RyRs in a CaRU	100
g_{RyR}	conductance of single RyR subunit	800/s
k_{co}	transition rate from C to O	31.25μM/s
k_{oc}	Rate constant from O to C	1250.0/s
k_{oi}	Rate constant from O to I	5.0/s
k_{io}	Rate constant from I to O	5.0/s
k_{ic}	Rate constant from I to C	2.0/s
k_{ci}	Rate constant from C to I	0.05μM/s
ΔE_{co}	interaction energy between C and O	5.0kT
ΔE_{oi}	interaction energy between O and I	1.667kT
ΔE_{ci}	interaction energy between C and I	0
s	strength of coupling between subunits	adjustable

change during such a short time interval. Eq. IV.12 is simply integrated using Euler's method.

All simulations reported here consisted of presenting a sequence of triggers to the calcium release units. The trigger, given once every second, consisted of clamping the membrane voltage from a holding voltage of -80 mV to a specified higher potential (0 mV everywhere, except in Fig. IV.2 where it is varied) for a duration of 0.1 s. Since each calcium release unit exhibits a response which varies stochastically from trigger to trigger, this sequence needs to be long enough to ensure statistically meaningful results that can be compared to the *spatially* averaged results in myocyte experiments. In all simulations recorded here, we used a sequence of 1000 triggers, with the first 50 discarded to eliminate transient effects.

In our simple model, in which the nSR calcium concentration is kept constant, it is sufficient to simulate a single release unit. In the full model, on the other hand, we simulated 100 calcium release units simultaneously. Each release unit share a common cytoplasm and nSR, in which the calcium concentration is treated as a dynamic variable. Further details are furnished in the Supplemental Materials.

IV.B Results

We start by showing in Fig. IV.2 the gain as a function of the membrane potential for a particular value of s. For different values of s we obtained qualitatively similar curves (data not shown). The gain is clearly a monotonically decreasing function of the membrane potential and displays the graded release found in experiments [29,30,31]. The current through a single L-type channel and through a RyR, on the other hand, is bell shaped, with a small difference between their positions. This type of graded release is indicative of the local control theory. After all, if the RyR would respond only to the ensemble-averaged L-type current it would be impossible to have a different gain for two identical values of I_{dhpr}. Instead, the RyR responds to and is triggered by local L-type channels.

We next show in Fig. IV.3 the Ca^{2+} concentration in the dyadic space as a function of time for different values of s. As s is increased, the decay rate becomes larger and the peak Ca^{2+} concentration increases. After $s \sim 0.4$, however, both the decay time and the rising rate increase and this peak Ca^{2+} concentration decreases. This leads to a maximum in peak Ca^{2+} concentration for a particular value of the cooperativity parameter $s^* \sim 0.4$.

The gain function also shows a clear maximum as a function of the cooperativity s (Fig. IV.4A) with the maximum occurring at $s = s^*$. Here, as in Fig. IV.4B and C, we have plotted the results from the simple model as a thick solid line and the results from the full model as a thin dashed line. Further characterization of the effect of a varying s is illustrated in Fig. IV.4B where we plot the diastolic jSR content as function of s. The diastolic jSR content was measured during the second half of the 1 s interval separating the stimuli. This content increases monotonically until $s \sim s^*$, and then reaches the nSR concentration in the simple model. In the full model, on the other hand, the jSR content depends on the uptake mechanisms and reaches an equilibrium for larger values of s. The resting value of the Ca^{2+} concentration in the dyadic space as a function of s is plotted in Fig. IV.4C. It is a monotonically decreasing function of s for $s < s^*$ and is roughly constant for $s > s^*$.

Comparing the results from the two models shows that the simple model already captures the essential qualitative features of the full model. It also shows a distinct bell shaped gain curve while the jSR content saturates at slightly earlier values of s. Note that the Ca^{2+} concentration in the dyadic space in the full model increases slower when s is decreased due to the partial depletion of the jSR and the nSR. Finally, the nSR calcium concentration in the full model follows the jSR calcium concentration for $s > s^*$ and decreases to values slightly higher than the jSR calcium concentration for $s > s^*$ (data not shown). In the remainder of the chapter, we will focus on the simple model.

The reduced SR content for $s < s^*$ is caused by an increased leak in the RyR. This is shown in Fig. IV.5A, where we have plotted the open probability P_0 as a function of background Ca^{2+} for two different values of s. This probability is calculated analytically and represents the probability that at least one subunit is open. Reducing the cooperativity leads to a shift in this curve to smaller values of Ca^{2+} and thus to an increased probability for opening at low Ca^{2+} concentration. The presence of an increased leak is further illustrated in Fig. IV.5B and C where we plot the distribution of open states within an RyR at a controlled calcium concentration (the dashed line in Fig. IV.5A). For $s = 0$ (Fig. IV.5B), the subunits are completely independent and the distribution shows a significant contribution from the subconductance states. For high values of s (Fig. IV.5C), the increased cooperativity suppresses the subconductance states and the fully closed and fully open states become dominant.

The effect of the subunit cooperativity and the presence of a leak can be further characterized by the spontaneous spark frequency. To measure this frequency, we stimulated the cell every second and measured the number of sparks 0.5 s before each stimulus. The total duration of the numerical experiment was 50 s and to ensure the steady state was reached we discarded the first 40 s. We defined a spontaneous calcium spark as an event during which 30% or more of the subunits open. Furthermore, to prevent counting small fluctuations around this threshold value, we required the activity to decrease below 5% of the subunits before a new spark could be counted. The measured spark frequency (per calcium release unit) is shown in Fig. IV.6 and shows that this frequency decreases rapidly when s approaches s^*. For $s > s^*$ the measured spontaneous spark frequency was essentially zero, indicating that an increased cooperativity reduces the probability for a spontaneous spark and hence for leak. Furthermore, assuming a distance of 2 μm between CRUs along a Z-line, for s slightly smaller than s^* we obtain spark rates (0.1-0.5 /s/CRU) that are in good agreement with experimentally obtained values (0.1 /s/CRU) [14].

We have also examined the detailed calcium release pattern in the presence of the L-type channel current and found it was different for $s < s^*$ and $s > s^*$. In Fig. IV.7A we plot the distribution of latency times, defined as the time between the rising of the test potential and the time when J_{RyR} reaches its maximum. As s is increased, the average and the variation of the latency times are: 7.9 ms and 8.2 ms respectively for $s = 0.3$, 7.6 ms and 4.9 ms respectively for $s = 0.4$ and 13.3 ms and 8.5 ms respectively for $s = 0.5$. The mean latency time increases significantly when $s > s^*$, and the variation reaches minimum at $s = s^*$. Furthermore, we have calculated the total fraction of open RyR channel subunits within a cluster at the peak Ca^{2+} concentration, and have plotted its distribution in Fig. IV.7B. As s is increased, this distribution changes from essentially single-peaked to clearly double peaked. In other words, for higher values of s, the probability of opening becomes smaller and a substantial portion of clusters exhibit a small fraction of open RyRs. This, combined with the larger variation in latency time, indicates that the calcium release from different clusters is less synchronized by the triggers when the cooperativity becomes larger than s^*.

To examine the dependence of the gain on the SR load, we also performed simulations using a higher nSR Ca^{2+} concentration and recalculated the gain as a function of s. The result, for two different values of $[Ca^{2+}]_{nSR}$, is plotted in Fig. IV.8 and shows that the qualitative form of the gain curve has not changed. On the other hand, the peak value of the gain shifts towards lower values of s for increased SR content. Thus, for a given value of s, the gain function can be either increasing or decreasing, depending on the value of the SR load.

IV.C Discussion

In this chapter we have examined the effect of cooperativity between RyR subunits using a theoretical approach. This approach consists of modeling the Ca^{2+} dynamics within the cell and the dyadic cleft combined with a novel Markovian approach for the RyR. The RyR Markovian model takes into account the subunit structure of the RyR and includes a measure of cooperativity s. Using this model, we calculated the E-C coupling gain as a function of several system parameters. Our main result is that this gain exhibits a clear maximum for a particular value of the cooperativity, $s = s^*$. For larger cooperativity values the resting jSR content is s insensitive while for smaller values it decreases with decreasing s.

To understand intuitively why the gain curve displays a maximum let us consider the effects of the subunit cooperativity s on the gain. This gain is roughly determined by the maximum value of J_{RyR} and is thus given by the product of the open probability of the RyRs and the gradient of the calcium concentration between the jSR and the dyadic space (see Eq. IV.9). Increasing s decreases the open probability, but it increases the calcium concentration difference between the jSR and the dyadic space due to the suppression of subconductance states of the RyR. The competition of these two opposite effects leads to a maximum of gain at some definite s^*.

Specifically, for $s > s^*$, recalling that increasing s represents an energy penalty for a subunit to be in a different state than its neighbors, it is easy to see that a large s makes it more difficult to have fractional openings. In other words, the RyR subunits become more likely to open and close collectively and leads to a smaller effective activation rate due to a higher energy barrier between closed and open states. This can be seen from Fig.IV.7A which shows that the latency time increases as s is increased. Thus, the probability that a cluster can be triggered to open successfully is reduced, which leads to a reduced gain.

For $s < s^*$, the probability that the RyRs exhibit subconductance states becomes substantial (Fig. IV.5). This leads to a persistent SR leak during diastole, defined here as 1/2 s before a stimulus. This causes a decreased SR content (Fig. IV.4B) and an increased diastolic calcium level in the dyadic space (Fig. IV.4C). Hence, upon an I_{dhpr} stimulus, the Ca^{2+} current through the RyRs is smaller, leading to a decreased E-C coupling gain.

How do these results relate to experimental findings? As discussed above, our cooperativity parameter s correlates with the amount of FKBP associated with the RyR complexes in the cell. The effect of FKBP on *in vivo* E-C coupling has been investigated in three species: rat, mouse and rabbit. For the latter, FKBP sequestering reduced E-C coupling [12] while FKBP overexpression increased E-C coupling [13,14]. In rats and mice, on the other hand, FKBP sequestering increased E-C coupling [10,11,12], even though overexpression appears to increase E-C coupling [15]. These results appear to be contradictory, although there are of course caveats about whether other components of the calcium-handling system are affected by the different protocols. If we for the moment ignore the data from FKBP overexpression in rats, we can combine all the other experimental data with the results of our theoretical modeling and provide the following hypothesis: normal levels of cooperativity in rats and mice are higher than the optimal level while normal levels of cooperativity in rabbits are lower than the optimal level. One way to achieve this difference is schematically drawn in Fig. IV.9a where the circle represents the postulated operating point for rats and mice and the square represents rabbits. Another possibility is of course that the subunit cooperativity across species is preserved while other factors determining the gain varies. Then, as is schematically shown in Fig. IV.9b, the rabbit gain curve has shifted in its entirety towards higher values of s compared to the gain curve for the rat and mouse (or vice versa) while the value of the cooperativity s_{op} is the same for both species. In both cases, the operating value of s for the rat and mouse is larger than s^* which agrees with experimental data showing that the SR content is maintained during FKBP dissociation [12]. The fact that the SR content decreases in rabbits after dissociation of FKBP and increases after FKBP overexpression [12,13] serves as a self-consistency check (see Fig. IV.4).

On the other hand, if the overexpression of FKBP in rats does indeed increase the E-C coupling gain [15], we have to modify the above hypothesis. In this case, the experimental data is consistent with our modeling results if we assume that both rats/mice and rabbits have a normal level of cooperativity that is lower than the optimal level. Of course, this still leaves open the question why FK506 decreases the gain in rats but perhaps, as pointed out in [15], it also acts on other components of the E-C coupling machinery. In summary, it is clear that rabbits lie to the left of the peak and the situation for rats/mice needs to be clarified experimentally.

Another comparison comes from the distribution of the spark latency times. Two groups [32,33] performed experiments showing that the calcium release is more synchronized under β-AR stimulation. Although Song et al hypothesized that the observed simultaneous release of calcium is mainly an effect of increased L-type channel current, we show in Fig. IV.7 that a decreased cooperativity inside

RyR can also cause a larger probability for a cluster to respond to the trigger. Moreover, our model predicts that the mean latency time increases as s increases, which is consistent with experiments [32].

A final comparison with in vivo experiments can be made when we analyze the frequency of spontaneous sparks (Fig. IV.6). Since increasing s corresponds to increasing the energy barrier, we find that the spark frequency decreases as s increases. This is consistent with experimental findings which show a decreased spontaneous spark frequency in rabbits with overexpressed FKBP [14]. In fact, it is also consistent with the observed decrease in spontaneous spark frequency in FKBP-overexpressing rats [15], independent of the aforementioned uncertainty as to the normal level of cooperativity. In addition, the model shows that for $s < s^*$, the total released Ca^{2+} in a cluster is smaller than for $s \sim s^*$ due to a decreased jSR content. Thus, for $s < s^*$ a locally triggered spark is less likely to initiate a release event in the neighboring cluster and a propagating wave is more likely to abort. This scenario seems consistent with experimental data in FKBP -overexpressed rabbits. Of course, to investigate wave propagation in our model requires us to include spatial coupling between cluster and t-tubules. Once incorporated, this model would then be able to investigate the stochastic process of wave abortion, using an similar approach to that employed in [34] for the case of Xenopus oocytes.

Our major goal was to produce a model which could be compared with data from single myocyte studies as well as from bilayer experiments. The bilayer experiments suggest that in the presence of FKBP the subconductance states are nearly completely suppressed, while in the absence of FKBP they are prominently present. By assuming that each RyR subunit can contribute 1/4 of the total conductance independently and that they must act cooperatively with FKBP binding, our model produces very similar distributions of subconductance states (Fig. IV.5) as shown in those experiments.

Our model is not able to investigate the complete ”fight-or-flight” response, during which the $\beta-$adrenergic pathway is stimulated and PKA activation levels are elevated. This signaling pathway not only targets the RyR but also increases the influx through the L-type channel and the Ca^{2+} uptake through the SERCA pumps, mechanisms that are not included in our study. Nevertheless, if our hypothesis shown in Fig. IV.9 is correct, we can postulate that the relative importance of the components involved in the fight-or-flight response should be species dependent. After all, independent of the species, the net result of the fight-or-flight response is an increased E-C coupling gain and cardiac output [35]. If our postulated schematic gain function in Fig. IV.9 is correct, $\beta-$adrenergic stimulation in rabbits will reduce the E-C coupling gain if only considering the dissociation of FKBP from RyR. Thus, one of the other targets of $\beta-$adrenergic pathway needs to compensate the reduction of gain associated with the loss in co-operativity. In mice and rats, if we assume that FK-506 acts primarily on RyRs to decrease the cooperativity and increase the E-C coupling gain, this compensation is not necessary. Of course, if both rabbits and rats operate with normal levels of s below the maximal value, rats also need a compensatory mechanism.

The effect of FKBP dissociation on human congestive heart failure, and in particular the role of PKA hyperphosphorylation, is a controversial topic. Several groups have found that the FKBP association level is significantly decreased by PKA hyperphosphorylation in HF myocytes [19,21]. Furthermore, experiments have shown that drugs can prevent the onset of experimental heart failure by reversing PKA hyperphosphorylation and preventing the decrease of RyR-bound FKBP [21]. Other groups, however, have reported that PKA hyperphosphorylation of RyR does not dissociate FKBP from RyR and can not influence RyR function [36,37,38]. Our model does not take into account the actual mechanism whereby the cooperativity is changed and, hence, can not shed light on the hyperphosphorylation controversy. On the other hand, our model shows that a scenario in which partial association of FKBP (i.e. a slightly lower value of s) results in a increased E-C coupling and severe dissociation of FKBP (i.e. a very low value of s) leads to events typically associated with heart failure (reduced SR content, decreased ECC gain and increased diastolic leak) is plausible.

Marks *et al* found that the destablization of RyR can also lead to exercise induced ventricular arrhythmia, resulting in sudden cardiac death [39]. They compared FKBP12.6 deficient (FKBP12.6$^{-/-}$) mouse myocytes and the normal mouse myocytes, and delayed after-depolarizations (DADs) appear consistently in FKBP12.6$^{-/-}$ mice under exercise. DAD is a spontaneous action potential during diastolic phase and it's a precaution of ventricular arrhythmia. In this case, cytosolic calcium concentration is greatly elevated by the persistent leak through RyR and the overloaded SR Ca^{2+} content. This increases the calcium inward current (majorly sodium calcium exchanger current), and so increases the membrane potential to the threshold of inward fast sodium current, leading to the DAD. This is an interesting phenomenon that we can model in the next step. The voltage clamp condition will be replaced by the interacting dynamics of ion channel currents and membrane potential, and all the major currents including Ca^{2+},Na^{+}, K^{+} and Cl^{-} needs to be simulated carefully. Such a full model has been implemented. However, the simulations show decreasing s greatly prolongs the action potential because RyR can't close and nSR Ca^{2+} is forcibly maintained at high level. But the inward current during diastole, although increased, is not enough to trigger DAD. One possible solution is to add some stronger "fateful" Ca-activation-dependent inactivation mechanism to RyR gating, so calcium sparks can terminate while the frequency of spontaneous sparks is still high for low s. The effect of diffusion may also be very important, because under this pathological condition the background [Ca^{2+}] is high and the opening threshold of RyR is low. A spontaneous spark can probably activate neighboring calcium release units, and the leak is magnified through such a calcium wave. Such a spatially extended model might be necessary to trigger DAD. Overall our work has provided a platform to study the relation between RyR destablization and exercise-linked ventricular arrhythmia. By adding more realistic mechanisms to the current model, it has the potential to simulate the DAD phenomenon observed in experiments.

By now we have only modeled the effect of FKBP on the coupling between the RyR subunits. There is experimental evidence, however, that FKBP can also couple neighboring receptors [40,41]. Several groups have addressed the effect of receptor-receptor coupling on Ca^{2+} dynamics. A recent modeling study, which implements coupling between neighboring RyRs in much the same way as we do here, found that introducing a cooperativity between receptors can make certain unstable RyR gating schemes stable [27]. Another modeling study showed that a lack of cooperativity between receptors can lead to prolonged calcium sparks [24]. In our model, we also observed an increase in the duration of these sparks when we lowered s (data not shown). In fact, we believe that the inter-receptor coupling discussed in [24,27] and the intra-receptor coupling discussed in this chapter may lead to very similar effects. For example, we predict that the gain curve will exhibit a similar qualitative form when varying the inter-receptor coupling constant. The relative importance of intra- vs. inter-receptor coupling remains to be resolved.

Finally, there is no way to date to establish a quantitative link between the concentration of FKBP and the value of s. Microscopically, s can be calibrated to the change of Ca-RyR binding energy for a specific level of bound FKBP. This would require direct measurements of the gating mechanisms while varying the FKBP concentration.

IV.D Acknowledgements

The text of chapter III, in part, is a reprint of the material as it appears in Kai Wang, Yuhai Tu, Wouter-Jan Rappel, and H. Levine, *Excitation-Contraction Coupling Gain and Cooperativity of the Cardiac Ryanodine Receptor: A Modeling Approach*, Biophys. J. **89**, 3017, © 2005 Biophysical Society, where the dissertation author was the first author. The co-authors in this publication directed, supervised, and co-worked on the research which forms the basis of this chapter.

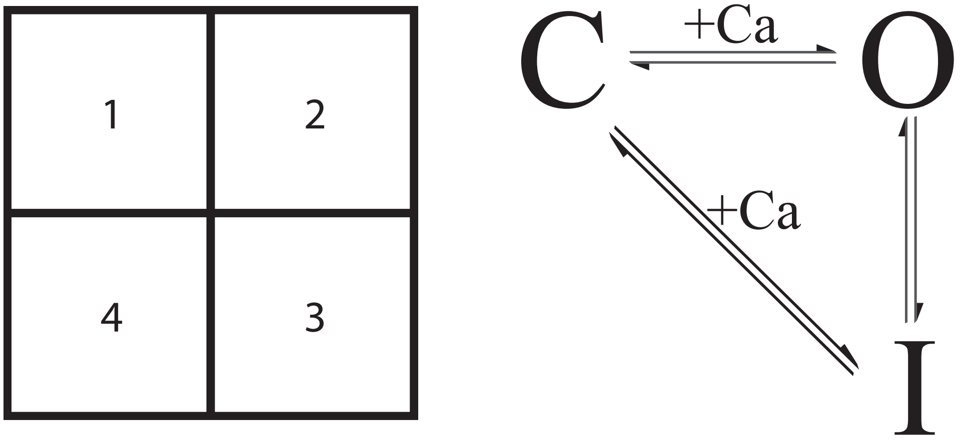

Figure IV.1: Left: A schematic picture of the RyR used in our model. Each receptor consists of four subunits which only interact with its nearest neighbor (i.e., subunit one interacts with subunits 2 and 4 but not with subunit 3). Right: The 3-state model for each RyR subunit.

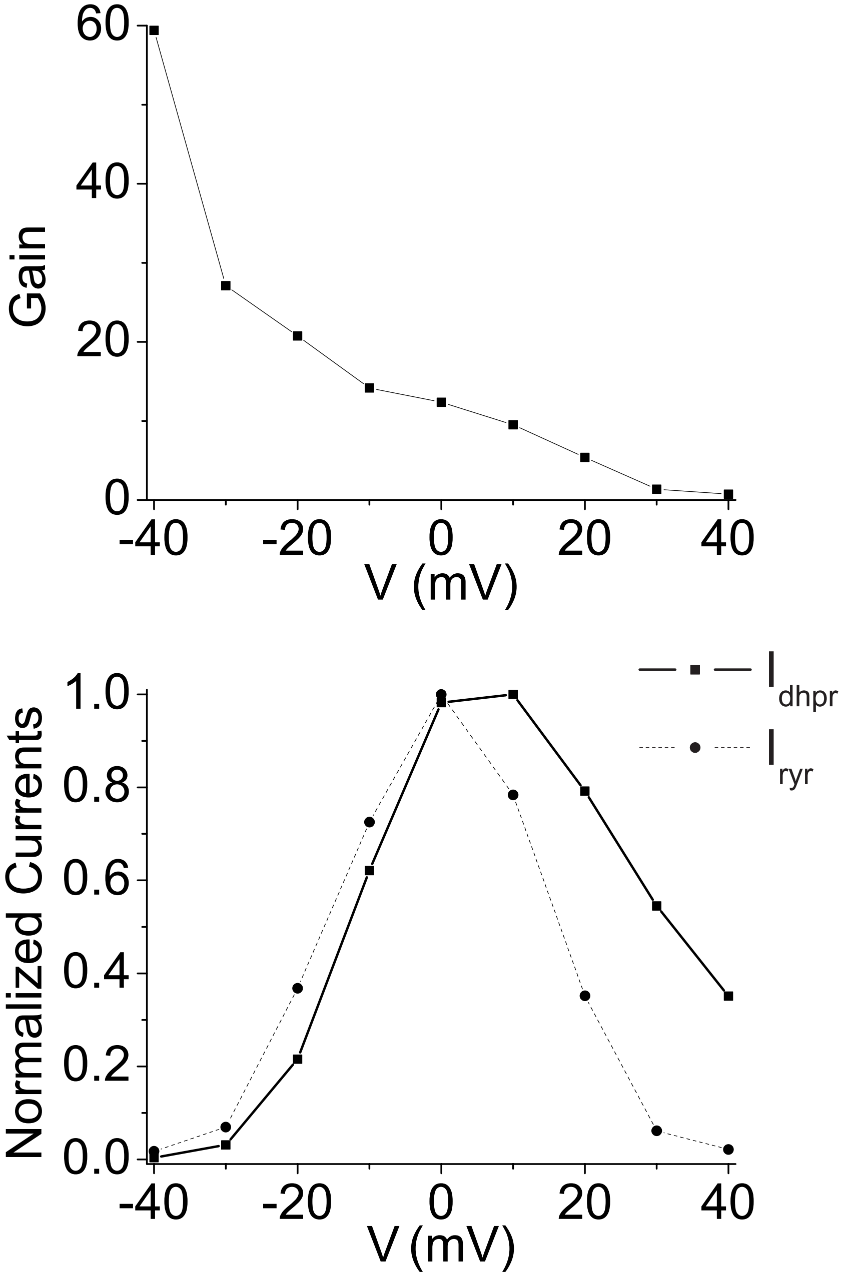

Figure IV.2: Top: The E-C coupling gain as a function of the membrane voltage. Bottom: The current through the L-type channel and the RyR, both normalized to their peak values, as a function of the membrane voltage. s is set to be 0.5 in this simulation.

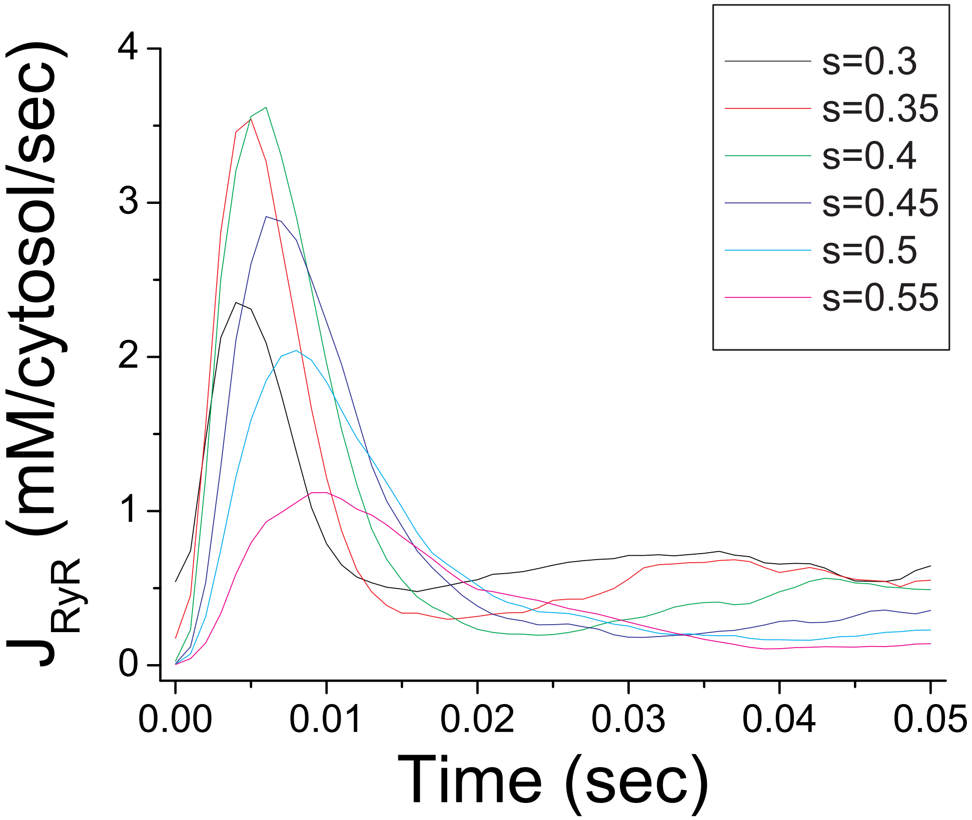

Figure IV.3: Calcium release through the RyR cluster in the dyadic space for different values of s following a 0.1 s pulse of the membrane potential started at t=0 s. The release reaches its maximum at $s = 0.4$.

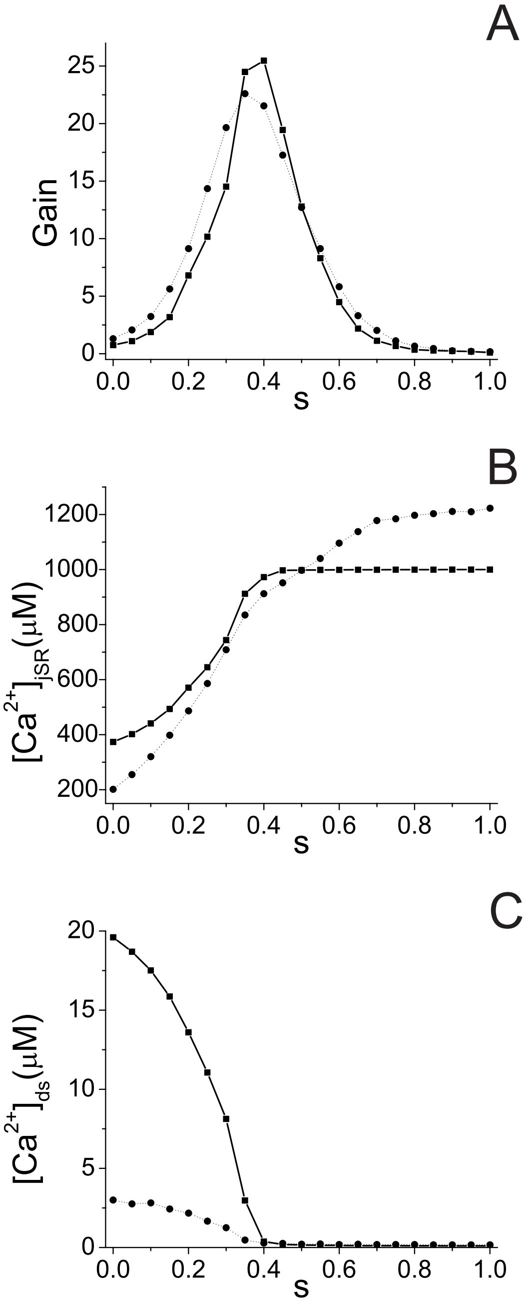

Figure IV.4: Dependence of the gain (**A**), the resting jSR calcium level (**B**) and the diastolic calcium concentration in the dyadic cleft (**C**) on the coupling strength (**s**). The thick lines show results from from the simple model and the thin lines display results from the full model (see appendix).

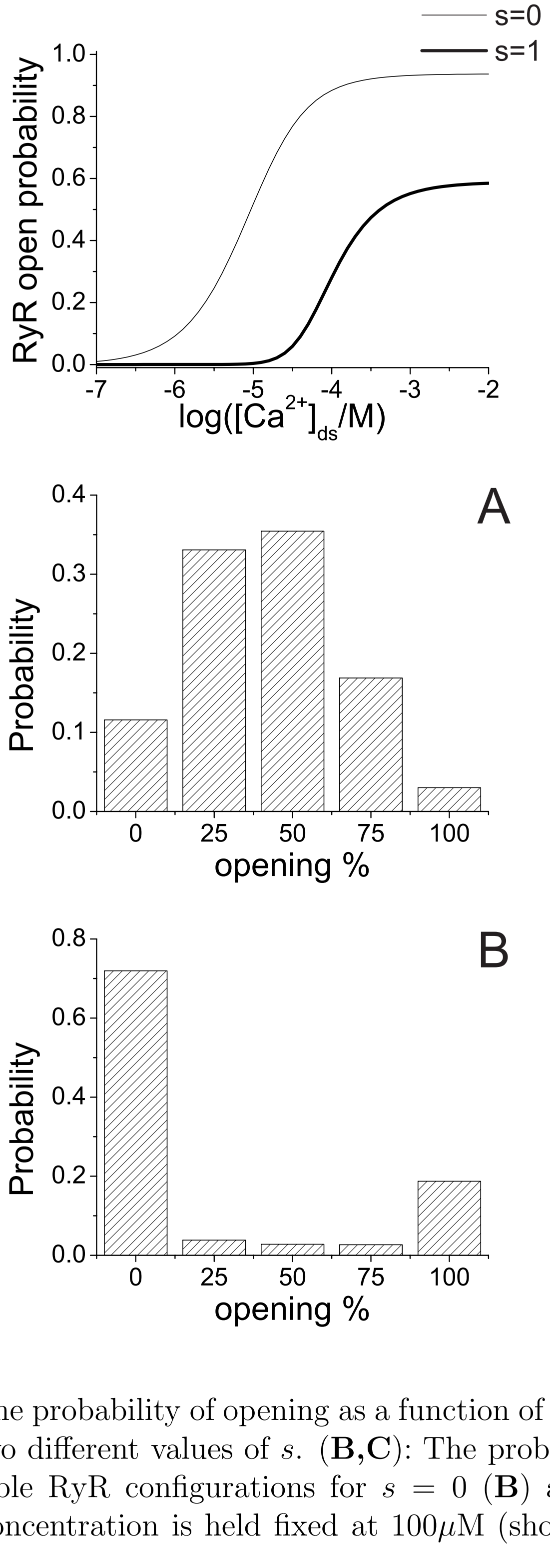

Figure IV.5: (**A**): The probability of opening as a function of the background Ca^{2+} concentration for two different values of s. (**B,C**): The probability of opening for each of the 5 possible RyR configurations for $s = 0$ (**B**) and $s = 1$ (**C**). The background Ca^{2+} concentration is held fixed at 100μM (shown as dashed line in (**A**)).

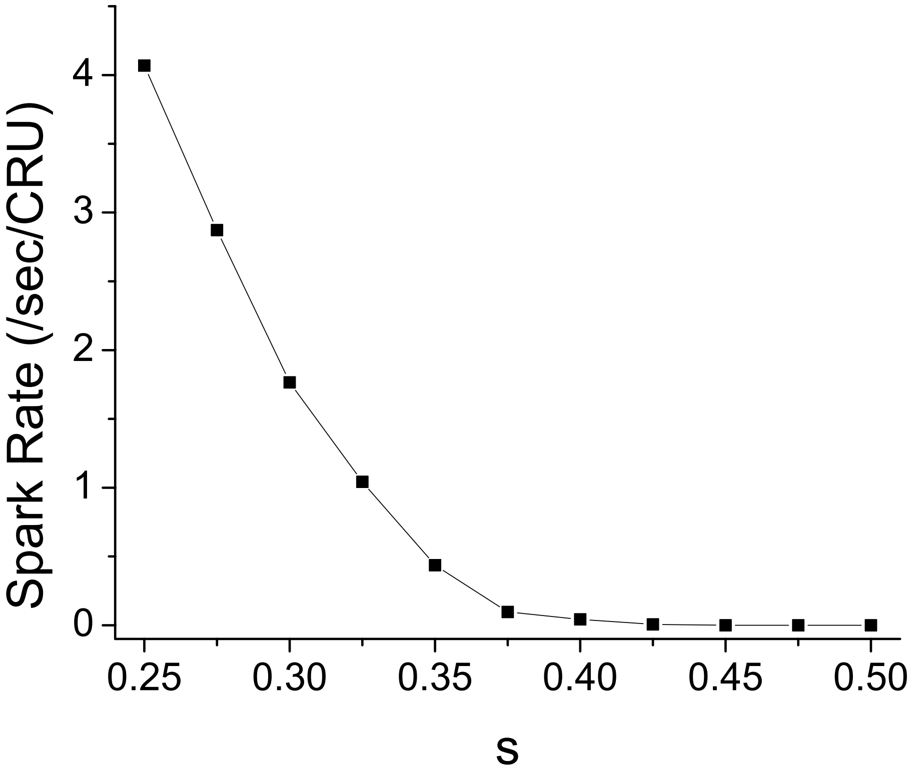

Figure IV.6: The spontaneous spark frequency as a function of the cooperativity s. There is very severe leak when s is small, and almost no sparks when $s > s^*$.

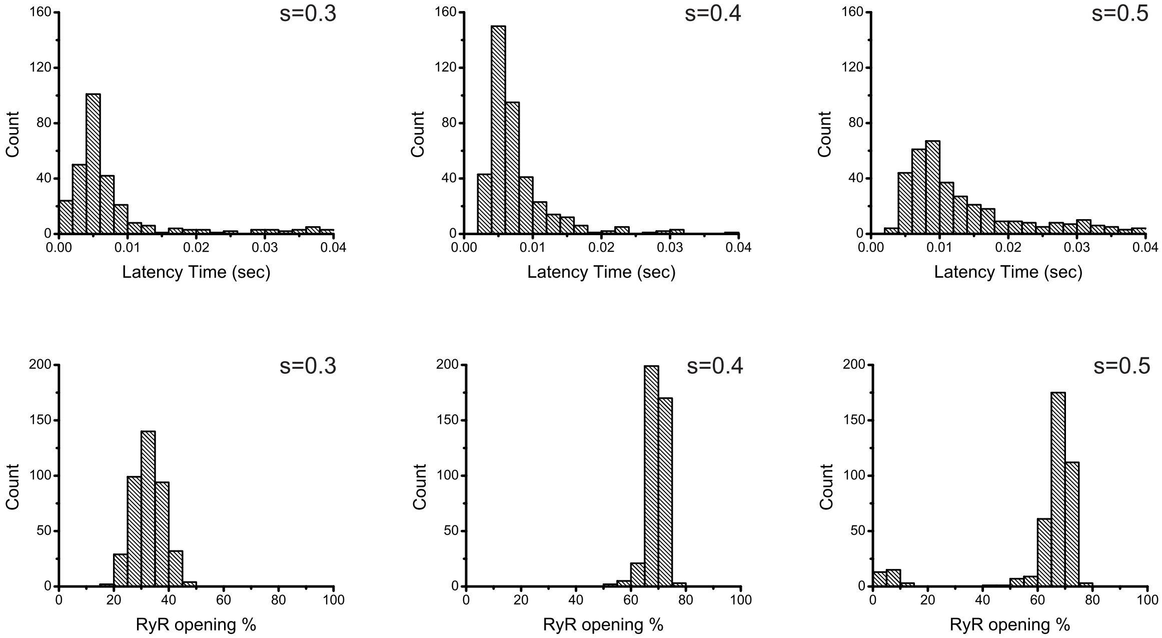

Figure IV.7: **A** The distributions of the latency time of the release triggered by the L-type channel current with varied level of cooperativity. **B** The corresponding distributions of the peak opening fraction during the release triggered by the L-type channel current.

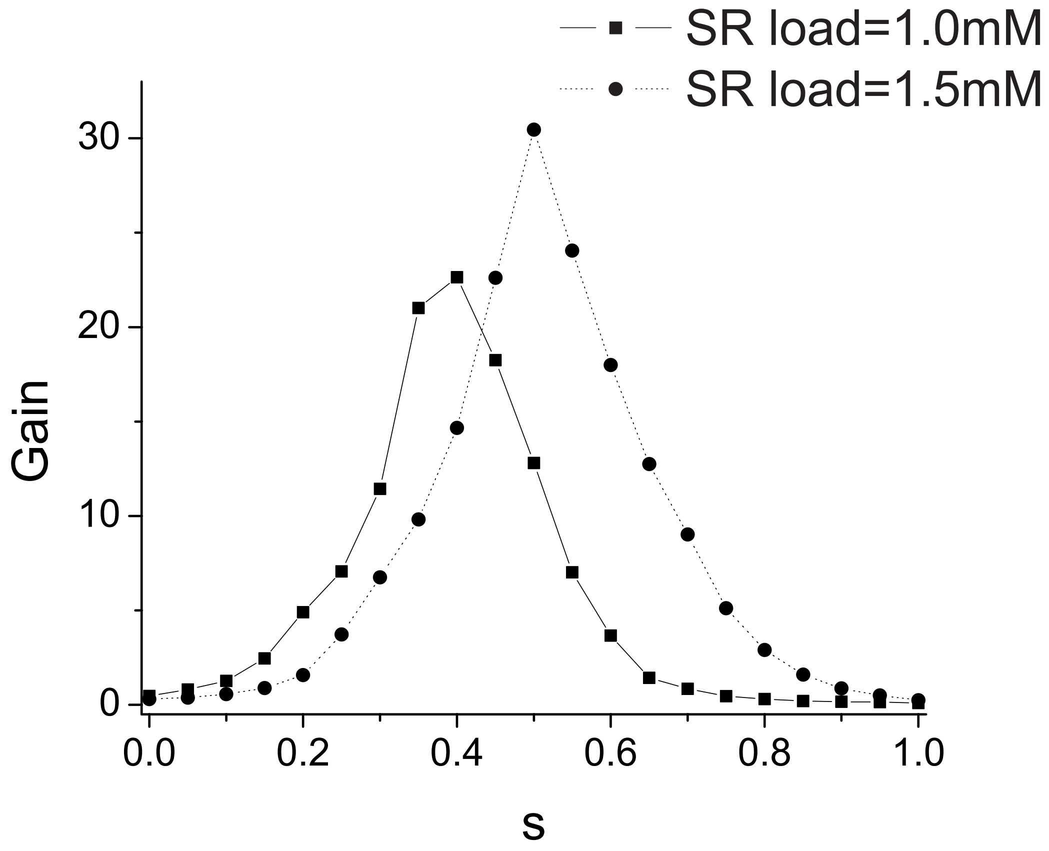

Figure IV.8: The gain as a function of the cooperativity for two different, fixed values of the SR content.

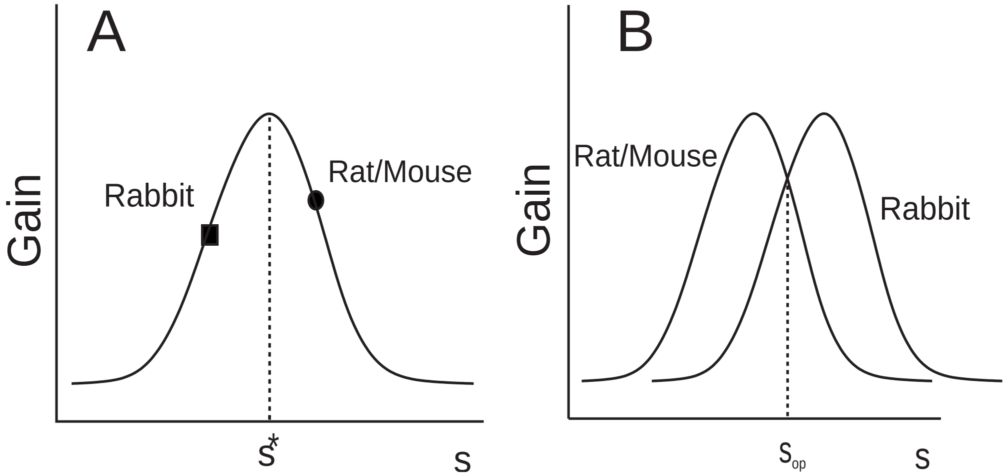

Figure IV.9: Possible schematic E-C coupling gain as a function of the FKBP association. (**A**): The gain function is the same for different species while the cooperativity level varies. The postulated operating point for rabbits is marked by a square while the operating point for mice and rats is marked by a circle. (**B**): The cooperativity is the same across species while the gain function is different.

IV.E Appendix: Description of the Full Model

In the main text we used a full model to validate the simple model in Figure 4. In this section, we describe in detail the construction of this full model, their corresponding equations, and parameter settings.

In this full model, we simulate N_{sim} calcium release units(CRU) simultaneously. Each CRU has its own L-type channels, RyRs and corresponding junctional SR. All CRUs are linked by sharing a common cytoplasm and network SR. The calcium dynamics in these 4 kind of pools are described by the following equations. Note that the subscript i denotes i^{th} CRU, and V_{cyto} and V_{nSR} are the volumes per CRU.

$$\frac{dCa^{2+}_{ds,i}}{dt} = J_{RyR,i} + J_{dhpr,i} + J_{Buf,i} - J_{efflux,i} \tag{IV.11}$$

$$\frac{dCa^{2+}_{jSR,i}}{dt} = \beta_{jSR,i}(-\frac{V_{ds}}{V_{jSR}} J_{RyR,i} + J_{refill,i}) \tag{IV.12}$$

$$\frac{dCa^{2+}_{cyto}}{dt} = \beta_{cyto}(\frac{1}{N_{sim}} \sum_i \frac{V_{ds}}{V_{cyto}} J_{efflux,i} - J_{SERCA} - J_{trpn} - \frac{A_{cap}C_{sc}}{2FV_{cyto}}(I_{Ca,b} - 2I_{NaCa} + I_{p(Ca)})) \tag{IV.13}$$

$$\frac{dCa^{2+}_{nSR}}{dt} = -\frac{1}{N_{sim}} \sum_i \frac{V_{jSR}}{V_{nSR}} J_{refill,i} + \frac{V_{cyto}}{V_{nSR}} J_{SERCA} \tag{IV.14}$$

All the flux described in the simple model are the same here. The fast buffer approximation in cytoplasm (calmodulins) and junctional SR (calsequestrins) are given by:

$$\beta_{cyto} = \frac{1}{1 + \frac{B_{CMDN}K_{CMDN}}{(K_{CMDN} + Ca^{2+}_{cyto})^2}} \tag{IV.15}$$

$$\beta_{jSR,i} = \frac{1}{1 + \frac{B_{CSQN}K_{CSQN}}{(K_{CSQN} + Ca^{2+}_{jSR,i})^2}} \tag{IV.16}$$

All the slow buffer dynamics are simulated according to Eq.IV.17. In the dyadic space these buffers include calmodulins, SR membrane buffers (BSR) and sarcolemmal membrane buffers (BSL). In Eq.IV.11 J_{Buf} is the sum of these 3 buffering flux. In cytoplasm they include high-sensitive troponins (HTRPN) and low-sensitive troponins (LTRPN). In Eq.IV.13 J_{trpn} is the sum of these 2 buffering flux. The total buffer amount B_j, dissociation constant K_j, on-rate $k_{j,on}$ and off-rate $k_{j,off}$ for each kind of buffer j are given in Table IV.3.

$$\frac{d[CaB_j]}{dt} = k_{j,on}[Ca]([B_j] - [CaB_j]) - k_{j,off}[CaB_j] \tag{IV.17}$$

We adopt the SERCA pump mechanism from a recent model by Shannon et al with parameters provided in Table IV.4:

$$J_{SERCA} = K_{sr}\frac{V_{mf}(\frac{[Ca^{2+}]_{cyto}}{K_{mf}})^H - V_{mr}(\frac{[Ca^{2+}_{nSR}]}{K_{mr}})^H}{1 + (\frac{[Ca^{2+}]_{cyto}}{K_{mf}})^H + (\frac{[Ca^{2+}]_{nSR}}{K_{mr}})^H} \tag{IV.18}$$

The sodium-calcium exchanger reads:

$$I_{NaCa} = k_{NaCa}\frac{e^{\frac{\eta VF}{RT}}[Na^+]_i^3 Ca_o^{2+} - e^{\frac{(\eta-1)VF}{RT}}[Na^+]_o^3 Ca_{cyto}^{2+}}{(1 + k_{sat}e^{\frac{(\eta-1)VF}{RT}})(K_{m,Na}^3 + [Na^+]_o^3)(K_{m,Ca} + Ca_o^{2+})} \tag{IV.19}$$

The other two plasma membrane calcium currents are:

$$I_{p(Ca)} = \overline{I_{p(Ca)}}\frac{Ca_{cyto}^{2+}}{K_{p(Ca)} + Ca_{cyto}^{2+}} \tag{IV.20}$$

$$I_{Ca,b} = G_{Ca,b}(V - E_{Ca}) \tag{IV.21}$$

where Nernst potential for calcium E_{Ca} reads:

$$E_{Ca} = \frac{RT}{2F}ln(\frac{Ca_o^{2+}}{Ca_{cyto}^{2+}}) \tag{IV.22}$$

150 beats are simulated in each run. The first 50 beats work as a warm-up to ensure the system reach the steady state, and data are collected from averaging the following 100 beats. Due to the limit of computation time, we only simulate 100 CRUs ($N_{sim} = 100$). But we tested simulations with a larger N_{sim} and it shows no significant difference.

Table IV.3: Buffering Parameters

Parameter	Value	Reference
$[B_{CMDN}]$	50μM	Greenstein and Winslow, 2002
K_{CMDN}	2.38μM	Greenstein and Winslow, 2002
$k_{CMDN,on}$	$100/\mu$M/s	Sobie et al, 2002
$[B_{CSQN}]$	13.5mM	Greenstein and Winslow, 2002
K_{CSQN}	0.63mM	Greenstein and Winslow, 2002
$[B_{BSL}]$	1124μM	Sobie et al, 2002
$k_{BSL,on}$	$115/\mu$M/s	Sobie et al, 2002
$k_{BSL,off}$	1000/s	Sobie et al, 2002
$[B_{BSR}]$	47μM	Sobie et al, 2002
$k_{BSR,on}$	$115/\mu$M/s	Sobie et al, 2002
$k_{BSR,off}$	100/s	Sobie et al, 2002
$[B_{HTRPN}]$	140μM	Iyer et al, 2004
$k_{HTRPN,on}$	$20/\mu$M/s	Iyer et al, 2004
$k_{HTRPN,off}$	0.066/s	Iyer et al, 2004
$[B_{LTRPN}]$	70μM	Iyer et al, 2004
$k_{LTRPN,on}$	$40/\mu$M/s	Iyer et al, 2004
$k_{LTRPN,off}$	40/s	Iyer et al, 2004

Table IV.4: SERCA Pump Parameters

Parameter	Value	Reference
K_{sr}	2.6	(Shannon et al, 2004)
K_{mf}	0.246μM	(Shannon et al, 2004)
K_{mr}	1700μM	(Shannon et al, 2004)
V_{mf}	286μM/cytosol/s	(Shannon et al, 2004)
V_{mr}	286μM/cytosol/s	(Shannon et al, 2004)
H	1.787	(Shannon et al, 2004)

Table IV.5: Sodium-calcium Exchanger Parameters

Parameter	Value	Reference
k_{NaCa}	1500μA/μF	Greenstein and Winslow, 2002
$K_{m,Na}$	87.5mM	Greenstein and Winslow, 2002
$K_{m,Ca}$	1.38mM	Greenstein and Winslow, 2002
k_{sat}	0.2	Greenstein and Winslow, 2002
η	0.35	Greenstein and Winslow, 2002
$[Na^+]_i$	10mM	Greenstein and Winslow, 2002
$[Na^+]_o$	138mM	Greenstein and Winslow, 2002
Ca_o^{2+}	2mM	Greenstein and Winslow, 2002

Table IV.6: Membrane Calcium Exchanges, Background Current

Parameter	Value	Reference
$K_{p(Ca)}$	0.5μM	Grrenstein and Winslow, 2002
$\overline{I_{p(Ca)}}$	0.05μA/μF	Grrenstein and Winslow, 2002
$G_{Ca,b}$	0.254μS/μF	Grrenstein and Winslow, 2002

Bibliography

[1] Bers D. (2001) Excitation-contraction coupling and cardiac contractile force. Kluwer, Boston.

[2] Hasenfuss, G., & Pieske, B. (2002) Calcium cycling in congestive heart failure. *J. Mol. Cell Cardiol.* **34,** 261-286.

[3] Sjaastad, I., Wasserstrom, J. A. & Sejersted, O. M. (2002) Heart failure - a challenge to our current concepts of excitation-contraction coupling. *J. Physiol.* **546,** 33-47.

[4] Parker, M. (1985) Sudden unexpected death in patients with congestive heart failure: A second frontier. *Circulation.* **72,** 681-685.

[5] Bers, D. (2000) Calcium fluxes involved in control of cardiac myocyte contraction. *Circ. Res.* **87,** 275-281.

[6] Bers, D. M., Eisner, D. A. & Valdivia, H. H. (2003. Sarcoplasmic reticulum Ca2+ and heart failure: roles of diastolic leak and Ca2+ transport. *Circ. Res.* **93,** 487-490.

[7] Marks, A. R. (2003) A guide for the perplexed: towards an understanding of the molecular basis of heart failure. *Circulation* **107,** 1456-1459.

[8] Brillantes A. B., Ondrias, K., Scott, A., Kobrinsky, E., Ondriasova, E., Moschella, M. C., Jayaraman, T., Landers, M., Ehrlich, E. E. & Marks, A. R. (1994) Stabilization of calcium release channel (ryanodine receptor) function by FK506-binding protein. *Cell* **77,** 513-523.

[9] Ahern, G. P., Junankar, P. R. & Dulhunty, A. F. (1997) Subconductance states in single-channel activity of skeletal muscle ryanodine receptors after removal of FKBP12. *Biophys. J.* **72,** 146-162.

[10] McCall, E., Li, L., Satoh, H., Shannon, T. R., Blatter, L. A. & Bers, D. M. (1996) Effects of FK-506 on contraction and Ca2+ transients in rat cardiac myocytes. *Circ. Res.* **79,** 1110-1121.

[11] Xin, H. B., Senbonmatsu, T., Cheng, D. S., Wang, Y. X., Copello, J. A., Ji, G. J., Collier, M. L., Deng, K. Y., Jeyakumar, L. H., Magnuson, M. A., Inagami,

T., Kotlikoff, M. I. & Fleischer, S. (2002) Oestrogen protects FKBP12.6 null mice from cardiac hypertrophy. *Nature* **416,** 334-338.

[12] Su, Z., Sugishita, K., Li, F., Ritter, M. & Barry W. H.. (2003) Effects of FK506 on [Ca2+]i differ in mouse and rabbit ventricular myocytes. *J. Pharmacol. Exp. Ther.* **304,** 334-341.

[13] Prestle, J., Janssen, P. M., Janssen, A. P., Zeitz, O., Lehnart, S. E., Bruce, L., Smith, G. L. & Hasenfuss, G. (2001) Overexpression of FK506-binding protein FKBP12.6 in cardiomyocytes reduces ryanodine receptor-mediated Ca(2+) leak from the sarcoplasmic reticulum and increases contractility. *Circ. Res.* **88,** 188-194.

[14] Loughrey, C. M., Seidler, T., Miller, S. L., Prestle, J., MacEachern, K. E., Reynolds, D., Hasenfuss, G. & Smith, G. L. (2004) Over-expression of FK506-binding protein FKBP12.6 alters E-C coupling in adult rabbit cardiomyocytes. *J. Physiol.* **556,** 919-934.

[15] Gomez, A. M., Schuster, I., Fauconnier, J., Prestle, J., Hasenfuss, G. & Richard, S. (2004) FKBP12.6 overexpression decreases Ca2+ spark amplitude but enhances [Ca2+]i transient in rat cardiac myocytes. Am. J. Physiol. Heart Circ. Physiol. 287:H1987–H1993. *Am. J. Physiol. Heart Circ. Physiol.* **287,** H1987-H1993.

[16] Hain, J., Onoue, H., Mayrleitner, M., Fleischer, S. & Schindler, H. (1995) Phosphorylation modulates the function of the calcium release channel of sarcoplasmic reticulum from cardiac muscle. J. Biol. Chem. 270:2074–2081. *J. Biol. Chem.* **270,** 2074-2081.

[17] Valdivia, H. H., Kaplan, J. H., Ellis-Davies, G. C. & Lederer, W. J. (1995) Rapid adaptation of cardiac ryanodine receptors: modulation by Mg2+ and phosphorylation. *Science* **267,** 1997-2000.

[18] Marks, A. R., Reiken, S. & Marx, S. O. (2002) Progression of heart failure: is protein kinase A hyperphosphorylation of the ryanodine receptor a contributing factor? *Circulation* **105,** 272-275.

[19] Marx, S. O., Reiken, S., Hisamatsu, Y., Jayaraman, T., Burkhoff, D., Rosemblit, N. & Marks, A. R. (2000) PKA phosphorylation dissociates FKBP12.6 from the calcium release channel (ryanodine receptor): defective regulation in failing hearts. *Cell* **101,** 365-376.

[20] Ono, K., Yano, M., Ohkusa, T., Kohno, M., Hisaoka, T., Tanigawa, T., Kobayashi, S., Kohno, M. & Matsuzaki, M. (2000) Altered interaction of FKBP12.6 with ryanodine receptor as a cause of abnormal Ca(2+) release in heart failure. *Cardiovasc. Res.* **48,** 323-331.

[21] Yano, M., Kobayashi, S., Kohno, M., Doi, M., Tokuhisa, T., Okuda, S., Suetsugu, M., Hisaoka, T., Obayashi, M., Ohkusa, T., Kohno, M. & Matsuzaki, M. (2003) FKBP12.6-mediated stabilization of calcium-release channel (ryanodine receptor) as a novel therapeutic strategy against heart failure. *Circulation* **107,** 477-484.

[22] Wehrens, X. H., Lehnart, S. E., Huang, F., Vest, J. A., Reiken, S. R., Mohler, P. J., Sun, J., Guatimosim, S., Song, L. S., Rosemblit, N., D'Armiento, J. M., Napolitano, C., Memmi, M., Priori, S. G., Lederer, W. J. & Marks, A. R. (2003) FKBP12.6 deficiency and defective calcium release channel (ryanodine receptor) function linked to exercise-induced sudden cardiac death. *Cell* **113,** 829-840.

[23] Wehrens, X. H., Lehnart, S. E., Reiken, S. R., Deng, S. X., Vest, J. A., Cervantes, D., Coromilas, J., Landry, D. W. & Marks, A. R. (2004) Protection from cardiac arrhythmia through ryanodine receptor-stabilizing protein calstabin2. *Science* **304,** 292-296.

[24] Sobie, E. A., Dilly, K. W., dos Santos Cruz, J., Lederer, W. J. & Jafri, M. S. (2002) Termination of cardiac Ca(2+) sparks: an investigative mathematical model of calcium-induced calcium release. *Biophys. J.* **83,** 59-78.

[25] Greenstein, J. L. & Winslow, R. L. (2002) An integrative model of the cardiac ventricular myocyte incorporating local control of Ca2+ release. *Biophys. J.* **83,** 2918-2945.

[26] Iyer, V., Mazhari, R. & Winslow, R. L. (2004) A computational model of the human left-ventricular epicardial myocyte. *Biophys. J.* **87,** 1507-1525.

[27] Stern, M. D., Song, L. S., Cheng, H., Sham, J. S., Yang, H. T., Boheler, K. R. & Rios,E. (1999) Local control models of cardiac excitation-contraction coupling. A possible role for allosteric interactions between ryanodine receptors. *J. Gen. Physiol.* **113,** 469-489.

[28] Franzini-Armstrong, C., Protasi, F. & Ramesh, V. (1999) Shape, size, and distribution of Ca(2+) release units and couplons in skeletal and cardiac muscles. *Biophys. J.* **77,** 1528-1539.

[29] Wier, W. G., Egan, T. M., Lopez-Lopez, J. R. & Balke, C. W. (1994) Local control of excitation-contraction coupling in rat heart cells. *J. Physiol.* **474,** 463-471.

[30] Cannell, M. B., Cheng, H. & Lederer, W. J. (1995) The control of calcium release in heart muscle. *Science* **268,** 1045-1049.

[31] Janczewski, A. M., Spurgeon, H. A., Stern, M. D. & Lakatta, E. G. (1995) Effects of sarcoplasmic reticulum Ca2+ load on the gain function of Ca2+ release by Ca2+ current in cardiac cells. *Am. J. Physiol.* **268,** H916-H920.

[32] Song, L. S., Wang, S. Q., Xiao, R. P., Spurgeon, H., Lakatta, E. G. & Cheng, H. (2001) β-adrenergic stimulation synchronizes intracellular Ca^{2+} release during excitation-contraction coupling in cardiac myocytes. *Circ. Res.* **88,** 794-801.

[33] Viatchenko-Karpinski, S. & Gyorke, S. (2001) Modulation of the Ca^{2+}-induced Ca^{2+} release cascade by β-adrenergic stimulation in rat ventricular myocytes. *J. Physiol.* **533,** 837-848.

[34] Falcke, M., Tsimring, L. & Levine, H. (2000) Stochastic spreading of intracellular Ca(2+) release. *Phys. Rev. E* **62,** 2636-2643.

[35] Wherens, X. H. T. & Marks, A. R. (2003) Altered function and regulation of cardiac ryanodine receptors in cardiac disease. *Trends Biochem. Sci.* **28,** 671-678.

[36] Li, G., Lau, C., Ducharme, A., Tardif, J. & Nattel, S. (2002) Transmural action potential and ionic current remodeling in ventricles of failing canine hearts. *Am. J. Physiol. Heart Circ. Physiol.* **283,** H1031-H1041.

[37] Jiang, M. T., Lokuta, A. J., Farrell, E. F., Wolff, M. R., Haworth, R. A. & Valdivia, H. H. (2002) Abnormal Ca2+ release, but normal ryanodine receptors in canine and human heart failure. *Circ. Res.* **91,** 1015-1022.

[38] Xiao, B., Sutherland, C., Walsh, M. P. & Chen, S. R. W. (2004) Protein kinase A phosphorylation at serine-2808 of the cardiac Ca2+-release channel (Ryanodine receptor) does not dissociate 12.6-kDa FK506-binding protein (FKBP12.6). *Circ. Res.* **94,** 487-495.

[39] Wehrens, X. H. T., Lehnart, S. E., Huang, F., Vest, J. A., Reiken, S. R., Mohler, P. J., Sun, J., Guatimosim, S., Song, L.-S., Rosemblit, N., D'Armiento, J. M., Napolitano, C., Memmi, M., Priori, S. G., Ledere, W. J. & Marks, A. R. (2001) FKBP12.6 Deficiency and Defective Calcium Release Channel (Ryanodine Receptor) Function Linked to Exercise-Induced Sudden Cardiac Death. *Cell* **113,** 829-840.

[40] Marx, S. O., Ondrias, K. & Marks, A. R. (1998) Coupled gating between individual skeletal muscle Ca2+ release channels (ryanodine receptors). *Science* **281,** 818-821.

[41] Marx, S. O, Gaburjakova, J., Gaburjakova, M., Henrikson, C., Ondrias, K. & Marks, A. R. (2001) Coupled gating between cardiac calcium release channels (ryanodine receptors). *Circ. Res.* **88,** 1151-1158.

V

Measuring Intercellular Signals with Arbitrary Accuracy

The interaction between an external diffusing stimulus and cell receptors has long been recognized as a stochastic process [1]. At the level of a single receptor, this process is inherently stochastic, but cells can contain many such receptors which can reduce the variability in the detected signal by suitable averaging. It is therefore of interest to characterize the residual noise in this measurement as a function of interaction kinetics, signal integration time, and receptor number.

In their classic paper on the physics of chemoreception, Berg and Purcell [2] argued for an irreducible level of noise encountered whenever a cell utilizes receptors to detect local concentrations of diffusing molecules. Using heuristic arguments, they proposed that for large receptor number the normalized variance in the concentration c approaches

$$\left(\frac{\delta c}{\bar{c}}\right)^2 \simeq \frac{1}{DT\bar{c}R} \tag{V.1}$$

Here D is the diffusivity of the molecule with mean concentration $\bar{c}$, R is the cell radius and T is the measurement time, implemented by the downstream signaling circuitry. This result was re-derived by Bialek and Setayeshgar by using a fluctuation-dissipation approach [3]. This leaves the impression that a cell cannot achieve arbitrary accuracy by increasing its receptor number; its only option would be to increase the measurement time T, which may be an impractical solution for a dynamically changing environment. We will show by direct stochastic simulation and by physical reasoning that this conclusion is unwarranted.

V.A Methods

We start by focusing on the most common interaction between a ligand L and a receptor:

$$L + R_0 \rightleftharpoons R_1 \tag{V.2}$$

The forward rate $k_+[L]$, where $[L]$ represents the ligand concentration, and backward rate k_- determine the transitions between the unoccupied R_0 and occupied R_1 states and can be combined to give the dissociation constant $K_d \equiv \frac{k_-}{k_+}$.

To study the stochastic dynamics of this model, we performed numerical simulations using MCell3, a modeling tool for realistic simulation of cellular signaling in complex three dimensional geometries [4]. MCell uses highly optimized Monte Carlo algorithms to track the stochastic behavior of discrete molecules in space and time as they diffuse in user-specified geometries. It can model interactions between diffusing molecules and receptors on cell membranes as well as molecule-molecule interactions and has been validated extensively [4].

In our simulations, we modeled the cell as a 5 μm radius sphere, rendered by 100 triangles (Fig. V.E). The surface of the cell was divided into tiny patches and each patch could hold at most one receptor. The patch density was taken to be $1000/\mu\text{m}^2$, resulting in a receptor size of 1000 nm^2. We have verified that simulations with smaller receptor sizes show no observable differences for the parameters we are considering here. A variable number of N receptors ($N = 20000 - 300000$) were randomly distributed on the membrane of the cell. Each receptor can bind one ligand and the dissociation constant was taken to be $K_d = 30$ nM and the unbinding rate as $k_- = 10\ \text{s}^{-1}$.

Our cell was placed in a cubic box with sides of size 30 μm. To reduce finite-box effects and to save computation time, we incorporated a specific concentration-clamp boundary condition in MCell3. In this condition, we imagine our computational box to be immersed in a much larger box with the same ligand concentration that functions as a reservoir. Molecules from this reservoir can enter the computational box at a random location and at a rate that equals the escape rate of molecules from the computational box to the reservoir. The latter can be calculated analytically and depends on system parameters and the time step. Note that this boundary condition neglects any possible correlation between outgoing and incoming molecule. Hence, the measured correlation function (see below) will be underestimated for large times. We refer to the Appendix for more details on the dependence of the numerical results on the box size and time step size.

Each simulation simulated 50 seconds and the time step was 10 μs. At the start of a simulation, a certain amount of ligand molecules are released into the box and diffuse freely with diffusion constant $D = 200\,\mu\text{m}^2/\text{s}$. Once a ligand hits a receptor, it can either bind to it or be reflected off the membrane. MCell3 calculates the binding probability based on the reaction rates, ligand diffusivity, receptor size and time step. After an initial transient period of 10 s, during which the system reaches equilibrium, the number of bound receptors was recorded every 1 ms. A snapshot of a simulation is shown in Fig. V.E.

Two types of measurements are identified. With N receptors in total, an instantaneous measurement is defined as

$$Z(t) = \frac{1}{N}\sum_{i}^{N} r_i \tag{V.3}$$

where r_i is a binary random variable taking the value 0 if the i^{th} receptor is in the R_0 state and 1 if the i^{th} receptor is in the R_1 state. To compare directly with Burg-Purcell's result, we define a time-averaged measurement of receptor occupancy ias an average of instantaneous measurements over a time window T:

$$Z_T(t) = \frac{1}{T}\int_{t-T}^{t} d\tau Z(\tau) \tag{V.4}$$

For each simulation, we measured both the instantaneous receptors occupancy $Z(t)$ and the time-averaged measurement $Z_T(t)$, for $T = 10/k_- = 1\,s$, as well as the correlation function $C(\tau) = \int (Z(t) - \bar{Z})(Z(t+\tau) - \bar{Z})dt$. The latter is only calculated for $\tau < 4$ s; for larger values of τ the correlation function is overwhelmed by fluctuations. The mean and variance of $Z(t)$ were estimated in the following standard way:

$$\bar{Z} = \frac{1}{N_{data}} \sum_{j=1}^{N_{data}} Z_j \tag{V.5}$$

$$\sigma_Z^2 = \frac{1}{N_{data} - 1} \sum_{j=1}^{N_{data}} (Z_j - \bar{Z})^2 \tag{V.6}$$

where N_{data} is the number of time stamps obtained from a single simulation. The ensemble average and variance of the estimated variances are estimated by repeating each simulation 10 times.

The ensemble average of the correlation function is fit to an exponential, $C(\tau) \sim \exp(-\tau/\tau_c)$, to obtain an estimate of the correlation time scale τ_c. The variance in the receptor occupancy is simply proportional to the variance in the concentration of Eq. V.1 (see Eq. V.13).

V.B Results

V.B.1 Instantaneous measurements

Fig. V.Ea shows the variance σ_Z^2 of the instantaneous measurement $Z(t)$ as a function of receptor number N. The data, obtained by averaging over ten independent runs, is easily fit by the form $\sigma_Z^2 = A_0/N$ with the coefficient A_0 equal to

$$A_0 = \frac{\bar{c}K_d}{(\bar{c} + K_d)^2} \tag{V.7}$$

which is just the single receptor variance. This simple finding arises from the fact that once a molecule binds a receptor, it cannot affect neighboring receptors no matter how close-by they are located, until a finite time later when it is unbound. Hence instantaneous measurements at separate receptors are uncorrelated and the mean has accuracy that scales as $1/N$. Thus, utilizing a one-time measurement, the cell can attain arbitrary accuracy in its evaluation of a signal concentration.

V.B.2 Time-averaged measurements

To understand why this result appears to disagree with the Berg-Purcell conclusion, we consider now the time-averaged measurements, where T is the time interval over which the instantaneous measurement is averaged. As demonstrated in Fig. V.Eb, the data now do fit the expected finite residual formula $\sigma^2_{Z_T} = A_T/N + B_T$; the error cannot be less than B_T. The difference between the instantaneous measurement and the time averaged measurement is more easily appreciated when we write the variance as $\sigma^2 = A(1/N + 1/N_c)$. For the time averaged measurement we obtain $N_c = 1.1 \times 10^5$ while the instantaneous measurement results in a value of N_c that is nearly two orders of magnitude bigger ($N_c = 7.6 \times 10^6$).

V.B.3 Instantaneous measurements and time-averaged measurements are related

How can this occur? The answer is that as long as the integration time T is longer than the correlation time τ_c one needs to multiply the instantaneous data by a factor of $2\tau_c/T$ to obtain the time-averaged measurement. To see this, we start with the definition of the variance of the time-averaged measurement:

$$\sigma^2_{Z_T} = \left\langle \left(\frac{1}{T} \int_0^T (Z(t) - \bar{Z}) dt \right)^2 \right\rangle = \frac{1}{T^2} \int_0^T dt \int_0^T ds \, \langle Z(t) Z(s) \rangle - \bar{Z}^2$$

Next, we assume that the correlation function has an exponential decay:

$$\langle Z(t) Z(s) \rangle = \bar{Z}^2 + \sigma^2_Z e^{-\frac{|t-s|}{\tau_c}}$$

where τ_c is the correlation time. Performing the integrals leads to:

$$\sigma^2_{Z_T} = \frac{2\sigma^2_Z \tau_c}{T^2}(T - \tau_c(1 - e^{-T/\tau_c})) \tag{V.8}$$

The relationship between the two variances can be simplified for $T >> \tau_c$ where it becomes $\sigma^2_{Z_T} = \frac{2\sigma^2_Z \tau_c}{T}$. Thus, to obtain the variance of the time-averaged measurement, one needs to multiply the variance of the instantaneous measurement with the correlation time. For our system, this correlation time *diverges* as N for large receptor number which can be demonstrated directly in our simulations (Fig. V.E). Hence, $\tau_c \sim \Lambda N$ which leads to the residual term

$$B_T = \frac{2\Lambda A_0}{T}, \tag{V.9}$$

consistent with our computational data.

Where does this diverging time come from? The receptor surface density for our cell is obviously $\rho = N/4\pi R^2$. Thus, the expected number of bound receptors per unit surface area is $\rho\bar{c}/K_d$, where for simplicity we have considered the case $\bar{c} << K_d$, leading to $A_0 = \bar{c}/K_d$. In order for the molecules bound to these receptors to escape to infinity and hence for the configuration to be completely refreshed, we must wait a time equal to the correlation time:

$$\tau_c = \frac{1}{k_-} + \frac{\rho\bar{c}/K_d}{J_{diff}} = \frac{1}{k_-} + \frac{N}{4\pi D R K_d} \tag{V.10}$$

where the first term describes the average time for unbinding and where the diffusive flux is given by $J_{diff} = D\bar{c}/R$. (See Appendix V.F for an analytical calculation of τ_c.)

To test the scalings of τ_c, we start our simulation with a ratio of bound to unbound receptors equal to $\bar{c}/K_d$ and no free ligands. The box boundary is taken to be absorptive so once a ligand hits the boundary it is removed from the system. As in the full simulation, we record the number of bound receptors as a function of time which exhibits an exponential decay with time scale as the correlation time of receptor occupancy τ_c. Since we do not need to maintain a constant concentration of ligands in the entire computational box, this simulation is very fast and we use a box size of 120 μm and a time step of 1 μs to ensure accurate results. Figure V.E shows the correlation time as a function of the number of receptors for 5 different parameter sets: our "default" parameter set, used throughout the chapter, and sets in which one parameter is changed to the indicated value. The results show clearly that the correlation time increases linearly with N in all cases. Linear fits give the following values for the slope Λ:

Table V.1: Comparison of estimated Λ for different parameter sets.

Parameter Set	default	$k_- = 5s^{-1}$	$D = 400\mu m^2/s$	$R = 10\mu m$	$K_d = 60nM$
Λ(μs)	4.36 ± 0.03	4.34 ± 0.05	2.23 ± 0.02	2.12 ± 0.03	2.19 ± 0.03

The theoretical value of Λ is 4.406 μs for the default case. Clearly all the fitting results are very close to the predictions of Eq. V.32. Reducing k_- by a factor of 2 does not change the slope, but shifts the correlation time up by about 0.1s, consistent with Eq. V.32. Changing D, R or K_d by a factor of 2, on the other hand, changes the slope also by a factor of 2, validating Eq. V.32. In addition, we have performed a limited set of full simulations and have found that the correlation time depends on the system parameters as in Eq. V.32 (data not shown).

Combining Eq. V.8, Eq. V.32, and the condition $T >> \tau_c$, we immediately find

$$\sigma^2_{Z_T} = \frac{A_T}{N} + B_T = \sigma^2_Z \frac{2\tau_c}{T} = \frac{2A_0}{NT}(\frac{1}{k_-} + \frac{N}{4\pi DRK_d}) \tag{V.11}$$

and thus:

$$A_T = \frac{2A_0}{Tk_-} \quad \text{and} \quad B_T = \frac{\bar{c}}{2\pi DTRK_d^2} \tag{V.12}$$

The term B_T is in agreement with Eq. V.1 for small $\bar{c}$. The crucial point, however, is that this formula is valid only for long-enough times ($T > \tau_c$) and *does* *not* imply any irreducible diffusive noise limiting measurement accuracy. In fact, for any fixed measuring time T, there is a sufficiently large N such that $\tau_c(N) > T$, resulting in a variance that scales as $1/N$ just like the variance of instantaneous measurements. This is demonstrated in Fig. V.E where we have plotted $\sigma^2_{Z_T}$ as a function of the measurement time T, using Eq. V.8, for different number of receptors. On each curve we have marked the point where $T = \tau_c$; the collections of these points for different N is plotted as a dashed line. Below this line, T is much smaller than τ_c and the time-averaged variance approaches the instantaneous variance σ^2_Z.

Furthermore, the difference in the noise level estimated from Eq. V.1 and from our formula can become significant. To see this, we first need to relate the variance in concentration level $(\delta c/\bar{c})^2$ to the variance in the number of bound receptors $\sigma^2_{Z_T}$. The average occupancy level is given by $\bar{Z} = \bar{c}/(\bar{c} + K_d)$ from which we can derive $\delta c = (\bar{c} + K_d)^2 \delta Z / K_d$. Hence, the variance appearing in the Berg and Purcell expression is simply the variance in the number of bound receptors multiplied by a factor that depends on the average concentration and the dissociation constant:

$$\left(\frac{\delta c}{\bar{c}}\right)^2 = \sigma^2_{Z_T} \left[\frac{(\bar{c} + K_d)^2}{\bar{c} K_d}\right]^2 \tag{V.13}$$

In Fig. V.E we have plotted $(\delta c/\bar{c})^2$ as a function of the diffusion constant as predicted by Eq. V.1 (dashed line) and by our general formulas Eq. V.8 and Eq. V.13 (solid line). For small diffusion constants, where the larger correlations time becomes larger than the averaging time, the difference between the two formulas becomes appreciable and a simple application of the Berg and Purcell formula would significantly overestimate the noise level.

V.B.4 Alternative reaction models

It is interesting to note that our conclusions depend on the interaction details. To study this, we considered an alternate model in which the diffusing molecule, L, acts enzymatically on the receptor:

$$\begin{aligned} L + R_0 &\rightarrow L + R_1 \\ R_1 &\rightarrow R_0 \end{aligned} \tag{V.14}$$

where the forward and backward rate are identical to the ones in the binding-unbinding model. Now, the fact that the diffusing particle is not absorbed by the receptor means that it can act in rapid succession on neighboring receptors, thereby correlating their response. In the limit of infinite N, this can happen with infinitesimal time-lags and the resulting correlations limit the achievable accuracy. In fact, the variance of the instantaneous measurement for this case is

$$\sigma_Z^2 = A_0\left(\frac{1}{N} + \frac{1}{N_c}\right) \tag{V.15}$$

where

$$N_c = 8\pi R^2 K_d (1+\tilde{c})^{3/2} \sqrt{\frac{D}{k_-}} \cdot \frac{1}{1 - e^{-2R\sqrt{\frac{k_-(1+\tilde{c})}{D}}}} \tag{V.16}$$

and $\tilde{c} = \bar{c}/K_d$. The details of this calculation is shown in Appendix V.G. Figure V.E (red circles) shows the simulation results of σ_Z^2 does not vanish for large N but remains finite and it fits very well with the theoretical prediction. It is not clear whether there are any direct realizations of this alternate scheme. However, more complex models in which the decay of the bound ligand-receptor pair leaves the receptor at least temporarily in the signaling-competent state will behave in the enzymatic way whenever the dissociation rate is fast compared to the final rate of decay.

V.C Experimental relevance

This new understanding of the way in which fluctuations limit measurement accuracy will become relevant whenever cells utilize measurements with integration times less than the receptor array correlation τ_c. The most intriguing possible example arises in the case of the chemotactic sensing of f-Met-Leu-Phe by neutrophils [5]. Eukaryotic chemotaxis is a difficult task, as the signal is created by a small difference between front and rear concentrations whereas the noise is due to the mean occupancy [6]. Typical interaction numbers for this system are $k_- \simeq 2/\text{s}$, $K_d \simeq 15 - 50$ nM, for a cell of radius $6 - 8$ μm [7, 8]. The number of receptors is regulated, increasing from $N = 40,000$ to $N = 150,000$ when the neutrophil is activated by cytokines [9, 10]. With a typical small-molecule diffusivity of $200\,\mu\text{m}^2/\text{s}$, we estimate a τ_c of approximately one second, but this could be increased by experimental manipulation of the extracellular medium. Rapidly advancing microfuidics technology [11, 12] should enable a test of whether and when the neutrophil sensing must be thought of as instantaneous, being governed directly by the individual receptor variance. Once this occurs, the ultimate limit (in evolutionary terms) of gradient detection would be set by considerations other than diffusion, perhaps by noise in the downstream processing system or by trade-offs with other needs for cell surface "real estate".

V.D Applications in modeling gradient detection

This work has important implications in modeling eukaryotic gradient detection. Usually in those models the membrane receptor occupancy works as the input of the whole signaling pathway, and the fluctuation of the occupancy is not considered, or considered in a simple way. Our work reveals this fluctuation has a relatively complicated time correlations due to the rebinding of ligands. We can construct sample input sequences for those models according to this particular correlation, and make the modeling more accurate. For example, in a 1-dimensional gradient detection model, the correct self-correlation for one end of the cell is an exponential decay,

$$C_{self}(t_2 - t_1) = A_s \exp(-|t_2 - t_1|/\tau_s) \tag{V.17}$$

and the cross-correlation between the front and the back can be fit to

$$C_{cross}(t_2 - t_1) = A_c |t_2 - t_1| \exp(-|t_2 - t_1|/\tau_c) \tag{V.18}$$

This cross-correlation starts from 0 and has a peak at τ_c, marking the maximal rebinding of molecules on one side originating from the other side. The A's and τ's can be obtained from a 3-D MCell simulation.

We can also measure the cross-correlations between different surface segments of a flat cylindric cell with MCell, and use this data to construct input signals for more abstracted 2-D models. By this approach, we found the local fluctuation of receptor activity can be as large as the difference of the mean signals across the cell, and a model which is very sensitive to local receptor activity may not be able to work properly and detect the right gradient direction. This difficulty is never considered in previous models. The key idea is the cell must have some mechanism to spatially average the signal. The range of this spatial average must be at least comparable with the spatial scale of the cross-correlation, while its still small comparing to the cell's size. We found allowing 2-D diffusion of membrane receptors can help this situation and smooth out the local fluctuations to some extent.

V.E Acknowledgements

The text of chapter V, in part, is a reprint of the material as it appears in Kai Wang, Wouter-Jan Rappel, Rex Kerr and Herbert Levine, *Measuring Intercellular Signals with Arbitrary Accuracy*, Submitted to Proc. Natl. Acad. Sci., where the dissertation author was the first author. The co-authors in this publication directed, supervised, and co-worked on the research which forms the basis of this chapter.

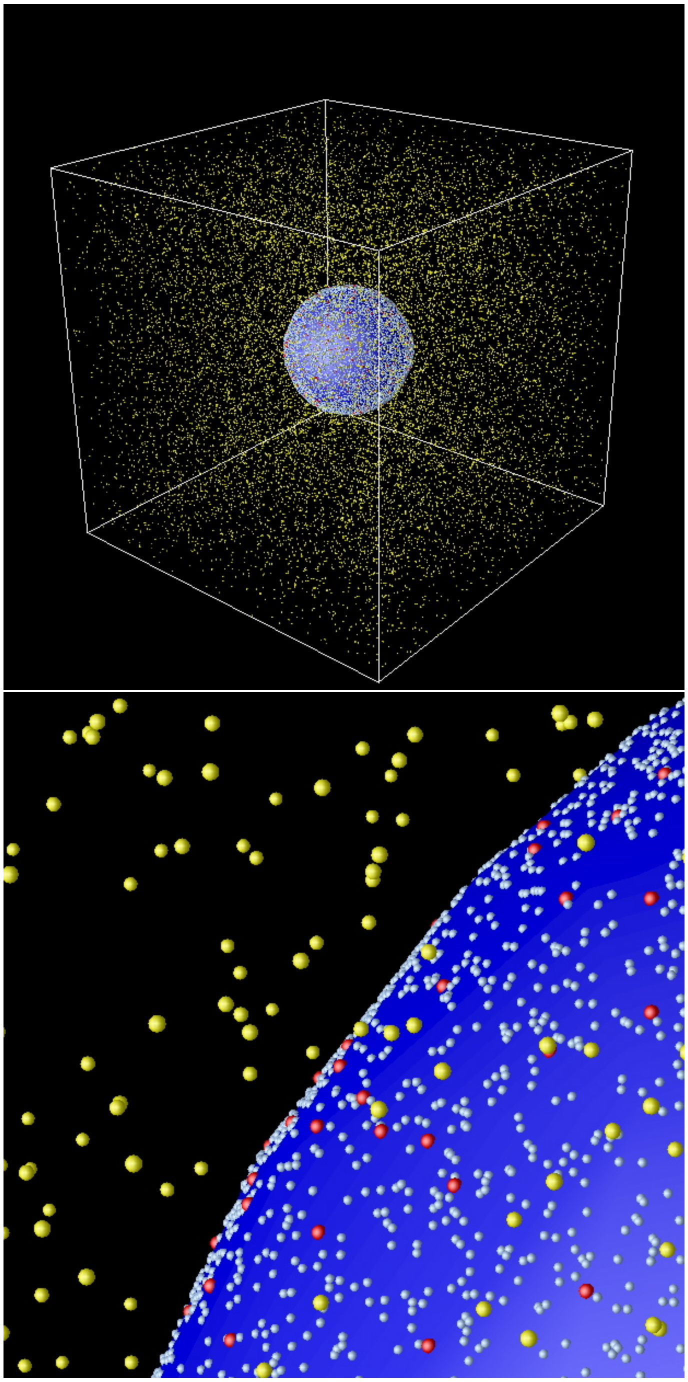

Figure V.1: Representation of the numerical geometry. **Top,** A spherical cell is placed at the center of the computational box. Bound receptors on the cell membrane are plotted red, unbound are plotted as white symbols and freely diffusing ligands are yellow. **Bottom,** A close-up view of the membrane with its receptors and diffusing ligands.

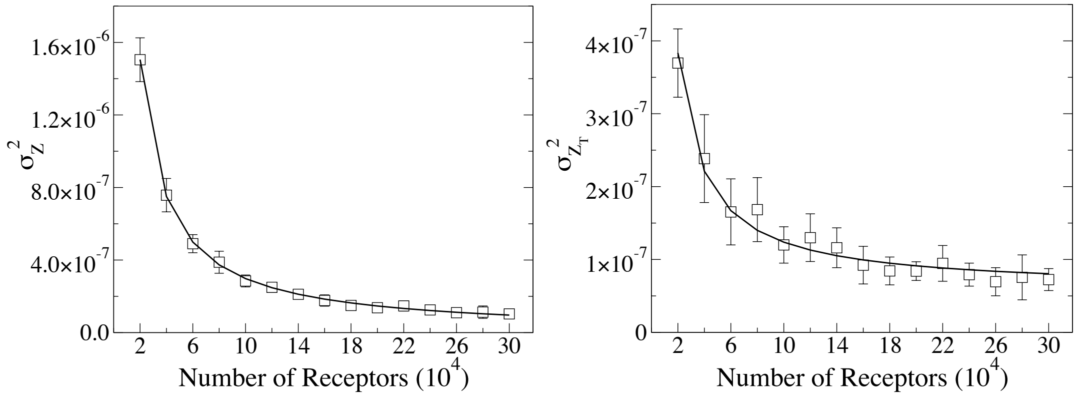

Figure V.2: Instantaneous measurements of receptor occupancy can achieve arbitrary accuracy while time-averaged measurements display a residual noise level. **a,** The variance of instantaneous measurements of receptor occupancy as a function of the number of receptors N. The symbols show the results from our MCell3 simulations which agree very well with the expression $\sigma_Z^2 = \bar{c}K_d/N(\bar{c}+K_d)^2$, shown as a solid line, where $\bar{c}$ is the ligand concentration (1 nM) and K_d is the dissociation constant (30 nM). Remaining parameter values are: $R = 5\mu$m and $k_- = 10\,\mathrm{s}^{-1}$. The fact that the variance vanishes in the limit of large number of receptors can be further verified by fitting the symbols to $A_0/N + B_0$. This fit results in a value of B_0 very close to zero ($B_0 = -4.1 \times 10^{-9}$), indicating that the cell can achieve arbitrary accuracy in its measurement of an external signal. Furthermore, the fitted value of $A_0 = 3.02 \times 10^{-2}$ agrees well with the theoretically predicted value of Eq. 4 (3.12×10^{-2}). The error bars here, and in the remaining figures, indicate the standard deviation obtained by performing 10 independent simulations. **b,** The variance of time-averaged measurements as a function of the number of receptors. Shown are the results of the simulations (symbols) and the fitting formula $A_T/N + B_T$ with $A_T = 6.49 \times 10^{-3}$, in good agreement with Eq. 10, and $B_T = 5.83 \times 10^{-8}$. The instantaneous receptor occupancy was averaged over $T = 1s$.

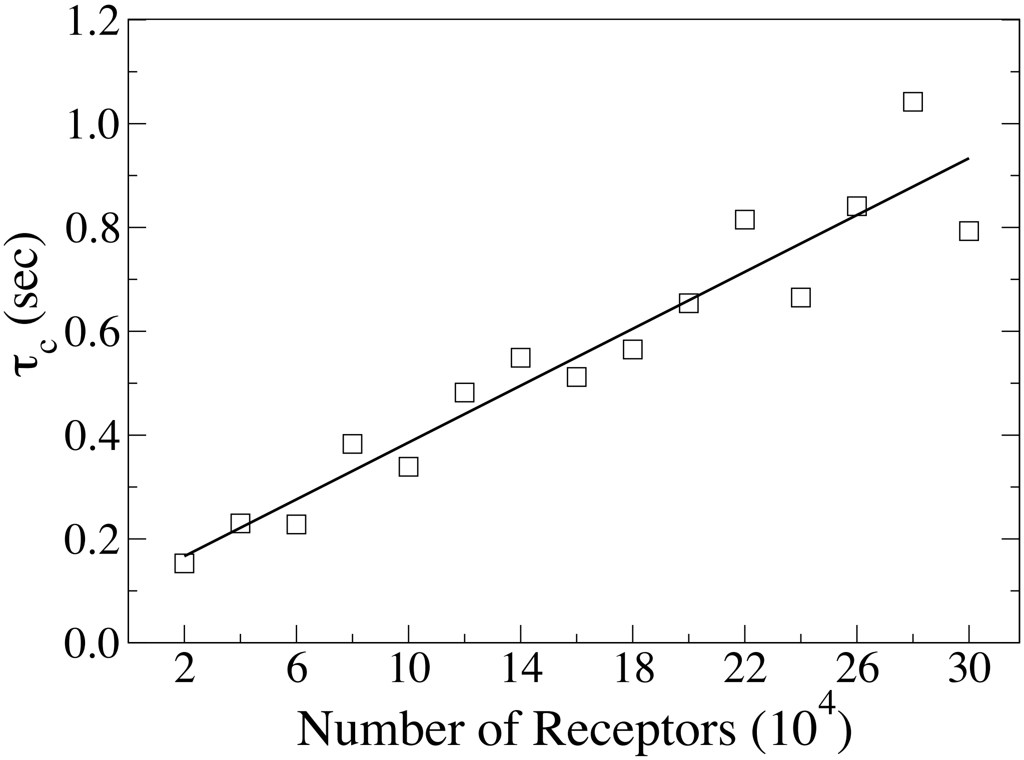

Figure V.3: The correlation time of receptor occupancy increases linearly with the number of receptors. Symbols represent the correlation time obtained from fitting the measured correlation function to an exponential decay function. The solid line shows the linear fit $\tau_c(N) = \tau_0 + \Lambda N$ with $\tau_0 = 0.112s$ and $\Lambda = 2.74 \times 10^{-6}s$.

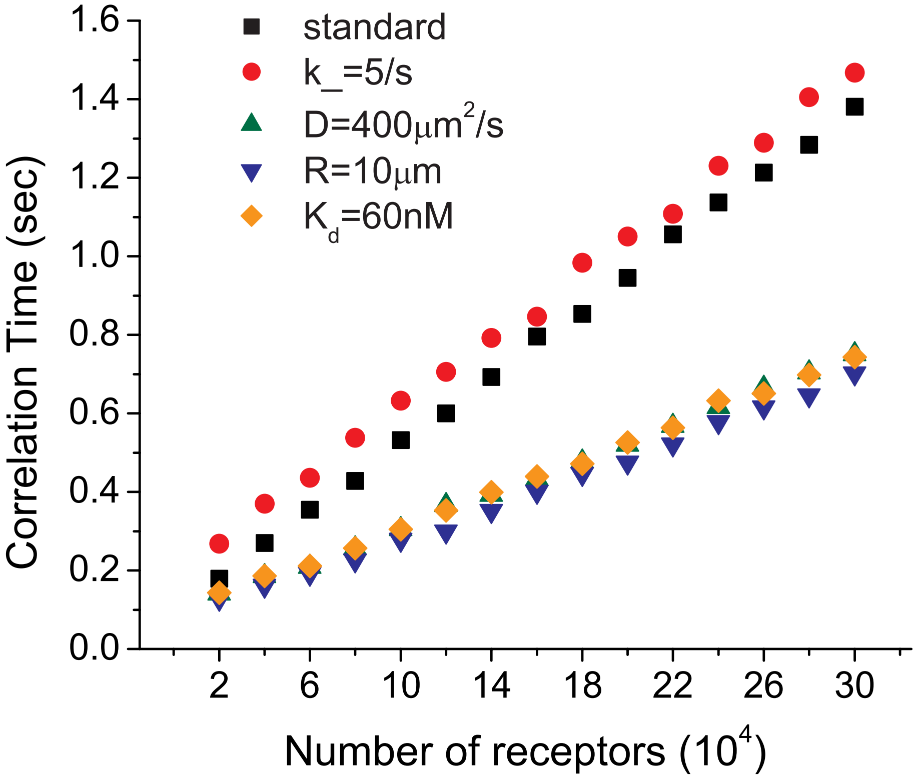

Figure V.4: The correlation time as a function of the number of receptors for different parameter sets. The black symbols correspond to the default parameter set: $R = 5\mu m$, $D = 200\mu m^2/s$, $K_d = 30nM$, $\bar{c} = 1nM$, $k_- = 10s^{-1}$. Other curves are obtained by changing only the indicated parameter. Increasing the value of D, R or K_d reduces the slope of the linear fit by a factor of two, in accordance with Eq. 1. Furthermore, decreasing k_- results in a constant translation of the correlation time, again in agreement with Eq. 1.

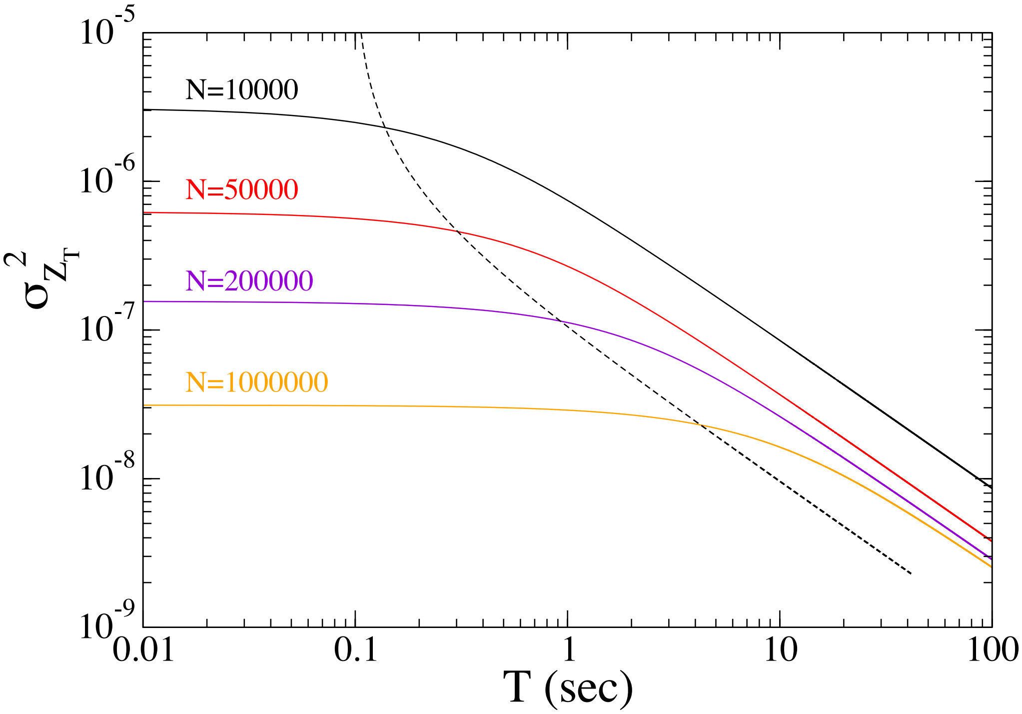

Figure V.5: The time-averaged variance as a function of the measurement time T for different number of receptors. The symbols represent the points for which the measurement time equals the correlation time. The collection of these points for different N is drawn as a dashed line. Below this line, the variance approaches the instantaneous variance σ_Z^2 while above this line the variance scales as $1/T$.

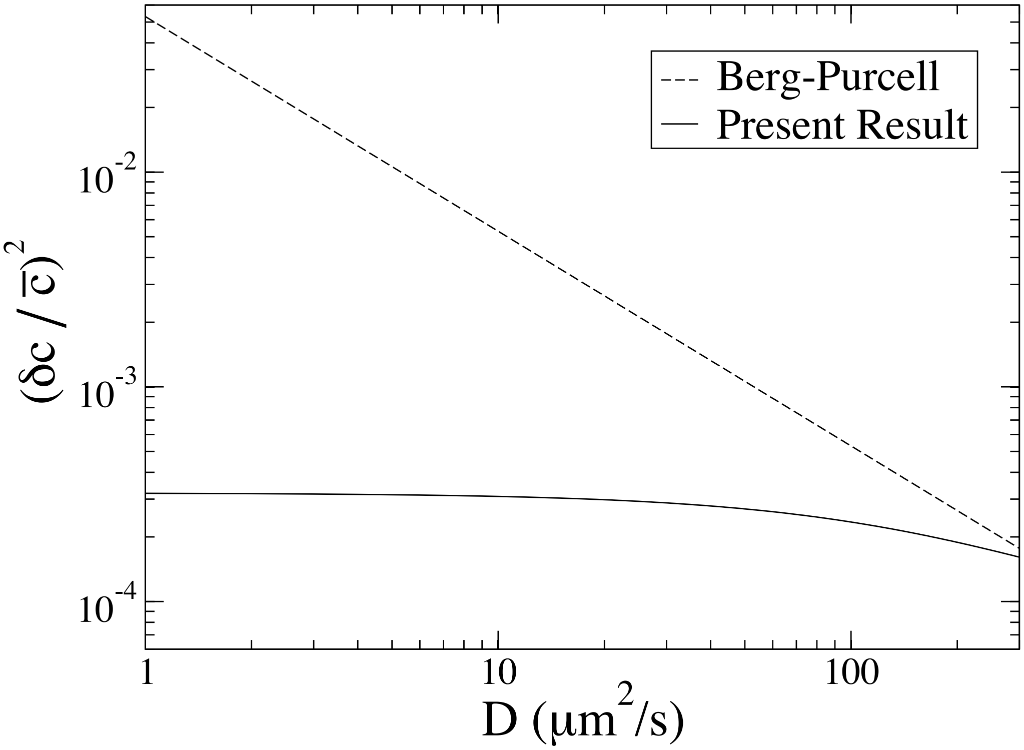

Figure V.6: The Berg and Purcell formula can overestimate the noise level. The dashed line shows the normalized variance in the concentration as a function of the diffusion constant using the Berg and Purcell result. The solid line represents the results found in the present work and demonstrate that for small diffusion constants the widely used formula of Berg and Purcell can significantly overestimate the noise level. Parameter values are the default ones with $N = 100000$ and $T = 1$ s.

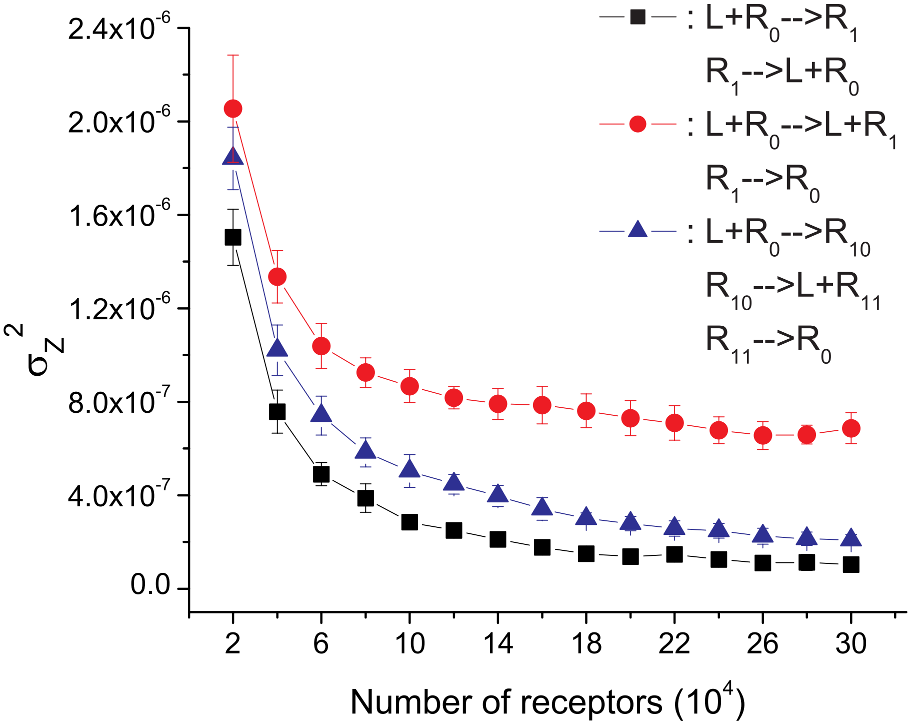

Figure V.7: The variance of the instantaneous receptor occupancy for 3 types of receptor-ligand interactions. Black symbols: binding-unbinding scheme with the default rates ($K_d = 30\,nM$, $k_+ = 0.33nM^{-1}s^{-1}, k_- = 10s^{-1}$). Red symbols: enzymatic scheme for the same rates. Blue symbols: interpolating scheme with $k_+ = 0.33nM^{-1}s^{-1}, k_1 = 20s^{-1}, k_2 = 20s^{-1}$.

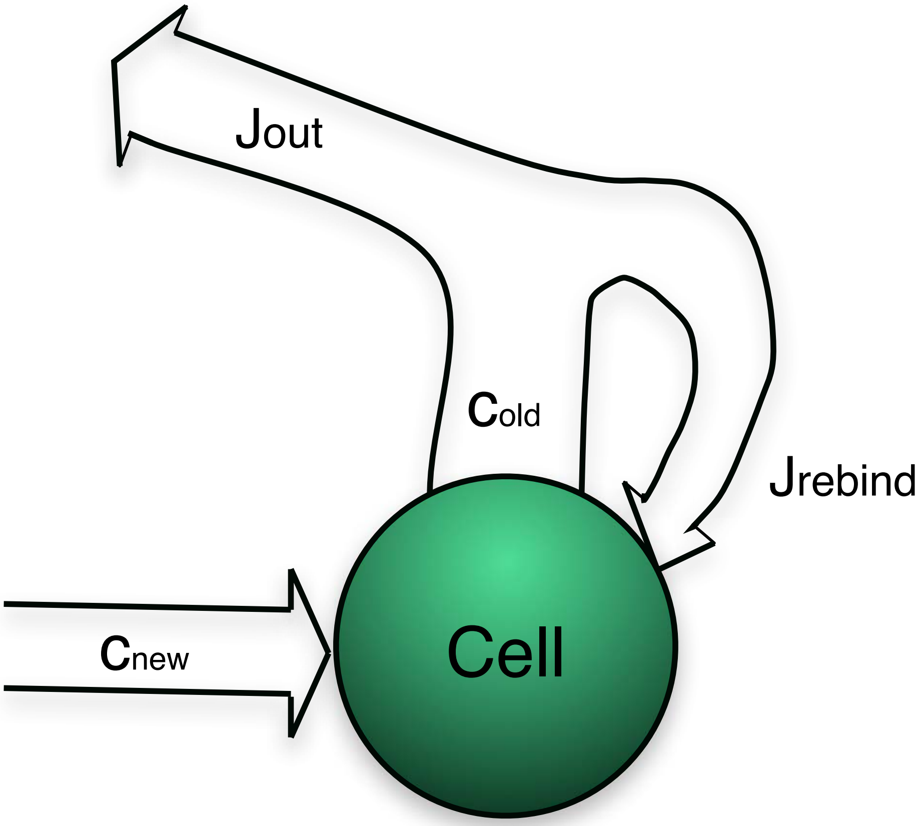

Figure V.8: Ligands are identified as new molecules (those never bind any receptors) and old molecules. New molecules can bind to the receptors and are converted to old molecules. Old molecules can be released from receptors. They can either escape to infinity or rebind to receptors.

V.F Appendix: Calculation of τ_c

As Figure V.8 shows, we divide the flux of molecules into those of ”new” molecules and those of ”old” molecules. We can write down proper differential equations for both type of molecules. For new molecules the concentration at infinity is fixed as $\bar{c}$:

$$\begin{aligned}\frac{\partial c_{new}(r,t)}{\partial t} &= D\nabla^2 c_{new} - a c_{new}\delta(R)\\ c_{new}(\infty) &= \bar{c}\end{aligned} \tag{V.19}$$

where R is the cell radius. For old molecules:

$$\begin{aligned}\frac{\partial c_{old}(r,t)}{\partial t} &= D\nabla^2 c_{old} + (b - a c_{old})\delta(R)\\ c_{old}(\infty) &= 0\end{aligned} \tag{V.20}$$

Note that (V.19)+(V.20) gives the desired dynamics of molecules:

$$\begin{aligned}\frac{\partial c(r,t)}{\partial t} &= D\nabla^2 c + (b - ac)\delta(R)\\ c(\infty) &= \bar{c}\end{aligned} \tag{V.21}$$

Here $c = c_{new} + c_{old}$. If we let $b = a\bar{c}$, then the steady state solution is $c(r) = \bar{c}$. To calculate the refreshing rate of the receptors, we need to know J_{out} in Figure V.8, which is equal to the flux of new molecules at equilibrium. The steady state solution of Eqn. V.19 is:

$$\begin{aligned}c(r) &= c_{in}, \qquad r < R\\ c(r) &= \bar{c} - \frac{A}{r}, \qquad r > R\end{aligned} \tag{V.22}$$

where R is the cell radius. c_{in} and A are unknown constants. At $r = R$, c should be continuous:

$$c_{in} = \bar{c} - \frac{A}{R} \tag{V.23}$$

Also, the flux should be conserved:

$$D\frac{\partial c_{out}}{\partial r}(R) - D\frac{\partial c_{in}}{\partial r}(R) = ac(R) \tag{V.24}$$

Combine (V.23) and (V.24) we get $A = \frac{aR^2\bar{c}}{D+aR}$, and thus the solution:

$$
\begin{aligned}
c(r) &= \frac{D\bar{c}}{D+aR}, && r < R \\
c(r) &= \bar{c}\left(1 - \frac{aR^2}{r(D+aR)}\right), && r > R
\end{aligned}
\tag{V.25}
$$

The flux of the new molecules to the receptors is:

$$
J_{new} = D\frac{\partial c_{out}}{\partial r}(R) = \frac{Da\bar{c}}{D+aR} = \frac{\bar{c}D}{R} \cdot \frac{aR}{D+aR} \tag{V.26}
$$

Now let's consider there are n_c molecules binded to receptors, and there is no new molecules. The dynamics of n_c satisfies:

$$
\frac{dn_c}{dt} = -4\pi R^2 J_{out} \tag{V.27}
$$

and J_{out} has the same form as J_{new}:

$$
J_{out} = \frac{c(R)D}{R} \cdot \frac{aR}{D+aR} \tag{V.28}
$$

on the membrane $n_c = Nc/K_d$, where N is the total number of receptors, and c is small. Plug J_{out} into (V.26), we get:

$$
\frac{dn_c}{dt} = -n_c/\tau_c \tag{V.29}
$$

and the correlation time is:

$$
\tau_c = \frac{N}{4\pi DRK_d}\left(1 + \frac{D}{aR}\right) \tag{V.30}
$$

Now we need to figure out a. Obviously a should be proportional to the receptor density and the binding rate constant:

$$
a \propto \rho_N k_+ = \frac{Nk_-}{4\pi R^2 K_d} \tag{V.31}
$$

Actually this gives the right dimension. So we assume $a = \frac{Nk_-}{4\pi R^2 K_d}$ and finally we get the correlation time as:

$$
\tau_c = \frac{1}{k_-} + \frac{N}{4\pi DRK_d} \tag{V.32}
$$

V.G Appendix: Calculation of σ_Z^2 for the Alternative Scheme

The reaction scheme considered here is:

$\mathrm{L{+}R_0} \longrightarrow \mathrm{L{+}R_1}$

$\mathrm{R_1} \longrightarrow \mathrm{R_0}$

To be convenient, I also list all the notations used in the following calculations here:

$c(\vec{x}, t)$: Concentration of molecule C at space $\vec{x}$ and time t.

$y_i(t)$: The state of i^{th} receptor at time t. It is either 0(unbound) or 1(bound).

N: Total number of receptors on the cell membrane.

k_+: Binding rate constant.

k_-: Unbinding rate constant.

K_d: k_-/k_+, Dissociation constant.

$\bar{c}$: Equilibrium mean concentration of molecule C around the cell.

Γ: $k_+\bar{c} + k_-$.

$\tilde{c}$: $\bar{c}/K_d$, relative molecule concentration.

$G(\vec{x}, t)$: Green function of the diffusion equation in a free space.

$P_{ij}(y_i(t_1), y_j(t_2))$: Joint probability of the i^{th} and j^{th} receptor states at t_1 and t_2 respectively.

$P_{ij}(y_i(t_1), y_j(t_2)|\vec{c}_i(t_1), \vec{c}_j(t_2))$: Joint probability of receptor states given the trajectories of the molecule concentrations around the two receptors up to time t_1 and t_2 respectively.

$\mathcal{P}(\vec{c}_i(t_1), \vec{c}_j(t_2))$: Joint probability of the trajectories of the molecule concentrations at $\vec{x}_i$ and $\vec{x}_j$ up to time t_1 and t_2 respectively.

$\hat{f}(s)$: Laplace transform of $f(t)$.

$\langle f \rangle$: The ensemble average of f.

V.G.1 $\langle \delta y_i(t) \delta y_j(t) \rangle$

$$\begin{aligned} \langle y_i(t) y_j(t) \rangle &= \sum_{y_i(t) y_j(t)} y_i(t) y_j(t) P_{ij}(y_i(t), y_j(t)) \\ &= P_{ij}(1,1) \\ &= \int \mathcal{D}\vec{c}_i \mathcal{D}\vec{c}_j P_{ij}(1,1|\vec{c}_i(t), \vec{c}_j(t)) \mathcal{P}(\vec{c}_i(t), \vec{c}_j(t)) \\ &= \int \mathcal{D}\vec{c}_i \mathcal{D}\vec{c}_j P_i(1|\vec{c}_i) P_j(1|\vec{c}_j) \mathcal{P}(\vec{c}_i(t), \vec{c}_j(t)) \end{aligned} \tag{V.33}$$

Now let's suppose $c_i(t) = \bar{c} + \delta c_i(t)$ and expand $P_i(1|\vec{c}_i)$ around the mean of c at every time:

$$P_i(1|\vec{c}_i) = P_i(1|\bar{c}) + \int_{-\infty}^{t} d\tau_k \left[\frac{\delta P_i(1|\vec{c}_i)}{\delta c_i(\tau_k)} \right]_{c_i(\tau_k)=\bar{c}} \delta c_i(\tau_k) \tag{V.34}$$

Note that $< y_i(t) >= P_i(1|\bar{c})$ at equilibrium. Plug Eqn. V.34 into Eqn. V.33, we get:

$$\langle y_i(t) y_j(t) \rangle = \langle y_i(t) \rangle \langle y_j(t) \rangle + \int \mathcal{D}\vec{\delta c}_i \mathcal{D}\vec{\delta c}_j \mathcal{P}(\vec{\delta c}_i(t), \vec{\delta c}_j(t)) \cdot \\ \left(\int_{-\infty}^{t} d\tau_k \left[\frac{\delta P_i(1|\vec{c}_i)}{\delta c_i(\tau_k)} \right]_{c_i(\tau_k)=\bar{c}} \delta c_i(\tau_k) \right) \left(\int_{-\infty}^{t} d\tau_l \left[\frac{\delta P_j(1|\vec{c}_j)}{\delta c_j(\tau_l)} \right]_{c_j(\tau_l)=\bar{c}} \delta c_j(\tau_l) \right) \tag{V.35}$$

Let $\delta y_i(t) = y_i(t) - \langle y_i(t) \rangle$, and note that

$$\langle \delta c_i(\tau_k) \delta c_j(\tau_l) \rangle = \int \mathcal{D}\vec{\delta c}_i \mathcal{D}\vec{\delta c}_j \mathcal{P}(\vec{\delta c}_i(t), \vec{\delta c}_j(t)) \delta c_i(\tau_k) \delta c_j(\tau_l) \tag{V.36}$$

Plug these into Eqn. V.35, we get:

$$\langle \delta y_i(t) \delta y_j(t) \rangle = \int_{-\infty}^{t} d\tau_k \int_{-\infty}^{t} d\tau_l \langle \delta c_i(\tau_k) \delta c_j(\tau_l) \rangle Q(\tau_k) Q(\tau_l) \tag{V.37}$$

where

$$Q(t) = \left[\frac{\delta P(1|\vec{c})}{\delta c(t)} \right]_{c(t)=\bar{c}} \tag{V.38}$$

Eqn. V.37 establishes a simple relation between $\langle \delta y_i(t) \delta y_j(t) \rangle$ and $\langle \delta c_i(\tau_k) \delta c_j(\tau_l) \rangle$. We can expect to get another relation between these two correlation functions from the diffusion equation and thus solve out these two functions. For this section, we assume the cell membrane is transparent and the catalytic reaction scheme is adopted, so that the binding process won't affect $\delta c_i(t)$. The diffusion equation reads:

$$\frac{d\delta c}{dt} = D\nabla^2 \delta c + \nabla \cdot \vec{L}(\vec{x}, t) \tag{V.39}$$

and the random flux $\vec{L}$ satisfies,

$$\langle L_i(\vec{x}, t) L_j(\vec{x}', t') \rangle = 2D\bar{c}\delta_{ij}\delta(\vec{x} - \vec{x}')\delta(t - t') \tag{V.40}$$

It can be proved that,

$$\langle \delta c_i(\tau_k) \delta c_j(\tau_l) \rangle = \bar{c} G(\vec{x}_i - \vec{x}_j, \tau_k - \tau_l) \tag{V.41}$$

Next step we need to calculate $Q(t)$. Note that $P_i(1|\vec{c}_i(t))$ satisfies the following master equation:

$$\frac{dP_i(1|\vec{c}_i(t))}{dt} = k_+ c_i(t)(1 - P_i(1|\vec{c}_i(t))) - k_- P_i(1|\vec{c}_i(t)) \tag{V.42}$$

The solution is:

$$P_i(1|\vec{c}_i(t)) = \int_{-\infty}^{t} dt' k_+ c_i(t') \exp\left(-\int_{t'}^{t} dt''(k_- + k_+ c_i(t''))\right) \tag{V.43}$$

So for some $\tau < t$, we get:

$$Q(\tau) = \frac{k_- k_+}{\Gamma} e^{-\Gamma(t-\tau)} \tag{V.44}$$

Plug Eqn. V.41 and Eqn. V.44 back into Eqn. V.37, we get:

$$\begin{aligned} \langle \delta y_i(t) \delta y_j(t) \rangle &= \frac{\bar{c} k_-^2 k_+^2 e^{-2\Gamma t}}{\Gamma^2 (4\pi D)^{3/2}} \int_{-\infty}^{t} \int_{-\infty}^{t} d\tau_k d\tau_l \, |\tau_k - \tau_l|^{-\frac{3}{2}} \, e^{-\frac{|\vec{x}_i - \vec{x}_j|^2}{4D|\tau_k - \tau_l|} + \Gamma(\tau_k + \tau_l)} \\ &= \frac{\bar{c} k_-^2 k_+^2 e^{-2\Gamma t}}{\Gamma^2 (2\pi)^3} \int d\vec{k} \int_{-\infty}^{t} \int_{-\infty}^{t} d\tau_k d\tau_l e^{-i\vec{k} \cdot (\vec{x}_i - \vec{x}_j) - Dk^2 |\tau_k - \tau_l| + \Gamma(\tau_k + \tau_l)} \end{aligned} \tag{V.45}$$

Now the integral over τ_k and τ_l are simple exponentials. After computing them, the equation becomes:

$$\begin{aligned}
\langle \delta y_i(t)\delta y_j(t)\rangle &= \frac{\bar{c}k_-^2k_+^2}{\Gamma^3(2\pi)^3}\int d\vec{k}\frac{e^{-i\vec{k}\cdot(\vec{x}_i-\vec{x}_j)}}{\Gamma+Dk^2} \\
&= \frac{\bar{c}k_-^2k_+^2}{\Gamma^3(2\pi)^3}\int_0^\infty k^2dk\int_0^\pi d\theta sin\theta\int_0^{2\pi}d\varphi\frac{e^{-ik|\vec{x}_i-\vec{x}_j|cos\theta}}{\Gamma+Dk^2} \\
&= -i\frac{\bar{c}k_-^2k_+^2}{\Gamma^3(2\pi)^2|\vec{x}_i-\vec{x}_j|}\int_{-\infty}^{+\infty}dk\frac{ke^{ik|\vec{x}_i-\vec{x}_j|}}{\Gamma+Dk^2} \qquad \text{(V.46)}
\end{aligned}$$

Finally we get:

$$\langle \delta y_i(t)\delta y_j(t)\rangle = \frac{\bar{c}k_-^2k_+^2}{4\pi\Gamma^3|\vec{x}_i-\vec{x}_j|}e^{-\sqrt{\frac{\Gamma}{D}}|\vec{x}_i-\vec{x}_j|} \qquad \text{(V.47)}$$

V.G.2 σ_Z^2

Suppose $Z = \frac{1}{N}\sum_{i=1}^N y_i$ is the final output of the receptor bindings that the cell can measure. It is interesting to ask how the fluctuation of Z depends on the system parameters. From its definition, we have:

$$\langle Z^2\rangle = \frac{1}{N^2}\sum_{i=1}^N\langle y_i^2\rangle + \frac{1}{N^2}\sum_{i=1}^N\sum_{j\neq i}\langle y_iy_j\rangle \qquad \text{(V.48)}$$

Let $p = \langle y_i\rangle$, it is obvious that $\langle y_i^2\rangle = p$ too. So,

$$\begin{aligned}
\langle Z^2\rangle &= \frac{Np}{N^2}+\frac{N(N-1)p^2}{N^2}+\frac{1}{N^2}\sum_{i=1}^N\sum_{j\neq i}\langle\delta y_i\delta y_j\rangle \\
&= p^2+\frac{p(1-p)}{N}+\frac{1}{N^2}\sum_{i=1}^N\sum_{j\neq i}\langle\delta y_i\delta y_j\rangle \\
&= \frac{k_-k_+\bar{c}}{N\Gamma}+\langle Z\rangle^2+\frac{1}{N^2}\sum_{i=1}^N\sum_{j\neq i}\langle\delta y_i\delta y_j\rangle \qquad \text{(V.49)}
\end{aligned}$$

So the variance of Z is,

$$\sigma_Z^2 = \frac{k_-k_+\bar{c}}{N\Gamma}+\frac{1}{N^2}\sum_{i=1}^N\sum_{j\neq i}\langle\delta y_i\delta y_j\rangle \qquad \text{(V.50)}$$

Now let's assume that the cell is an ideal sphere with transparent membrane, and the receptors are evenly distributed on the membrane. Due to the symmetry, the outer sum can be replaced by a factor of N. In the limit that N is large, the inner sum can be approximated by the integral:

$$\sum_{j=2}^{N}\langle\delta y_1\delta y_j\rangle = \frac{N}{4\pi}\int_0^{\pi} d\theta\sin\theta\int_0^{2\pi} d\varphi\langle\delta y(0,0)\delta y(\theta,\varphi)\rangle \tag{V.51}$$

It is easy to prove that $|\vec{x}(0,0)-\vec{x}(\theta,\varphi)| = 2R\sin\frac{\theta}{2}$, where R is the radius of the cell. Then Eqn. V.47 becomes:

$$\langle\delta y(0,0)\delta y(\theta,\varphi)\rangle = \frac{\bar{c}k_-^2k_+^2}{8\pi D\Gamma^3 R\sin\frac{\theta}{2}}e^{-\sqrt{\frac{\Gamma}{D}}R\sin\frac{\theta}{2}} \tag{V.52}$$

Plug this back into Eqn. V.51, we can get:

$$\sum_{j=2}^{N}\langle\delta y_1\delta y_j\rangle = \frac{\bar{c}k_-^2k_+^2}{8\pi D^{1/2}\Gamma^{7/2}R^2}\left(1-e^{-2R\sqrt{\frac{\Gamma}{D}}}\right) \tag{V.53}$$

Put this into Eqn. V.50, and change parameter sets to $\{D,\tilde{c},k_-,K_d,R\}$, we get the final answer as the following:

$$\langle\sigma_Z^2\rangle = \frac{\tilde{c}}{(1+\tilde{c})^2}(\frac{1}{N}+\frac{1}{N_c}) \tag{V.54}$$

where

$$N_c = 8\pi R^2 K_d(1+\tilde{c})^{3/2}\sqrt{\frac{D}{k_-}}\cdot\frac{1}{1-e^{-2R\sqrt{\frac{k_-(1+\tilde{c})}{D}}}} \tag{V.55}$$

Despite the transparent cell assumption and the first order approximation in Eqn. V.34, this result is precise for the catalytic reaction scheme. Actually, it fits quite well with MCell simulations.

Bibliography

[1] Bray, D. (1999) Protein molecules as computational elements in living cells. *Nature* **376,** 307-312.

[2] Berg, H. C. & Purcell, E. M. (1977) Physics of chemoreception. *Biophys. J.* **20,** 193-219.

[3] Bialek, W. & Setayeshgar, S. (2005) Physical limits to biochemical signaling. *Proc. Natl. Acad. Sci.* **102,** 10040-10045.

[4] Stiles, D. & Bartol, T. M. (2001) Monte Carlo methods for simulating realistic synaptic microphysiology using MCell. In de Schutter, E. (ed.) *Computational Neurobiology: Realistic Modeling for Experimentalists*, 87-127 CRC Press, Boca Raton, FL.

[5] Bourne, H. R. & Weiner, O. (1999) A chemical compass. *Nature* **419,** 21.

[6] Song, L. Nadkarni, S. M., Bodeker, H. U., Beta, C., Bae, A., Franck, C., Rappel, W. J., Loomis, W. F. & Bodenschatz, E. (2006) *Dictyostelium discoideum* chemotaxis: threshold for directed motion. *Eur. J. Cell Biol.* **85,** 981-989.

[7] Adams, J. A., Omann, G. M. & Linderman, J. J. (1998) A mathematical model for ligand/receptor/G-protein dynamics and actin polymerization in human neutrophils. *J. Theor. Biol.* **193,** 543-560.

[8] Chang, P. S., Axelrod, D., Omann, G. M. & Linderman, J. J. (2005) G protein threshold behavior in the human neutrophil oxidant response: measurement of G proteins available for signaling in responding and nonresponding subpopulations. *Cell Signal* **17,** 605-614.

[9] Weisbart, R. H., Golde, D. W. & Gasson, J. C. (1986) Biosynthetic human GM-CSF modulates the number and affinity of neutrophil f-Met-Leu-Phe receptors. *J. Immunol.* **137,** 3584-3587.

[10] Tennenberg, S. D., Zemlan, F. P. & Solomkin, J. S. (1988) Characterization of N-formyl-methionyl-leucyl-phenylalanine receptors on human neutrophils: effects of isolation and temperature on receptor expression and functional activity. *J. Immunol* **141,** 3937-3944.

[11] Beebe, D. J., Mensing, G. A. & Walker, G. M. (2002) Physics and applications of microfluidics in biology. *Annu. Rev. Biomed. Eng.* **4,** 261-286.

[12] Jeon, N. L., Baskaran, H., Dertinger, S. K., Whitesides, G. M., Van de Water, L. & Toner, M. (2002) Neutrophil chemotaxis in linear and complex gradients of interleukin-8 formed in a microfabricated device. *Nat. Biotechnol.* **20,** 826-830.

VI

Conclusions

In this thesis we have investigated three topics about stochastic effects in biological systems: the formation of spontaneous calcium wave in *Xenopus* oocytes, the stochastic cooperative gating of cardiac RyR and its relation with heart failure disease, and the noise of chemoreception.

The opening of inositol (1,4,5)-triphosphate (IP_3) receptors, clustered at discrete sites on the endoplasmic reticulum, can lead to large scale intracellular calcium waves. Experiments in *Xenopus* oocytes have shown that the inter-wave intervals for these spontaneous waves have a standard deviation that is much smaller than their mean and that the background calcium concentration exhibits a slow rise during the inter-wave interval. In Chapter III, we built a simple mathematical model and examined the possibility that this slow rise increases the cooperativity between the openings of the clusters. We find that incorporating pumps that slowly activate leads to a slow increase in the background calcium concentration which makes global events progressively more likely to occur. We show that this cooperativity results in much smaller standard deviations and inter-wave interval distributions that are close to experimental observations.

In Chapter IV we studied the cooperative gating of RyR in cardiac myocytes. Recent experiments have suggested that cooperativity between the four monomers comprising the RyR plays an important role in the dynamics of the overall receptor. Furthermore, this cooperativity can be affected by the binding of FKBP and hence modulated by adrenergic stimulation through the phosphorylating action of PKA. This has important implications for heart failure, where it has been hypothesized that RyR hyperphosphorylation, resulting in a loss of cooperativity, can lead to a persistent leak and a reduced SR content. In this study, we construct a theoretical model that examines the cooperativity via the assumption of an allosteric interaction between the four subunits. We find that the level of cooperativity, regulated by FKBP binding, can have a dramatic effect on the excitation-contraction (E-C) coupling gain and that this gain exhibits a clear maximum. These findings are compared to currently available data from different species and allows for an evaluation of the heart failure scenario.

In Chapter V we studied a general problem about how accurate a cell can detect environmental chemical signals via the bindings of membrane receptors. At the level of a single receptor, this process is inherently stochastic, but cells can contain many such receptors which can reduce the variability in the detected signal by suitable averaging. We applied explicit Monte Carlo simulations and analytical calculations to characterize the noise level as a function of the number of receptors. We show that the noise of an instantaneous measurement approaches zero for large receptor number, while the noise of a time-averaged measurement has a residue noise due to the rebindings of signal molecules by membrane receptors. Furthermore, the correlation time of receptor-ligand interaction increases linearly with receptor number. For a cell with fixed measuring time characterized by internal signaling pathways, increasing receptor number converts a time-averaged measurement into an instantaneous measurement, and thus the cell achieves arbitrary accuracy. This result has important implications for such processes as eukaryotic chemotaxis.